1-28-2015

A 3D Computational Fluid Dynamics Model Validation for Candidate Molybdenum-99 Target Geometry

Lin Zheng

Follow this and additional works at: https://digitalrepository.unm.edu/me_etds

Lin Zheng
_____
Candidate

Mechanical Engineering
_____
Department

This thesis is approved, and it is acceptable in quality and form for publication:

Approved by the Thesis Committee:

Peter Vorobieff, Chairperson
_____

Svetlana Poroseva
_____

Eric Olivas
_____

_____

_____

_____

_____

_____

A 3D Computational Fluid Dynamics Model Validation for

Candidate Molybdenum-99 Target Geometry

By

LIN ZHENG

B.S MECHANICAL ENGINEERING, UNIVERSITY OF NEW MEXICO (2012)

THESIS

Submitted in Partial Fulfillment of the
Requirements for the Degree of

Master of Science
Mechanical Engineering

The University of New Mexico
Albuquerque, New Mexico

December 2014

Acknowledgements

First, I would like to thank Dr. Greg Dale, of Los Alamos National Laboratory, for providing this project. He provided me the history and background of this project. He helped me understand how significant this project will benefit our society. Several other individuals that I'd also like to thank for and they are:

Dr. Peter Vorobieff, my advisor and professor at the University of New Mexico, for providing guidance and direction when it was needed at any time. He encouraged me to record all my research progress by constructing a series of bi-weekly progress reports. It had really helped me on the development of this thesis.

Keith Woloshun, Frank Romero, and Eric Olivas, of Los Alamos National Laboratory, for their supports and helps on both model and experiment developments for this project.

Nima Fathi, PhD Candidate at the University of New Mexico, for explaining me the process of doing computational fluid dynamics modeling. He provided me ideas of how to do verification and validation for my CFD model.

Donald Mercer and Sloan Pearsall, my office mates at the University of New Mexico, for proving me help in different academic areas. I have to thank them for spent those long hours in the office with me to develop this thesis.

A 3D COMPUTATIONAL FLUID DYNAMICS MODEL VALIDATION FOR CANDIDATE
MOLYBDENUM-99 TARGET GEOMETRY

By
Lin Zheng

B.S. Mechanical Engineering, University of New Mexico, 2012

M.S. Mechanical Engineering, University of New Mexico, 2014

Abstract

As part of its nuclear nonproliferation mission, the U.S. Department of Energy's Global Threat Reduction Initiative (GTRI) is working to develop a sustainable means for producing the critical medical isotope molybdenum-99 (^{99}Mo) without using highly enriched uranium (HEU). ^{99}Mo is the parent product of technetium-99m (^{99m}Tc), a radioisotope used in approximately 50,000 medical diagnostic tests per day in the U.S. The primary uses of this product include detection of heart disease, cancer, study of organ structure and function, and other applications. ^{99}Mo has a short half-life (66 hours) and cannot be stockpiled. U.S. demand is approximately 50% of the world market. The objective of the domestic ^{99}Mo project is to accelerate existing commercial projects to meet at least 100% of the U.S. demand of ^{99}Mo produced without HEU by the end of 2016.

New methods for generating ^{99}Mo are being explored in an effort to eliminate proliferation issues and provide a domestic supply of ^{99m}Tc for medical imaging within

the United States. For this project, electron accelerating technology is used by sending an electron beam through a series of ^{100}Mo targets. During this process a large amount of heat is created, which directly affects the operating temperature set for the system. The wall temperature along the target section must be maintained between 550 ℃ and 650 ℃. This temperature range is dictated by the tensile stress limit of the wall material.

To maintain the required temperature range, helium gas is used to server as a cooling agent that flows through narrow channels between the target disks.

This thesis investigated the cooling performance on a series of new geometry designs of the cooling channel by using Computational Fluid Dynamics (CFD) software ANSYS FLUENT 14.5. An experiment was also conducted to conclude whether the CFD model is valid and able to predict the right physics of the cooling channels. As a result, a new optimal geometry for the cooling channels will be selected for the purpose of the ^{99}Mo project.

Table of Contents

List of Figures

List of Tables

List of Variables

$\dot{Q}$ = Power

$\dot{m}$ = Mass flow rate

$\bar{T}_2$ = Average outlet temperature

$\bar{T}_1$ = Average inlet temperature

M = Mach number

v, V = Velocity

v_{sound} = Speed of sound

ρ = Density

E = Bulk modulus of elasticity

k = Thermal conductivity

R = Gas constant

T = Absolute temperature

p = Pressure

Q = Volumetric flow rate

A = Area

Re = Reynolds number

ℓ = Characteristic length

μ = Dynamic viscosity

μ_t = Turbulence viscosity

u_i, u_j = Directional velocity components

$\overline{u_i' u_j'}$ = Average fluctuating velocity component

Chapter 1 - Introduction and Literature Review

Nuclear Medicine is a branch of medicine that uses radiation to provide information about the functioning of a person's specific organs or to treat disease. Over 10,000 hospitals worldwide use radioisotopes in medicine and about 90% of the procedures are for diagnostics. The most common radioisotope used in diagnosis is technetium-99m (^{99m}Tc), with some 40 million procedures per year (16.7 million in USA in 2012), accounting for 80% of all nuclear medicine procedures worldwide. [1]

One of reasons that ^{99m}Tc is so popular in the nuclear medicine world is because of its short half-life. It has a half-life of six hours which is long enough to examine metabolic process yet short enough to minimize the radiation dose to the patient. However, the short half-life of ^{99m}Tc radioisotopes has created an issue when transporting them from the facility where they are created to their end users. To resolve this issue, ^{99m}Tc must be transported in the form of molybdenum-99 (^{99}Mo), which is the parent isotope of ^{99m}Tc. ^{99}Mo has a longer half-life of 66 hours and cannot be stockpiled.

Over 99% of the ^{99}Mo is made in five reactors: NRU in Canada (40%), HFR in Netherlands (30%), BR-2 in Belgium (9%), Osiris in France (5%), and Safari-1 in South Africa (10%). [1] Table 1.1 shows more info on the current ^{99}Mo production reactors.

In addition to the information provided above, statistics show that the entire U.S. supply of ^{99}Mo for nuclear medicine has been produced in aging foreign reactors using highly enriched uranium (HEU) targets. Within the last few years, maintenance and

repair shutdowns of these reactors have significantly disrupted the supply of ^{99}Mo in the U.S. and much of the rest of the world. [2]

Table 1.1: Main Mo-99 Production Reactors

	Reactor	Targets	Capacity*	Start	Est Stop
Belgium	BR-2	HEU	289	1961	2026
Netherlands	HFR	HEU	173	1961	2022
Czech Rep	LVR-5	HEU	104	1989	2028
Poland	Maria	LEU	71	1974	2030
Canada	NRU	HEU	173	1957	2016
Australia	OPAL	LEU	37	2006	2030+
France	OSIRIS	HEU	44	1966	2015+
Argentina	RA-3	LEU	15	1967	2027
Russia	RIAR	HEU	33	1961-70	--
South Africa	Safari-1	LEU	111	1965	2025
Total	--	--	1050	--	--

Because of the issues described above, Los Alamos National Laboratory (LANL) and Argonne National Laboratory (ANL) are working together with NorthStar Medical Technologies, LLC as part of the National Nuclear Security Administration (NSSA) Global Threat Reduction Initiative's (GTRI) program to accelerate the establishment of a reliable domestic supply of ^{99}Mo for nuclear medicine, produced without the use of HEU targets. [2]

Experiments are being performed by LANL and ANL to develop and demonstrate the technology necessary for large scale production of ^{99}Mo using high-power electron accelerators. ^{99}Mo is produced with electron accelerators using the ^{100}Mo(γ, n) ^{99}Mo reaction in an enriched ^{100}Mo target. This reaction has a threshold of 9 MeV and peak cross section of 150 mb. The photons for this reaction are generated by bremsstrahlung as

the electron beam from the accelerator collides with the target. After irradiation, the low specific activity ^{99}Mo is separated from the target using a two column generator developed by NorthStar Medical Technologies, LLC. [2] [3]

The subject currently under investigation in this work is mainly focused on the target cooling. The relationship between the behavior of the cooling fluid and the channel geometries are studied. The result of this thesis will provide a series of data (velocity, mass flow rate, and pressure drop, etc.) and comparisons to come up with a new design to optimize the heat transfer ability of the system.

1.1 History of ^{99m}Tc Production and Usage

^{99m}Tc was the first artificially produced element. ^{99m}Tc also occurs naturally in very small amount in the earth's crust. It was discovered by Carol Perrier and Emilio Segre in 1937. ^{99m}Tc was created by bombarding molybdenum atoms with deuterons that had been accelerated by a device called a cyclotron at University of California, Berkeley. [4] ^{99m}Tc was first obtained from molybdenum but is also produced as a nuclear reactor fission product of uranium and plutonium. All isotopes of technetium are radioactive, and the most commonly available forms are Tc-99 and Tc-99m. [5]

^{99m}Tc is an excellent superconductor at very low temperatures. In addition, ^{99m}Tc has anti-corrosive properties. Five parts of technetium per million will protect carbon steels from corrosion at room temperature. [5] However, ^{99m}Tc is primarily used in medical therapy in brain, bone, liver, spleen, kidney, and thyroid scanning and for blood flow studies. ^{99m}Tc is the radioisotope mostly widely used as a tracer for medical diagnosis. [5]

1.1.1 Nuclear Medicine Techniques and Development

As a popular source of nuclear medical imaging, ^{99m}Tc has played an important role in the nuclear medicine development. Nuclear medicine was developed in the 1950s by physicians with an endocrine emphasis, initially using iodine-131 to diagnose and then treat thyroid disease. In recent years, specialists have also come from radiology, as dual Computed X-ray Tomography (CT)/Positron Emission Tomography (PET) procedures have become established. [1]

CT scans and nuclear medicine contribute 36% of the total radiation exposure and 75% of the medical exposure to the US population, according to a US National Council on Radiation Protection & Measurement report in 2009. [1]

New procedures combine CT and PET scans to give co-registration of two images (PETCT), enabling 30% better diagnosis than with traditional gamma camera alone. It is a very powerful and significant tool which provides unique information on a wide variety of diseases from dementia to cardiovascular disease and cancer (oncology). [1]

1.1.2 Early Productions of ^{99}Mo/^{99m}Tc

Brookhaven reactor pioneered research using subatomic particles as tools to investigate the structure of matter. The Brookhaven High Flux Beam Reactor first achieved a self-sustaining chain reaction on October 31, 1965. For over 30 years, this reactor was one of two premier beam reactors in the world, the other being the Institut Laue-Langevin reactor in Grenoble, France. [6]

The raw material, which is produced in a nuclear reactor, is then transferred to a processing facility where it is purified through a multi-step process. The finished raw of ^{99}Mo is sent to generator manufactures to introduce them in medical markets for use of its decay product ^{99m}Tc in medical applications. In 1959 the U.S. Brookhaven National Laboratory (BNL) started to develop a generator to produce ^{99m}Tc from the reactor fissionable product ^{99}Mo, which has much longer half-life. The first ^{99m}Tc radiotracers were developed at the University of Chicago in 1964. Between 1963 and 1966, the interest in ^{99m}Tc grew as its numerous applications, as a radiotracer and diagnostic tool. By 1966, BNL was unable to cope with the demand for ^{99}Mo/^{99m}Tc generators and withdrew from production and distribution, in favor of commercial generators. [6]

1.1.3 Highly Enriched Uranium (HEU) Method

HEU is the most popular method in the current ^{99}Mo production system. HEU includes enough ^{235}U to maintain a chain reaction. However the ^{235}U used in the production of ^{99}Mo is a critical component for both civil nuclear power generator and military nuclear weapons. [6] This creates concern on the International Atomic Energy Agency (IAEA). IAEA attempts to monitor and control enriched uranium supplies and processes in its efforts to ensure nuclear power generation safety. [6]

In recent years, HEU method has become less and less favorable due to its environmental impact. The byproducts during the HEU process are not useful and become radioactive waste, which impact both human and environmental health. As a result, many alternative methods of producing ^{99}Mo without using HEU have been introduced and implemented.

5

1.1.4 Low Enriched Uranium (LEU)

As people have noticed the dangers of HEU process LEU is considered to be enhanced with less than 20% of ^{235}U. Fresh LEU in research reactor is usually enriched 12% to 19.75% ^{235}U. [6]

A big advantage of using LEU target is the reduction of nuclear proliferation concerns. However, a drawback of producing ^{99}Mo from LEU target is that they contain, by definition, less than 20% of fissile ^{235}U and as a consequence the produced ^{99}Mo has a very low specific activity, about five times lower compared to that produced from HEU. [6]

1.1.5 Neutron Activation

The production of ^{99}Mo by neutron activation of enriched ^{98}Mo target in a reactor is considered to be an attractive alternative to the HEU ^{99}Mo production. A disadvantage of this method is that the specific activity of ^{99}Mo produced by this procedure is low because of the small neutron capture cross section at the thermal neutron energy 0.14barn (1barn is equal to $10^{-24}\ cm^2$). Another reason why the ^{99}Mo production by this process has a very low specific activity is that most of the molybdenum in the product is ^{98}Mo. [6]

1.1.6 Photon Induced Reaction ^{100}Mo(γ, n) ^{99}Mo in Accelerator

This method uses an electron beam to generate high-intensity photons which in turn would be used to initiate the nuclear reaction on enriched ^{100}Mo such as ^{100}Mo(γ, n)^{99}Mo reaction which creates the desired product. [6] A very high intensity

beam is needed to overcome the factor of about 1000 times smaller cross section for this reaction versus neutron fission of ^{235}U, although the fission yields are almost identical (nearly 6%). [6]

One of drawbacks for Photon Induced Reaction method is the high cost of the multiple machines that are required for the operation. However, in 1998, researchers from Ukraine, published their results on ^{99}Mo production by targeting ^{100}Mo with an energetic electron beam produced by the linac according to the charged particle reaction ^{100}Mo(γ, n) ^{99}Mo. They concluded that the proposed technique has the promise of returning very high profits in a not too distant future. [6]

1.1.7 Overview of Non-HEU processes

An over view of non-HEU process of producing ^{99}Mo is shown in Figure 1.1.
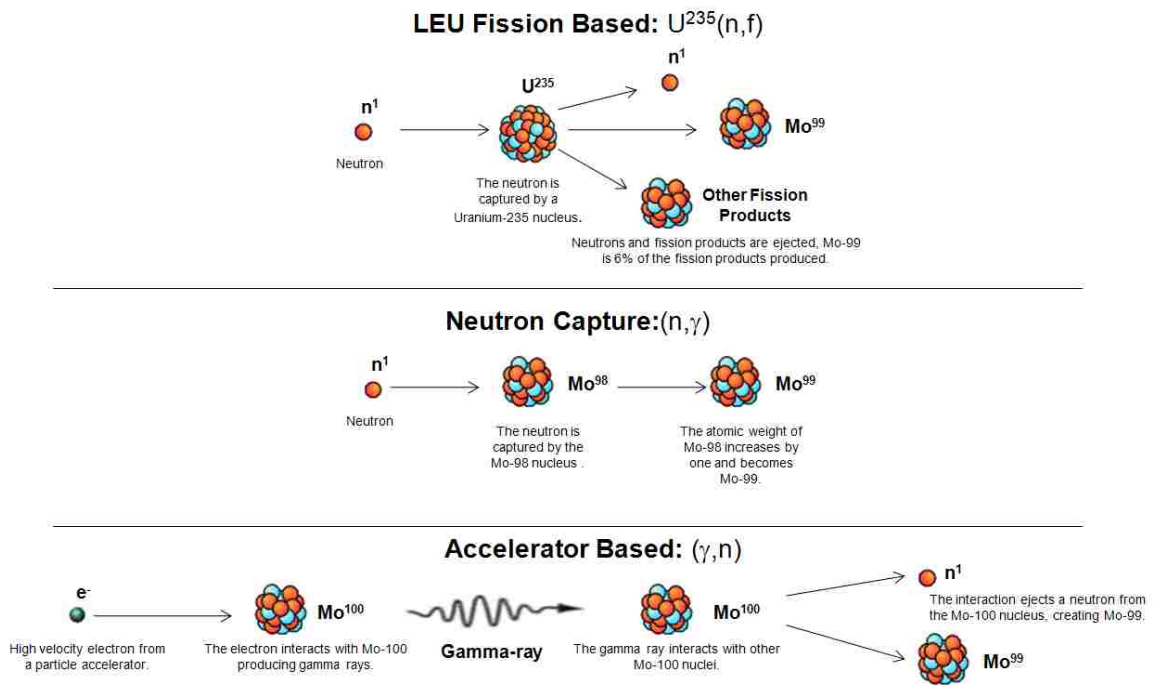
Figure 1.1: GTRI and U.S Domestic Mo-99: Non-HEU Production Methods

7

1.2 Overview of Proposed Method

The method that has been proposed for this project to produce reliable ^{99}Mo is to use a combination of an electron accelerator and a two-column chromatographic separation technique. [7] As mentioned early in section 1.1.6, the electron accelerator causes a ^{100}Mo$(\gamma, n)^{99}$Mo reaction when a high-intensity electron beam is sent through a ^{100}Mo target, and the ^{99m}Tc is extracted using NorthStar's two-column generator. The steps of this process can be found in Figure 1.1.

During the production of ^{99}Mo when using the new proposed method a large amount of heat is deposited into the target disks, which will directly affect the performance of the production, therefore the additional heat must be removed. The main purpose of thesis work is to investigate a new cooling design to improve the heat removal from the target disks.

When the new production method is completely implemented, the production rate of ^{99}Mo will be increased significantly compared to all other methods. The amounts of radioactive waste create during the process will be minimized and reduced to a point that they can be recycled back into the system.

1.3 Target Cooling System

During the production process, the electron bean from the accelerator deposits a significant amount of the beam power into the target as heat. The size of the target, and therefore the production density, is limited by the thermal performance of the target. [2] For the first few tests, water was introduced as the cooling agent. However, multiple evidence showed ^{99}Mo was detected in the cooling water, a conclusion was made that the

targets were not only being oxidized but were being eroded by the cooling water. The oxidization of the targets was most likely being caused by free radical and peroxide formation in the cooling water through radiolysis of the water by incident electron beam. [2]

1.3.1 Cooling Fluid Selection

Losing the enriched [100]Mo material during the production process is not acceptable. The expense of the material will increase the cost of the project; therefore a different kind of cooling fluid must be used to replace water.

A series of inert gas cooling systems were proposed to replace the water cooling system. A comparison was conducted to determine which inert gas is the best candidate for this project. Table 1.2 [7] gives the properties for the proposed inert gases. These properties are based on the assumption that the each enters the channel at 25 °C, has an inlet pressure of 300 pisa, and a pressure drop of 15 pisd. [7]

Table 1.2: Gas Coolant Properties

Property	H_2	He	Ne	N_2	SF_6	CO_2	Ar
k (W/m·K)	0.168	0.142	0.046	0.024	0.012	0.015	0.016
c_p (J/g·K)	14.32	5.19	1.03	1.04	0.58	0.84	0.52
c_v (J/g·K)	10.16	3.12	0.62	0.74	0.53	0.66	0.31
Density (kg/m^3)	1.67	3.34	16.87	23.39	121.95	36.75	33.33
Velocity (m/s)	514.0	363.4	161.7	137.4	60.2	109.6	115.1
Mach Number	0.39	0.36	0.36	0.39	0.44	0.41	0.36
Mass Flow Rate (g/s)	4.3	6.1	13.6	16.1	36.7	20.1	19.2
Reynolds Number	92082	58403	156545	248740	433932	255686	158793
Prandtl Number	0.757	0.724	0.372	0.533	0.771	0.867	0.748
Nusselt Number	196	134	237	387	683	465	302
h (W/m^2·K)	34614	20023	11432	9742	8600	7125	5077

When focusing on the heat transfer property of each gas, hydrogen outperforms any of those inert gases shown above. However, due to its combustion ability when mixed with air at high temperature (500 °C) hydrogen gas cannot be used in this system. When eliminate hydrogen gas, helium gas becomes the best choice among all other gases shown above.

1.3.2 Once-through Cooling System

As a proof of principle, a once-through helium gas cooled target was demonstrated using the electron accelerator facility at ANL in 2011. This cooling system used 20 large compressed gas bottle of helium as the supply of the cooling gas. A picture of the gas manifold and bottles is shown in Figure 1.2. [2]

The flow of the helium gas was regulated from the bottle manifold pressure down to the target inlet pressure of ~2 MPa by a high flow regulator. Due to the expansion through the regulator the helium gas became very cold; it was then passed through a gas to water heat exchanger. To control the flow rate of the helium a regulating valve was installed downstream of the target. From the regulating valve, the helium was passed through a HEPA filter and exhausted into the room ventilation system. [2]

Figure 1.2: Photograph of the Helium Gas Bottle and Gas Manifold Used During the Once-through Helium Gas Cooled Thermal Test Using the Electron Accelerator at ANL in March 2011

With the setup, a thermal test was conducted at ANL in 2011. The electron beam used in the test was set as follows: 17 MeV, 10.3 KW, 6 mm FWHM. The twenty large bottles of helium provided about 20 minutes of run time at full flow rate, and reached a peak velocity of 200 m/s, which cooled of peak heat flux of ~800 W/cm^2. The result from this experiment determined that the heat fluxes on the order of 1000 W/cm^2 or more were within reach with helium gas cooling. [2]

1.3.3 Closed Loop Helium Gas Cooling System

With the success of the once-through cooling system a closed loop helium gas cooling system was designed and installed at ANL. The main driving force for the flow is a three-lobe-roots-type blower, and it is contained within a pressurized system. A roots

blower is typically characterized by a high mass flow rate but a fairly low pressure rise (~100 KPa). To achieve a high target inlet pressure of ~2 MPa (290 Psi), and hence a higher gas density and mass flow rate, the roots blower is enclosed in a pressure vessel that is pressurized very near the desired target inlet pressure. In this fashion, the roots blower is only required to overcome the dynamic pressure losses in the system, which is well within the capabilities of a roots blower, and not have to achieve the full static inlet pressure of the target. A picture of the pressure vessel, roots blower, and motor installed at ANL is shown in Figure 1.3. [2]

The schematic of the closed loop is shown in Figure 1.4 and an engineering drawing of the layout in the accelerator vault is shown in Figure 1.5. From the blower outlet on the pressure vessel, the helium gas is piped to a heat exchanger which serves as an after cooler. The helium gas is heated as it is compressed by the blower, and the after cooler is used to remove this heat. The helium is then piped to a filter to remove any oil or particulates in the gas. From the filter, the helium is piped to the target. [2]

Temperature is monitored by a set of thermocouples installed on the inlet and outlet of the target. Temperature data gathered from the thermocouples can be used to calculate the power removed from the target.

In addition to the thermocouple, a simple screen filter is installed at the downstream of the target to trap pieces of target if it were dissembled during the irradiation. [2]

After helium left the filter, it passed through another heat exchanger which is used to remove the heat absorbed in the helium from the target. From the heat exchanger, the

inlet temperature of the cooling water was~25 °C and the volumetric flow rate was ~11 gpm. After exiting from the second heat exchanger, the helium flowed through a coriolis flow meter which is used to measure the mass flow rate of the helium. From the flow meter, the helium is flowed back to the pressure vessel and the cycle starts all over again. [2]

Similar loop is now built at LANL and ready to be used for the experimental part of this project.

Figure 1.3: Photograph of the Roots Blower (Left) and Motor (Right) Mounted to a Plate Cantileverd of the End of the Pressure Vessle Flange Plate. The Other End of the Pressure Vessel Slides Back and Forth Over the Motor and Blower on Rails Bolted to the Skid Plate
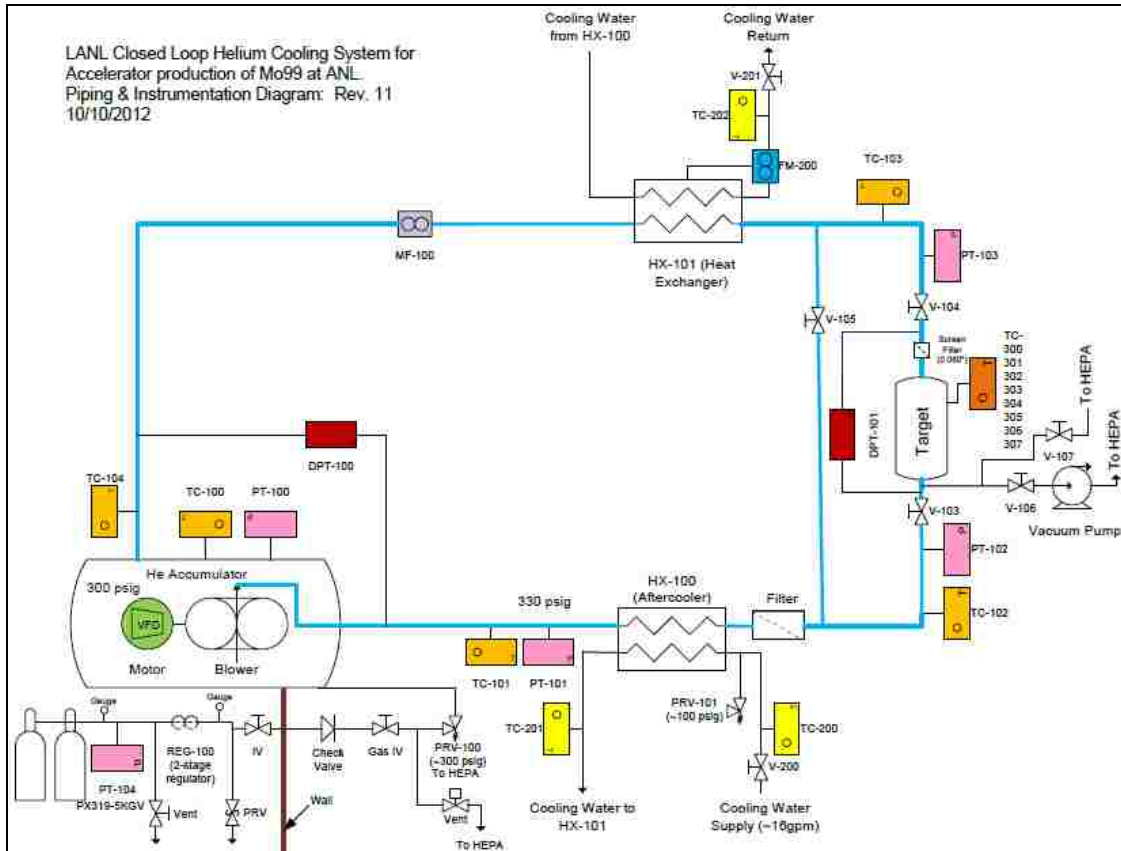
Figure 1.4: P&ID of the Production System
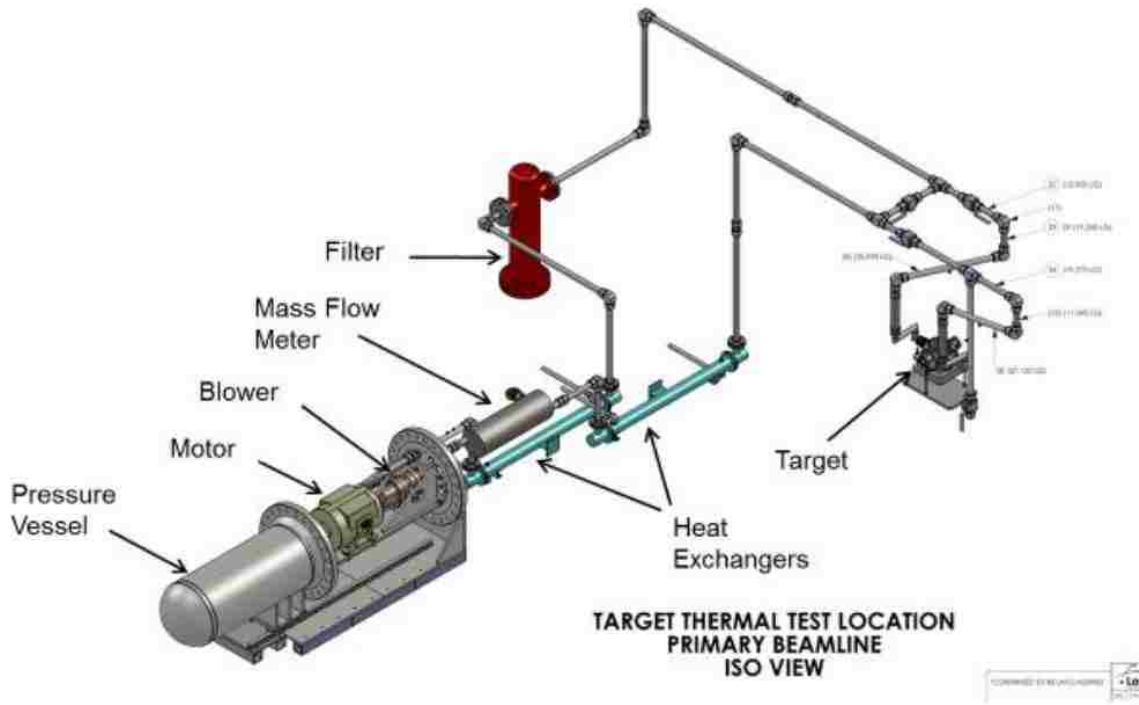
Figure 1.5: Piping Layout for the Helium Target Cooling System.

1.3.4 Flow Properties

According to the energy equation shown in Eq.(1.1). [8] The heat transfer coefficient is directly related to the mass flow rate. When the heat capacity $\bar{c}_p$ and the temperature difference are fixed; increase mass flow rate will directly increase the heat transfer coefficient.

$$\dot{Q} = \dot{m}\bar{c}_p(\bar{T}_2 - \bar{T}_1) \tag{1.1}$$

Maximizing mass flow rate can be achieved by changing the target geometry and the initial conditions of the flow loop. The main focus of this thesis project will be put on the design of the target geometry. Assuming the initial condition of the flow loop has already been maximized; a series of parametric studies on the target geometry will be

15

tested and compared. Close attention will be put on several parameters and they are: maximum and average velocities at different section of the target, mass flow rate at the inlet and outlet, and the dynamic pressure at the inlet region. The new design of the target geometry should able to reduce the target wall temperature to between 550 °C and 650 °C as described earlier in this chapter.

Chapter 2 - Theory and Methodology

2.1 Mach Number Calculation

Mach number is simply described as ratio of object speed over speed of sound. It is a dimensionless number that is useful for analyzing fluid dynamics problems to determine if a flow can be treated as an incompressible flow. The Mach number can be expressed as shown in Eq. (2.1). [9]

$$M = \frac{v}{v_{sound}} \tag{2.1}$$

Alternatively the Mach number can be expressed with the density and the bulk modulus of elasticity as Eq. (2.2). [9]

$$M = v\left(\frac{\rho}{E}\right)^{\frac{1}{2}} \tag{2.2}$$

If M < 0.3 and the flow is isothermal and quasi-steady, compressibility can be neglected, therefore incompressible flow model can be used.

Since the acoustic disturbance introduced in a point is very small the heat transfer can be neglected and for gases assumed isentropic. For an isentropic process the ideal gas law can be used and speed of sound can be expressed as shown in Eq. (2.3) [10]

$$v_{sound} = (kRT)^{\frac{1}{2}} \tag{2.3}$$

2.2 Density Calculation

Gases are highly compressible in comparison to liquids, which changes in density directly related to changes in pressure and temperature through the Eq. (2.4) [11]

$$\rho = \frac{p}{RT} \tag{2.4}$$

Eq. (2.4) is commonly termed the ideal or perfect gas law, or the equation of state for an ideal gas. It is known to closely approximate the behavior of real gases under normal conditions when the gases are not approaching liquefaction. [11]

2.3 Confined Flows

In many cases the fluid is physically constrained within a device so that its pressure cannot be prescribed. Such cases include nozzles and pipes of variable diameter for which the fluid velocity changes because the flow area is different from one section to another. For these situations it is necessary to use the concept of conservation of mass (the continuity equation) along with Bernoulli equation. Consider a fluid flowing through a fixed volume that has one inlet and one outlet. If the flow is steady so that there is no additional accumulation of fluid within the volume, the rate at which the fluid flows into the volume must equal the rate at which it flows out of the volume (otherwise, mass would not be conserved). [11]

The mass flow rate from an outlet can be calculated as shown in Eq. (2.5). [11]

$$\dot{m} = \rho Q \tag{2.5}$$

The volume flow rate Q can be related directly to the cross-sectional area A, and it can be expressed as shown in Eq. (2.6). [11]

$$Q = VA \tag{2.6}$$

Thus, mass flow rate $\dot{m}$ can be reconstructed as shown in Eq. (2.7). [11]

$$\dot{m} = \rho V A \tag{2.7}$$

To conserve mass, the inflow rate must equal the outflow rate. If the inlet is designated as (1) and outlet as (2), it follows that $\dot{m}_1 = \dot{m}_2$. Thus, conservation of mass requires [11]:

$$\rho_1 V_1 A_1 = \rho_2 V_2 A_2 \tag{2.8}$$

If the density remains constant, then $\rho_1 = \rho_2$, and the above becomes the continuity equation for incompressible flow [11]:

$$V_1 A_1 = V_2 A_2, or \ Q_1 = Q_2 \tag{2.9}$$

2.4 Reynolds Number

The Reynolds number is undoubtedly the most famous dimensionless parameter in fluid mechanics. It is named in honor of Osborne Reynolds (1842-1912), a British engineer who first demonstrated that this combination of variables could be used as a criterion to distinguish between laminar and turbulent flow. In most fluid flow problems there will be a characteristic length, ℓ, and a velocity, V, as well as the fluid properties of density, ρ, and viscosity, μ, which are relevant variables in the problem. Thus, with these variables the Reynolds number can be expressed as shown in Eq. (2.10). [11]

$$Re = \frac{\rho V \ell}{\mu} \qquad (2.10)$$

The Reynolds number is a measure of ratio of the inertia force on an element of fluid to the viscous force on an element. When these two types of forces are important in a given problem, the Reynolds number will play an important role. [11]

2.5 CFD Models

To properly characterize the flows that are in the cooling channels a turbulence model is needed. The candidate turbulence model should be able to capture the fluid interaction with the boundaries (walls) and initial conditions (inlet and outlet).

Initially both standard (SKW) and SST k-ω (SSTKW) models were conducted for this project; the final decision on the turbulence model will be validated and announced in the later chapter. Many studies show that both SKW and SSTKW models agree reasonably well with experimental data from Obi [12] and LES results from Kaltenback [13]. In addition, both SKW and SSTKW models have been known to obtain good results for flows that involve separation and reattachment.

Many commercial software packages are available for this CFD project and most are constructed and configured in a similar fashion. They are usually integrated systems, which include a mesh generator, a flow solver, and a visualization post processing tool. Most of the CFD codes are using popular algorithms that are published in the literature, for instance, standard k-ω model from Wilcox [14] , SST k-ω model developed by Menter [15], and one of most popular models standard k-ε model proposed by Launder

and Spalding [16]. The selections of these models are based on their robustness and reliability.

There are many popular commercial software packages recommended by multiple literatures, and they are CFX, Fluent, and Star-CD. However, ANSYS Fluent 14.5 version is chosen by the recommendation from El-Behery's [17] asymmetric diffuser study. The models comparison and their theory behind them are presented in section 2.5.1.

2.5.1 Turbulence Models

The commercial code ANSYS Fluent solves a set of governing equations. The numerical method employed is based on the finite volume approach. Fluent provides flexibility in choosing discretization schemes for each governing equation. The discretized equations, along with the initial condition and boundary conditions, are solved using the segregated solution method. Using the segregated solver, the conservation of mass and momentum are solved sequentially and a pressure correction equation is used to ensure the conservation of momentum and the conservation of mass (continuity equation). Several turbulence models, such as, the standard k-ε model, the low-Re k-ε model, the standard k-ω model, the shear-stress transport k-ω model, the Reynolds stress model (RSM) and the v^2-f model are used in the literature to predict the separating flow through diffuser. [17] The first five models are available directly in FLUENT while the last one (v^2-f model) was implemented using user-defined functions (UDF) and user-defined scalars (UDS).

The steady Reynolds Averaged Navier-Stokes (RANS) equations for turbulent

21

incompressible fluid flow with constant properties are used in the present study. The governing flow field equations are the continuity and the RANS equations, which are given by [18]:

$$\frac{\partial u_i}{\partial x_j} = 0 \tag{2.11}$$

$$\frac{\partial u_i \partial u_j}{\partial x_j} = \frac{1}{\rho}\frac{\partial p}{\partial x_i} + \frac{\partial}{\partial x_j}(\nu S_{ij} - \overline{u_i' u_j'}) \tag{2.12}$$

Where S_{ij} is the main strain rate and calculated by [18]:

$$S_{ij} = \frac{1}{2}\left(\frac{\partial u_i}{\partial x_j} + \frac{\partial u_j}{\partial x_i}\right) \tag{2.13}$$

It is an unfortunate fact that no single turbulence model is universally accepted as being superior for all classes of problems. The choice of turbulence model will depend on considerations such as the physics of the flow, the established practice for a specific class of problem, the level of accuracy required, the available computational resources, and the amount of time available for the simulation. To make the most appropriate choice of model for ones' application, one needs to understand the capabilities and limitations of the various options. [18]

However, in the literature, many results show that standard k-ω, SST k-ω, and v^2-f models clearly performed better than other models. They show an acceptable agreement with the velocity and turbulent kinetic energy profiles provided by Obi [12], Buice, and Eaton [19]. Since v^2-f model cannot be directly obtained from ANSYS Fluent

and requires additional UDF and UDS, standard and SST k-ω models are more suitable than v^2-f model. Standard and SST k-ω models can be directly obtained from ANSYS Fluent, and the ANSYS FLUENT Theory Guide gives a detailed explanation on standard and SST k-ω model as well as other popular turbulent models.

For this project, only three turbulent models are reviewed and all three of them are used to compare against the experimental data provided by Buice and Eaton. The three models are: Standard k-ε, Standard k-ω, and SST k-ω models. By doing the comparison, one can prove that the new FLUENT solver can still be valid to obtain a reliable solution as El-Behery did with FLUENT 6.3.26 version.

Two-equation models are historically the most widely used turbulence models in industrial CFD. They solve two transport equations and model the Reynolds Stresses using the Eddy Viscosity approach. The standard k-ε model in ANSYS FLUENT falls within this class of models and has become the workhorse of practical engineering flow calculations in the time since it was proposed by Launder and Spalding [16]. Robustness, economy, and reasonable accuracy for a wide range of turbulent flows explain its popularity in industrial flow and heat transfer simulations. The drawback of some k-ε models is their insensitivity to adverse pressure gradients and boundary layer separation. They typically predict a delayed and reduced separation relative to observations. This can result in overly optimistic design evaluations for flows, which separate, from smooth surfaces (aerodynamic bodies, diffusers, etc.). The k-ε model is therefore not widely used in external aerodynamics [18].

The standard *k-ε* model is a model based on model transport equations for the

turbulence kinetic energy (k) and its dissipation rate (ε). The model transport equation

for k is derived from the exact equation, while the model transport equation for ε was

obtained using physical reasoning and bears little resemblance to its mathematically exact

counterpart [18].

The standard k-ε model is valid only for fully turbulent flow. It assumes that the

flow is fully turbulent, and the effects of molecular viscosity are negligible [18].

The turbulence kinetic energy, k, and its rate of dissipation, ε are obtained from

the following transport equations:

$$\frac{\partial}{\partial t}(\rho k)+\frac{\partial}{\partial x_i}(\rho k u_i)=\frac{\partial}{\partial x_j}\left[\left(\mu+\frac{\mu_t}{\sigma_k}\right)\frac{\partial k}{\partial x_j}\right]+G_k+G_b-\rho\varepsilon-Y_M+S_k$$

(2.14)

And

$$\frac{\partial}{\partial t}(\rho\varepsilon)+\frac{\partial}{\partial x_i}(\rho\varepsilon u_i)=\frac{\partial}{\partial x_j}\left[\left(\mu+\frac{\mu_t}{\sigma_\varepsilon}\right)\frac{\partial\varepsilon}{\partial x_j}\right]+C_{1\varepsilon}\frac{\varepsilon}{k}(G_k+C_{3\varepsilon}G_b)-C_{2\varepsilon}\rho\frac{\varepsilon^2}{k}+S_\varepsilon$$

(2.15)

In these equations, G_k represents the generation of turbulence kinetic energy due

to the mean velocity gradients. G_b is the generation of turbulence kinetic energy due to

buoyancy. Y_M represents the contribution of the fluctuating dilation in compressible

turbulence to the overall dissipation rate. $C_{1\varepsilon}, C_{2\varepsilon}$, and $C_{3\varepsilon}$ are constants. σ_k and σ_ε are

turbulent Prantl numbers for k and ε, respectively. S_k and S_ε are user-defined source

terms [18].

The standard k-ω model in ANSYS FLUENT is based on the Wilcox model [14] ,

which incorporates modifications for low-Reynolds number effects, compressibility, and

shear flow spreading. One of the weak points of the Wilcox model is the sensitivity of the solutions to values for k and ω outside the shear layer (free stream sensitivity).While the new formulation implemented in ANSYS FLUENT has reduced this dependency, it can still have a significant effect on the solution, especially for free shear flows [18].

The standard k-ω model is an empirical model based on model transport equations for the turbulence kinetic energy (k) and the specific dissipation rate (ω), which can also be thought of as the ratio of ε to k [18].

As the k-ω model has been modified over the years, production terms have been added to both the k and ω equations, which have improved the accuracy of the model for predicting free shear flows [18].

The turbulence kinetic energy, k, and the specific dissipation rate ω, are obtained from the following transport equations;

Turbulence Kinetic Energy:

$$\frac{\partial(\rho k)}{\partial t} + \frac{\partial(\rho k u_j)}{\partial x_j} = \tau_{ij}\frac{\partial u_i}{\partial x_j} - \beta^*\rho k \omega + \frac{\partial}{\partial x_j}\left[(\mu + \sigma_{k1}\mu_T)\frac{\partial k}{\partial x_j}\right] \qquad (2.16)$$

Specific Turbulence Energy Dissipation Rate:

$$\frac{\partial(\rho\omega)}{\partial t} + \frac{\partial(\rho\omega u_j)}{\partial x_j} = \alpha\frac{\omega}{k}\,\tau_{ij}\frac{\partial u_i}{\partial x_j} - \beta_1\rho\omega^2 + \frac{\partial}{\partial x_j}\left[(\mu + \sigma_{w1}\mu_T)\frac{\partial\omega}{\partial x_j}\right] \qquad (2.17)$$

Where ,

- τ_{ij} is the Reynolds stress tensor

- $\tau_{ij}\frac{\partial u_i}{\partial x_j}$ is the production of turbulence kinetic energy

- $\beta^* \rho k \omega$ is the dissipation of turbulence kinetic energy

- $\alpha \frac{\omega}{k} \tau_{ij} \frac{\partial u_i}{\partial x_j}$ is the production of specific turbulence energy dissipation rate

- $\beta_1 \rho \omega^2$ is the dissipation of the specific turbulence energy dissipation rate

- $\alpha, \beta_1, \beta^*, \sigma_{k1}, \sigma_{w1}$ are closure coefficients

All of these closure coefficients provided above are based on the experimental data gathered from the benchmark tests to the models. A comparison between Wilcox [14] and ANSYS FLUENT's [18] closure coefficients on the standard k-ω is shown in Table 2.1.

Table 2.1: Standard k-ω Model Closure Coefficients Comparison

Coefficient	Wilcox	Fluent
α	0.09	0.09
β_1	0.5	0.5
β^*	0.56	0.52
σ_{k1}	0.075	0.072
σ_{w1}	0.5	0.5

The shear-stress transport (SST) *k-ω* model was developed by Menter [15] to effectively blend the robust and accurate formulation of the *k-ω* model in the near-wall region with the free-stream independence of the *k-ε* model in the far field. To achieve this, the *k-ε* model is converted into a *k-ω* formulation. The SST *k-ω* model is similar to the standard *k-ω* model, but includes the following refinements [18]:

- The standard *k-ω* model and the transformed *k-ε* model are both multiplied by a blending function and both models are added together. The blending function is designed to be one in the near wall region, which activates the

standard k-ω model, and zero away from the surface, which activates the transformed k-ε model.

- The SST model incorporates a damped cross diffusion derivative term in the ω equation.

- The definition of the turbulent viscosity is modified to account for the transport of the turbulent shear stress.

- The modeling constants are different.

These features make the SST k-ω model more accurate and reliable for a wider class of flow (for example, adverse pressure gradient flows, airfoils, transonic shock waves) than the standard k-ω model.

Menter's SST k-ω model is formulated in the form of:

Turbulence Kinetic Energy:

$$\frac{\partial(\rho k)}{\partial t} + \frac{\partial(\rho k u_j)}{\partial x_j} = \tau_{ij}\frac{\partial u_i}{\partial x_j} - \beta^* \rho k \omega + \frac{\partial}{\partial x_j}\left[(\mu + \sigma_k \mu_T)\frac{\partial k}{\partial x_j}\right] \qquad (2.18)$$

Specific Turbulence Energy Dissipation Rate:

$$\frac{\partial(\rho\omega)}{\partial t} + \frac{\partial(\rho\omega u_j)}{\partial x_j} = \alpha\frac{\omega}{k}\,\tau_{ij}\frac{\partial u_i}{\partial x_j} - \beta_2\rho\omega^2 + \frac{\partial}{\partial x_j}\left[(\mu + \sigma_{w2}\mu_T)\frac{\partial\omega}{\partial x_j}\right] +$$
$$2\rho(1-F_1)\sigma_{\omega2}\frac{1}{\omega}\frac{\partial k}{\partial x_j}\frac{\partial\omega}{\partial x_j} \qquad (2.19)$$

Where the blending function $F_1 = \tanh(\emptyset_1^4)$, and $\emptyset_1$ can be obtained as follow:

$$\emptyset_1 = \min\left[max\left(\frac{\sqrt{k}}{0.09\omega y}; \frac{500\mu}{\rho y^2 \omega}\right), \frac{4\rho\sigma_{\omega 2}k}{y^2 CD_{kw}}\right] \tag{2.20}$$

$$CD_{kw} = \max\left(2\rho\sigma_{\omega 2}\frac{1}{\omega}\frac{\partial k}{\partial x_j}\frac{\partial \omega}{\partial x_j}, 10^{-20}\right) \tag{2.21}$$

Where variable y is the distance from the nearest wall. Table 2.2 shows the closure coefficient between Menter [15] and fluent [18] model.

Table 2.2: SST k-ω Model Closure Coefficients Comparison

Coefficient	Menter	Fluent
σ_{k1}	0.85	1.176
σ_{k2}	1.0	1.0
$\sigma_{\omega 1}$	0.5	2.0
$\sigma_{\omega 2}$	0.856	1.168
α	0.31	0.31
β	0.075	0.075
β^*	0.09	0.0828

A benchmark problem constructed by El-Behery [17] will be used in Chapter 3 to validate the candidate turbulence models mentioned in this section.

Chapter 3 - CFD Model Development

This section describes the CFD model development by using the ANSYS Fluent 14.5 software package. Two separate cases were studied for the [99]Mo project; one for simple single channel flow and other for complex multi-channels flow.

For single channel study, both El-Behery [17] and Lan's [20] experimental comparison data were used to validate the model chosen for this project. For multi-channel case, the CFD result was compared directly to in-house experimental data that was measured at LANL.

From the initial comparison, single channel is more for an academic study, which represents the ideal case of a simple flow through a channel. The single channel study has been well published in the literature. A benchmark problem from El-Behery's study was used to finalize the turbulence model use for this project. A parametric study on the diffuser angle was conducted and a correlation between diffuser angle and flow separation was developed and compared against Lan's result. In this study, an ideal case can be obtained; with certain diffuser angles the flow separation can be completely eliminated. Even though, the single channel study does not directly reflect the actual behavior of the fluid flow that is performed from the actual production, it is still useful when trying to get a quick solution when optimizing the channel geometry, it can be used to eliminate some of the design process for the multi-channels model. When it comes to computational performance, single channel requires much less computational time than the multi-channel study and still produces a reasonable result.

For multi-channels study, since the ideal flow can never been obtained, a complete different flow behavior was found compared to the single channel study. However, this study is more valuable than the single channel study for the [99]Mo project, since the actual production involves multiple targets and cooling channels. Since the flow separation can no longer be eliminated, reducing the flow separation has become the priority for this part of study. The result of this study is later compared to the experiment that is conducted in-house.

3.1 Geometry

For ANSYS Fluent, the very first step of the simulation is to construct geometry. An exploded ISO view of the target disks and holder is shown in Figure 3.1.
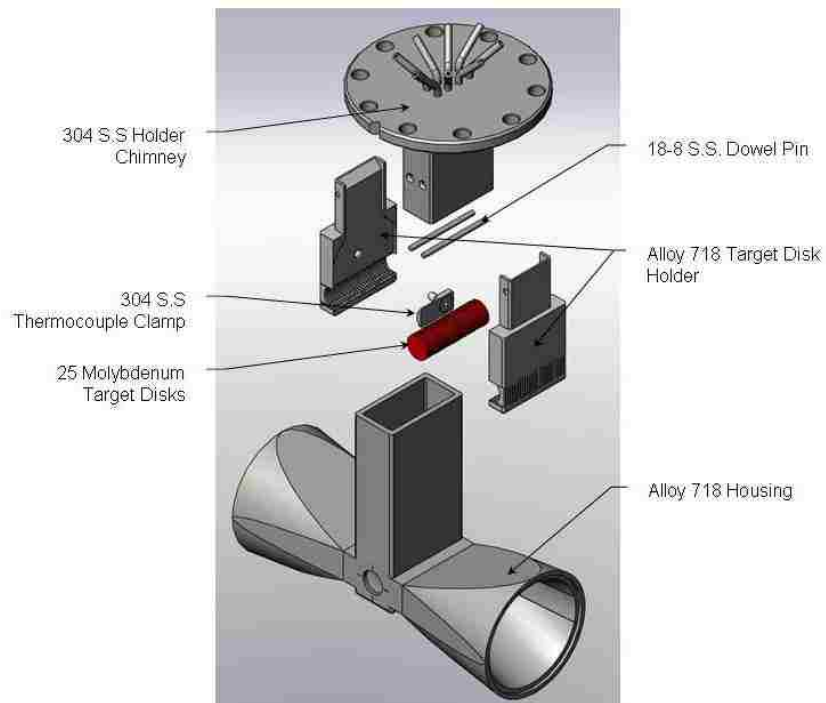
Figure 3.1: Exploded ISO view of housing, holder, and targets. Tubes that are located at the holder chimney flange are for thermocouple insertion.

To aid in mounting and aligning the target to the accelerator beam pipe, the target assembly was mounted inside a vacuum cube, as shown in Figure 3.2.
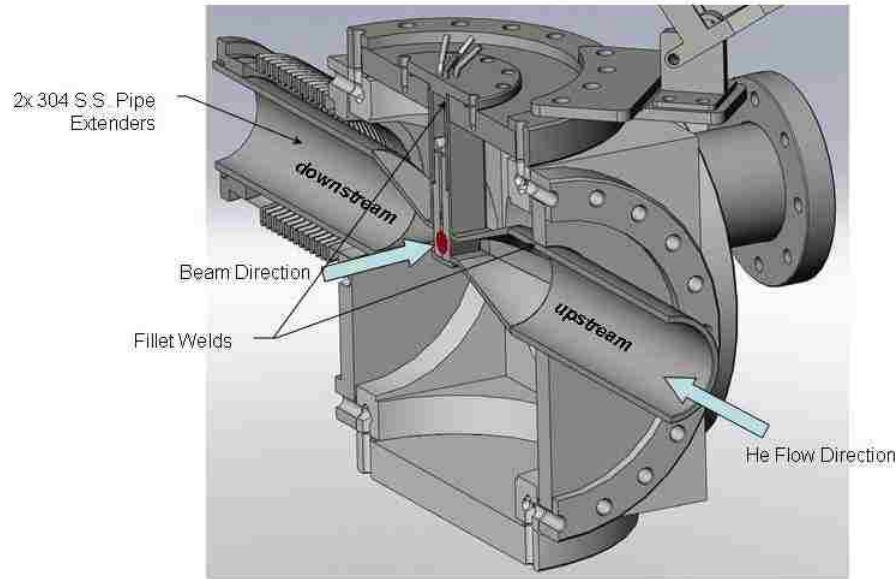
Figure 3.2: Cross-section view of Mo99 Target and Vacuum Cube Assembly showing assembly and weld locations.

For CFD simulation not all components are required to be modeled, the focus of this project is to model the test section, which only includes the ^{100}Mo target disks and the cooling channels in between the target disks.

The original configuration for the target disk was 12 mm in diameter and 1 mm thick, and featuring 0.5 mm wide channels in between disks. However, to increase the production rate a new configuration of the disk and the cooling channel is implemented. The target disk diameter is still 12 mm but with half of the thickness (0.5 mm), and there is also a 50% reduction (0.25 mm) on the width of the cooling channel. With the newest configuration of the target disk and the new design of the target holder, the total number of disks that can be fitted in the test section is now 82 instead of 25.

31

Figure 3.3 gives a demonstration of the configuration of the test section (this figure might not reflect to the actual production configuration). Two electron beams instead of one will be shot through the windows on both sides (front and back) normal to the disk faces, which will result in increase in production rate.
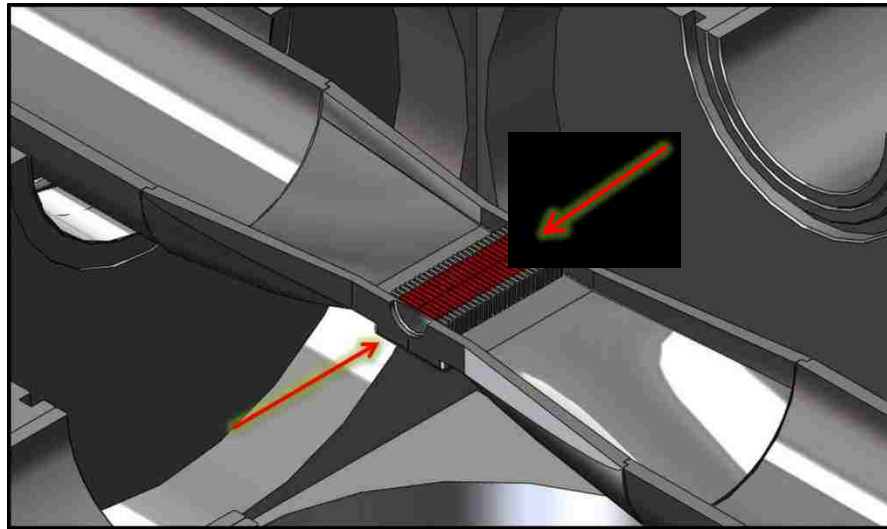
Figure 3.3: Target Disks and Production Configuration

3.2 Single Channel Model

The early phase of this project was to model a single helium flow channel instead of all cooling channels (83 channels). The main reason of doing this step is to quickly develop some fundamental knowledge of the fluid flow, and as mentioned before the result from the single channel study will also be used to eliminate some of the design process for the multi-channels model.

A base case CFD model was constructed to represent the original target cooling channel. The original target cooling channel has a sudden contraction and expansion inlet and outlet. Losses occur because of sudden change of inlet and outlet area. Because the fluid cannot turn a sharp right-angle corner, the flow is separated from the sharp corner,

which creates recirculation. The majority of the inlet head loss is due to inertia effects that are eventually dissipated by the shear stresses within the fluid. Only a small portion of the loss is due to the wall shear stress within the inlet region. The net effect is that the loss coefficient for a sudden contraction inlet could be high as $K_L = 0.50$, which means that one-half of a velocity head is lost as the fluid enters the channel. A similar effect applies to the outlet region, as the fluid leaves the smaller area and initially forms a jet-type structure as it enters the larger area. Within a few diameters downstream of the expansion, the jet becomes dispersed across the channel, and fully developed flow becomes established again. During this process, a portion of the kinetic energy of the fluid is dissipated as a result of viscous effects. [11] A demonstration of the original target cooling channel can be found in Figure 3.4.
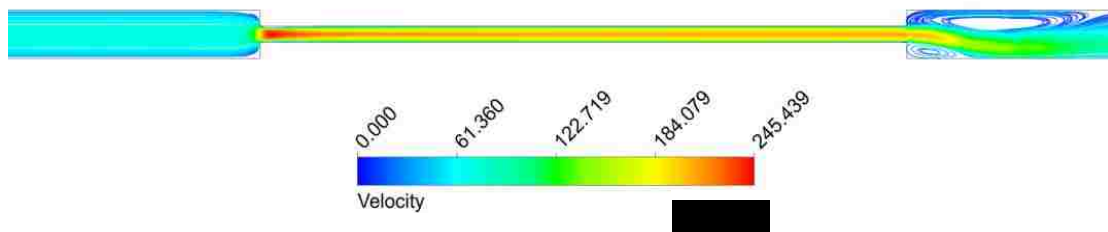
Figure 3.4: Original Target Cooling Channel (Single Channel Base Case)

An obvious way to reduce the loss is to add a more efficient feature to replace the sudden contraction and expansion inlet and outlet. Two designs were proposed for the inlet section; rounded and angled entrance. A diffuser design was introduced to minimize the loss coefficient at the outlet section. A comparison and final decision of the inlet and outlet features will be shown in Chapter 4 where the final result is provided.

3.2.1 Turbulence Model Validation

The fundamental process of turbulent flow separation has long been a troublesome calculation in the development of numerical turbulence models. Part of this difficulty can be traced to a limited database of experimental results for validation of flow models. Studies of turbulent flow in an asymmetric plane diffuser have been conducted independently by Obi et al [12]. and Buice and Eaton [19]. Using the experimental data of Buice as a benchmark, many studies had been conducted both experimentally and numerically on plane asymmetric diffusers. Many studies are compared to the results from turbulence models of varying complexity and their ability to accurately resolve the locations of separation and reattachment, as well as the velocity profiles through the diffuser. [21]
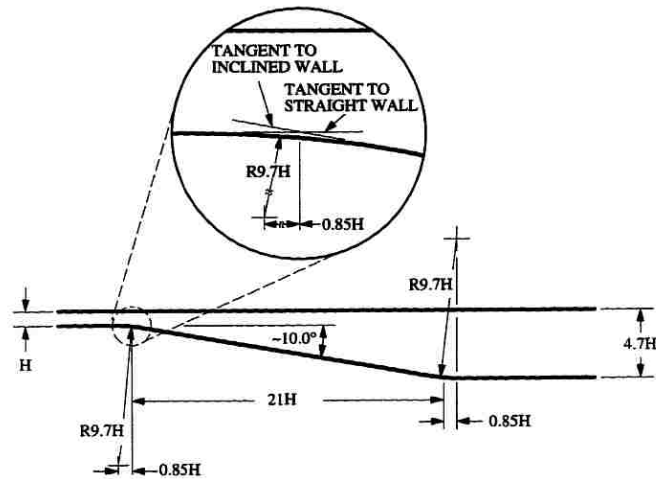

Figure 3.5: Obi's Diffuser Geometry

Figure 3.5 [12] shows the geometry of one of the very first asymmetric turbulent diffuser studies conducted by Obi et al [12]. The goal of his study was to validate a second-moment closure turbulence model for non-orthogonal numerical grids. A single-

component Laser Doppler Velocimetry (LDV) system was implemented with a Bragg cell frequency shift in a forward-scatter configuration. [21]

To validate the models that are used in this project, a benchmark problem was conducted. Figure 3.6, shows the popular benchmark problem that was constructed by El-Behery. He modeled the similar domain as Buice and Eaton did in their experiment and ran series of turbulent models on it. The axial velocity profile through the diffuser for the tested turbulent models was calculated and used to compare the experimental data gathered by Buice and Eaton.
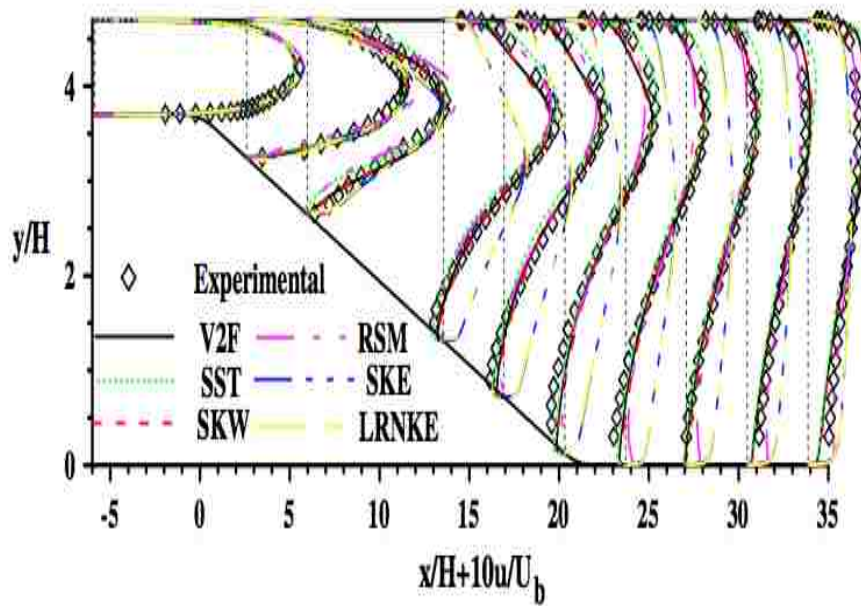
Figure 3.6: Development of axial velocity profile through the diffuser for the tested turbulence models compared with an experimental result of Buice-Eaton data. [19]

The result shown in Figure 3.6 is clear that the best model for diffuser flow are v^2-f, Standard k-ω, and SST k-ω model. These three models were able to predict the right physics from the experiment.
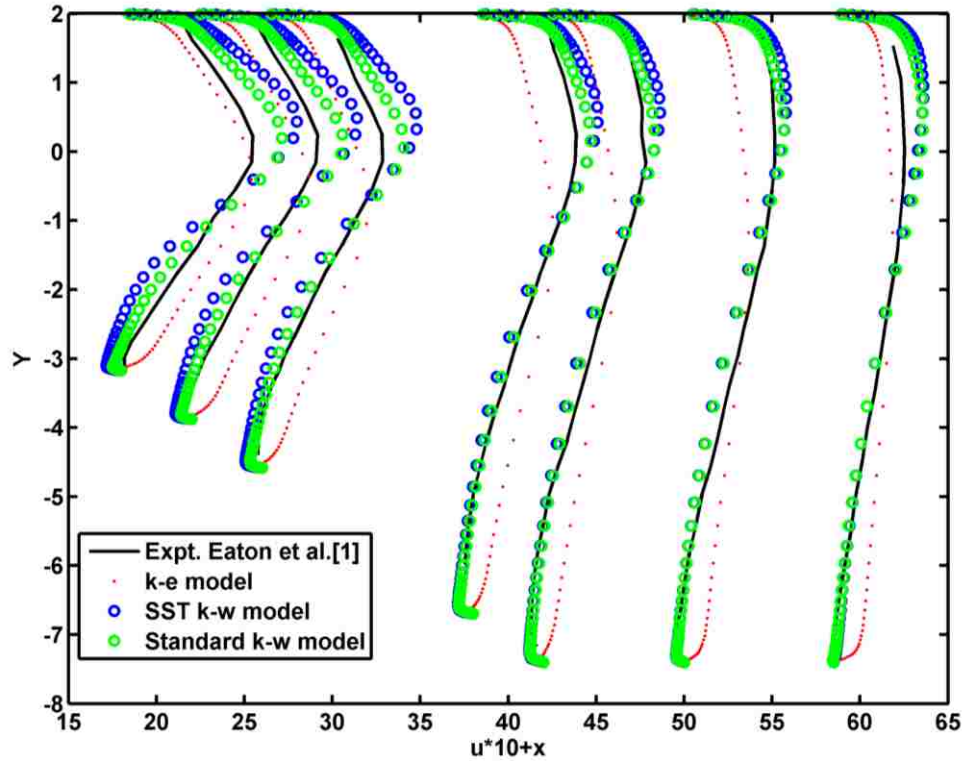
Figure 3.7: Mean Stream Velocity Comparison in a 10-Degree Diffuser (Model Validation)

By re-running El-Behery's simulation in ANSYS Fluent 14.5, three models were used to compare to Buice and Eaton's experimental data. In Figure 3.7, both standard and SST k-ω models show a better sign when matching the experimental data than standard k-ε model. This validation process proves that both standard and SST k-ω models are good candidates for this research project. However, a further testing and comparison are needed to confirm which model is truly the best model for the [99]Mo project.

3.2.2 Boundary Conditions and Model Inputs

The three-dimensional cooling channel model has three main parts: upstream inlet section, center cooling channel, and downstream outlet section with a diffuser design. All dimensions used in the simulation are reflected to the most current design that is sitting in the laboratory. The upstream inlet section has a duct height of 10.16 mm and width of

0.75 mm and featuring either a rounded or angled inlet (To be determined in next chapter). The center channel is constructed as a simple duct with duct height of 10.16 mm and width of 0.25 mm resulting in an expansion ratio of 3. Finally the downstream outlet section is featuring a diffuser design connected with an identical duct as the inlet section. All components are shown in Figure 3.8. Isothermal (at a temperature of 293 K), 1 atmosphere operating environment, and fully developed turbulent flows with helium gas as the medium are introduced to the system.
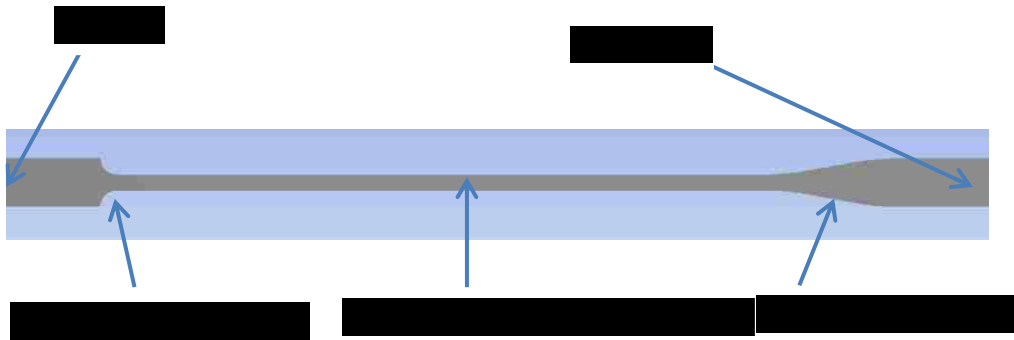
Figure 3.8: Single Channel Components

In addition to the selected turbulence models, a steady state pressure-based solver was selected along with a SIMPLE (Semi-Implicit Method for Pressure-Linked Equations) scheme. The inlet and outlet boundary conditions were set to pressure inlet and pressure outlet respectively. The gauge total pressure for inlet was set to 300 psi (2.07 MPa) and outlet was set to 285 psi (1.97 MPa) gauge pressure, which created a 15 psi pressure drop across the target cooling channel. Both inlet and outlet turbulence specification were set to a turbulence intensity of 5% coupled with their hydraulic diameter. Finally all walls were configured as stationary with no slip shear condition.

3.2.3 Mesh Development

A series of mesh resolution studies were conducted for all cases. A sample of rounded quarter circle inlet and 10-degree diffuser outlet is used in this section to show the grid independency of the simulation (See Figure 3.9 and Figure 3.10). A mesh biasing technique was introduced into this project, which is a non-uniform structured computational grid, where the finer grid is placed near the solid wall and region where the boundary layer is affective. With the higher grid density near the wall it is sufficient to capture the action near the boundary layer. In this study, growth ratio for the mesh was set to be no more than 1.2, which will help to keep the aspect ratio in a reasonable range.
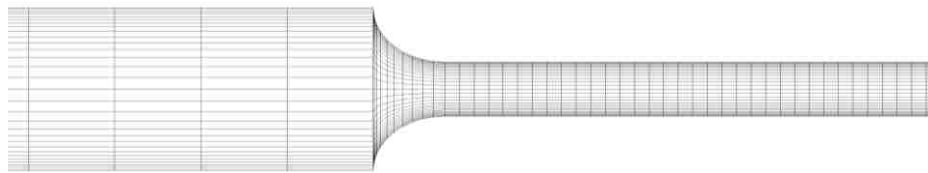

Figure 3.9: A Typical Mesh Used in the Calculation - Quarter Circle Inlet (438,216 Nodes)
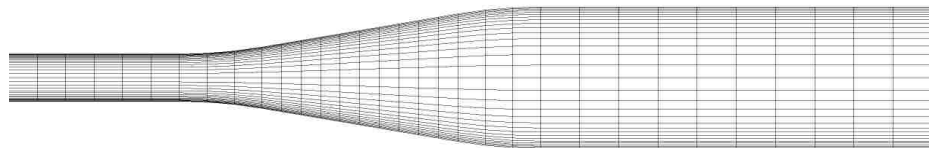

Figure 3.10: A Typical Mesh Used in the Calculation - Diffuser Outlet (438,216 Nodes)

Boundary layer theory was used to calculate the distance from the first boundary layer to the wall. The calculation for the distance to the wall is provided below:

$$Re_x = \frac{U_\infty x}{\nu} \tag{3.1}$$

$$v = \frac{\mu}{\rho} \tag{3.2}$$

$$C_f = [2 \log_{10}(Re_x) - 0.65]^{-2.3} \tag{3.3}$$

$$\tau_w = \frac{C_f \rho U_\infty^2}{2} \tag{3.4}$$

$$u_* = \sqrt{\frac{\tau_w}{\rho}} \tag{3.5}$$

$$y = \frac{y^+ v}{u_*} \tag{3.6}$$

Where,

Re_x = Reynolds number

v = Kinematic viscosity

C_f = Skin friction

τ_w = Wall shear stress

u_* = Friction velocity

y = Distance to the nearest wall

y^+ = Non-dimensional wall distance

Since the standard and SST k-ω models were chosen for this project, the recommendation from ANSYS fluent [18] is to use $y^+ \leq 5$. With input of Reynolds number $Re_x = 1.812 \times 10^4$ the distance to the nearest wall y was calculated to be 2.108×10^{-6} m. As a result, higher grid density was placed near wall than the center of the channel. An evidence of the mesh biasing result can also be found in Figure 3.9 and

Figure 3.10.

Mesh matrix was constructed to determine the independence of the model. To ensure the quality of each mesh configuration, two mesh quality measurements were used to determine the quality of the mesh; orthogonal quality and skewness. More information on these two measurements can be found as follows:

Orthogonal Quality:

- Orthogonal Quality ranges from 0 to 1, where values close to 0 correspond to low quality and value close to 1 correspond to high quality.

Skewness:

- Minimize equiangle skew:
    1. Hex and quad cells: skewness should not exceed 0.85.
    2. Tri's: skewness should not exceed 0.85.
    3. Tets: skewness should not exceed 0.9.

Skewness can be calculated as follow:

$$skewness = \frac{optimal\ cell\ size - cell\ size}{optimal\ cell\ size}$$

(3.7)

In Table 3.1 shows levels of quality of mesh based on the skewness number.

Table 3.1: Mesh Skewness

Value of Skewness	0-0.25	0.25-0.50	0.50-0.80	0.80-0.95	0.95-0.99	0.99-1.00
Cell Quality	excellent	good	acceptable	poor	sliver	degenerate

Three sets of meshes were compared as shown in Table 3.2.

Table 3.2: Single Channel Mesh Metrics

Turbulence Model	# of Nodes	# of Elements	Orthogonal Quality	Skewness	Mass Flow (g/s)	Max Channel Velocity (m/s)	Max Inlet Velocity (m/s)
SKW	59,136	51,750	0.986	2.29E-02	1.70	230.1	66.6
SKW	438,216	409,500	0.992	1.31E-02	1.76	259.0	69.1
SKW	788,020	742,800	0.994	1.14E-02	1.78	260.0	69.9
SSTKW	59,136	51,750	0.986	2.29E-02	1.90	259.6	74.2
SSTKW	438,216	409,500	0.992	1.31E-02	1.94	269.3	75.8
SSTKW	788,020	742,800	0.994	1.14E-02	1.94	270.3	75.9

All meshes provided in Table 3.2 were constructed as hex element; according to the two mesh quality measurements used in this study, all meshes studied here were high quality meshes. The mass flow, max channel velocity, and max inlet velocity data show a good sign of mesh convergence and independence when number of nodes reaches around 438,216. The mesh independence can also be proven visually by plotting the velocity profile along the mid-section of the channel. If the meshes are converged and have reached independence; their velocity profiles should be similar or close to each other. The visual evidence of mesh independence can be found in Figure 3.11 and Figure 3.12.

As expected from the result shown in Table 3.2; both Figure 3.11 and Figure 3.12 show good signs of mesh convergence. For both cases, the mid-section velocity profile for 438,216 nodes is almost completely overlaid on the velocity profile for 788,020 nodes. It is a sign of convergence and independence when two different high quality

meshes overlay each other. On the other hand, the velocity profile for 59,136 nodes is still far from reaching mesh independency.
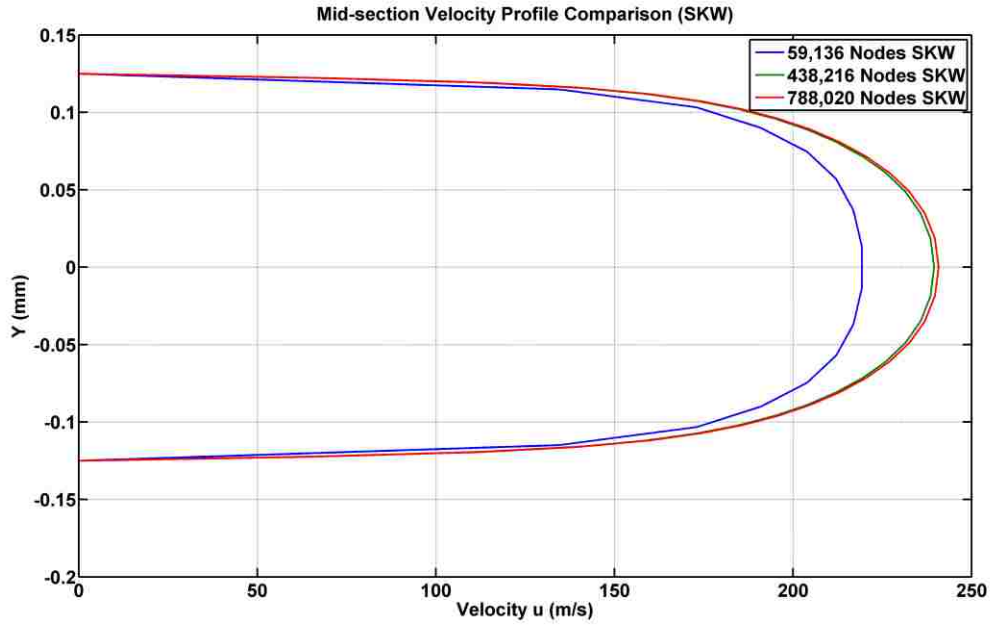

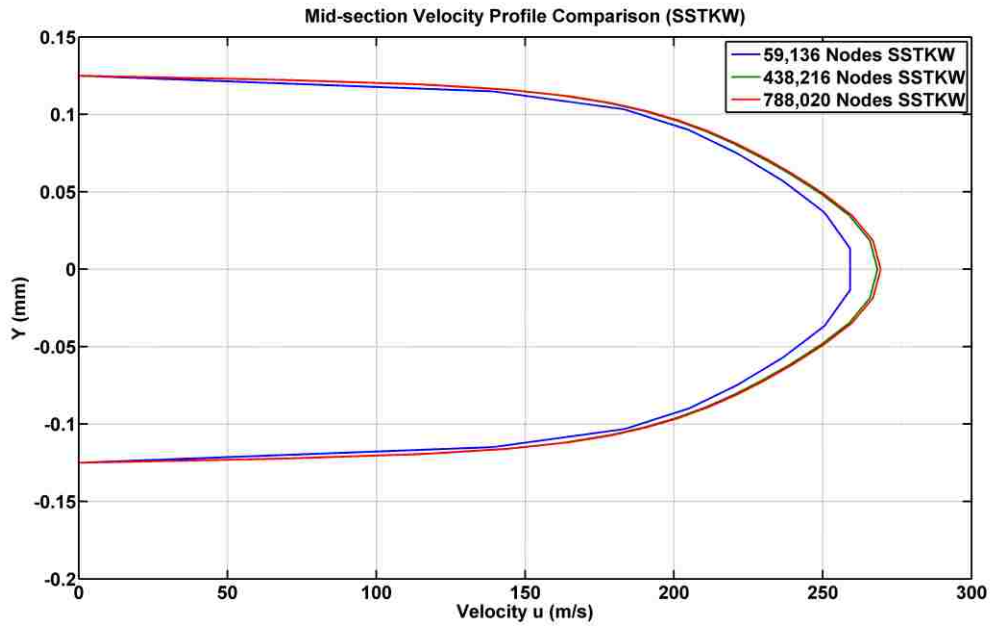Figure 3.11: Mesh Study – Mid-section Velocity Profile Comparison SKW Model

Figure 3.12: Mesh Study – Mid-section Velocity Profile Comparison SSTKW Model

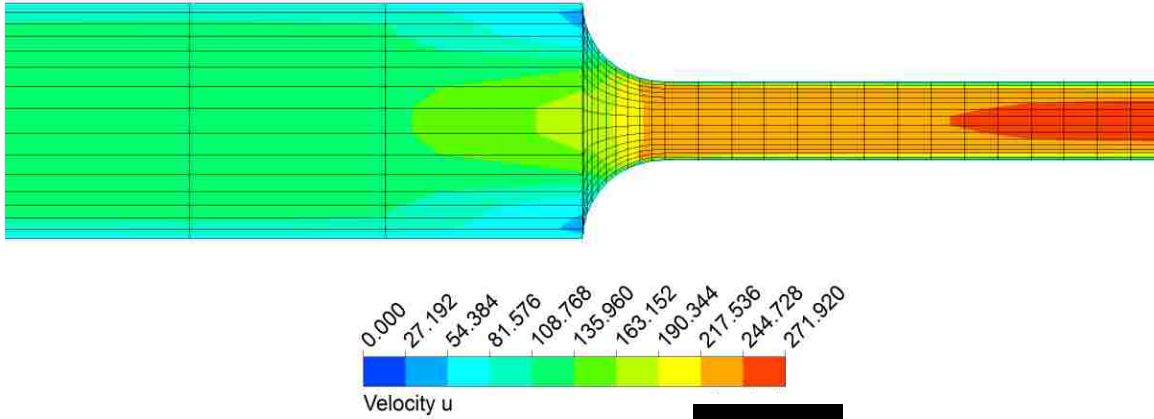An example of different mesh configurations can be found as follows:

Figure 3.13: Mesh Configuration - 59,136 Nodes Inlet

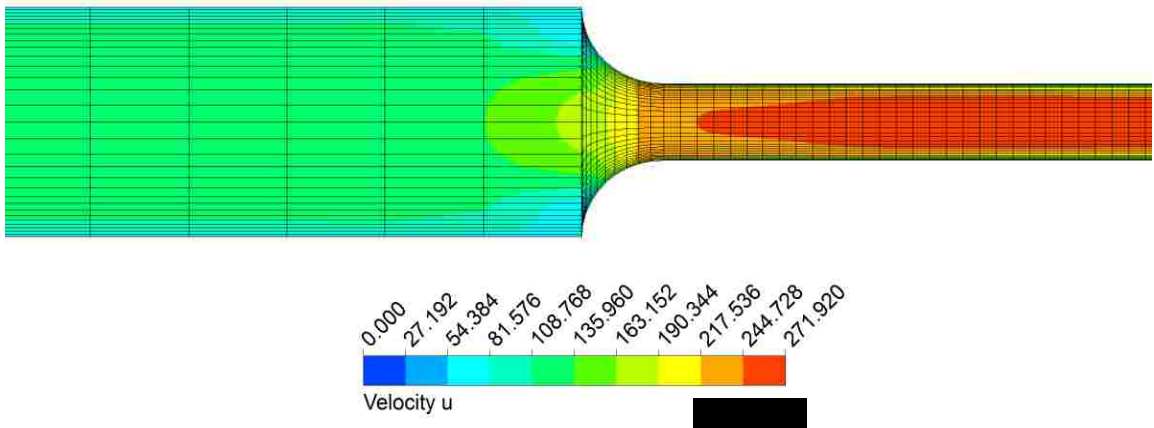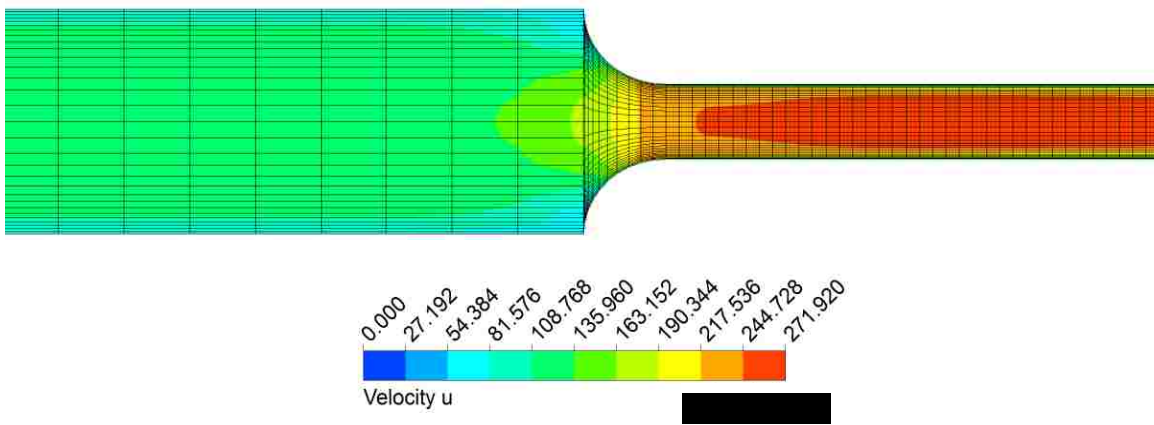Figure 3.14: Mesh Configuration - 438,216 Nodes Inlet

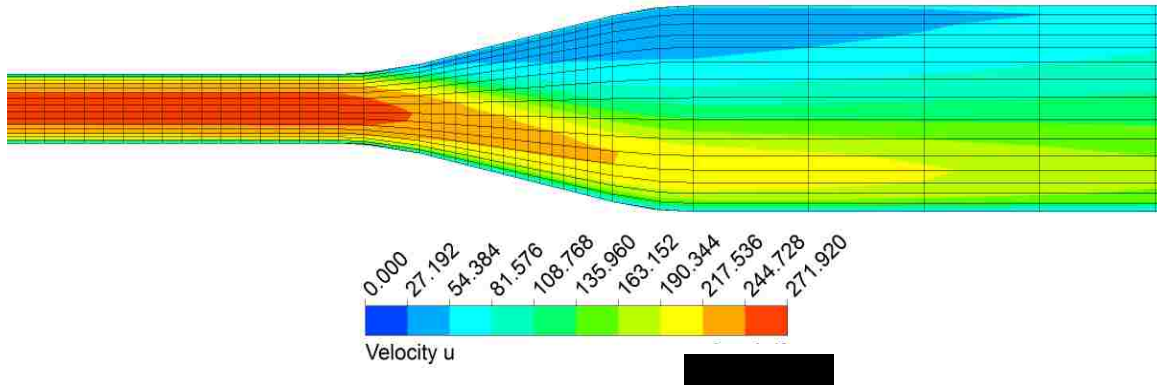Figure 3.15: Mesh Configuration - 788,020 Nodes Inlet

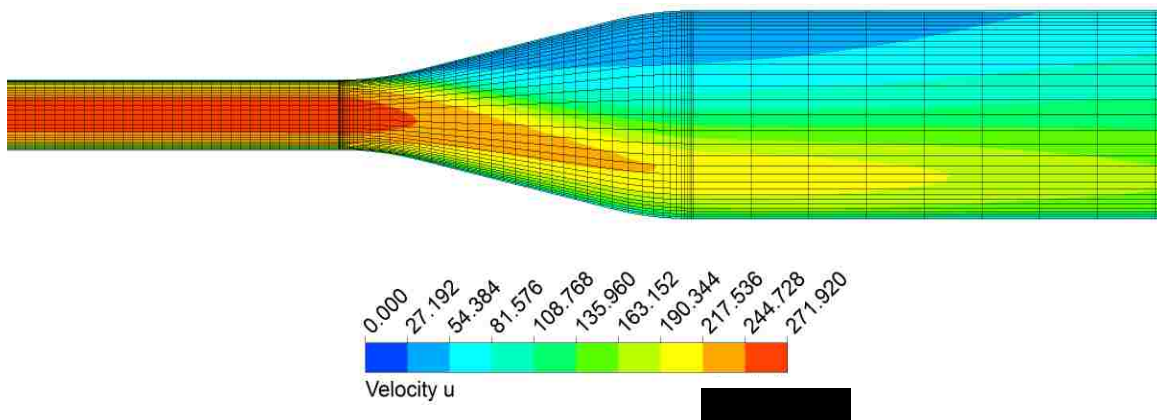Figure 3.16: Mesh Configuration – 59,136 Nodes Outlet

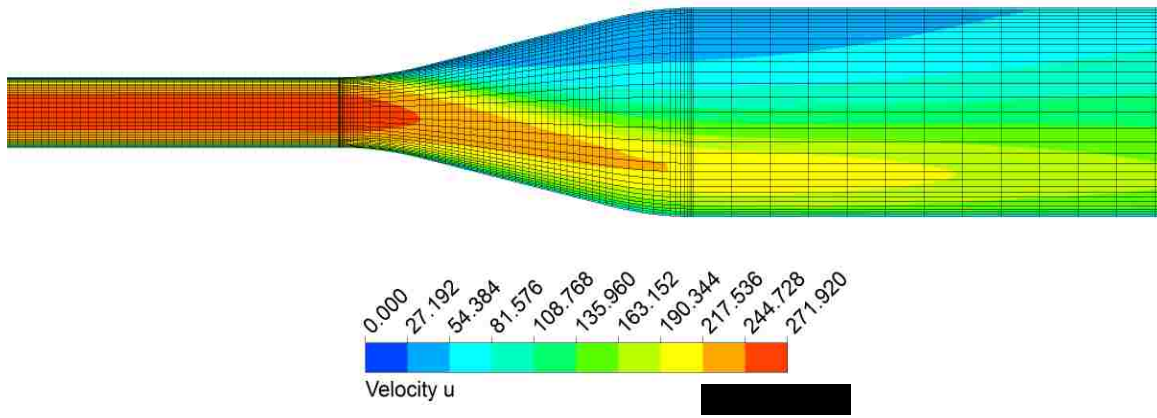Figure 3.17: Mesh Configuration - 438,216 Nodes Outlet

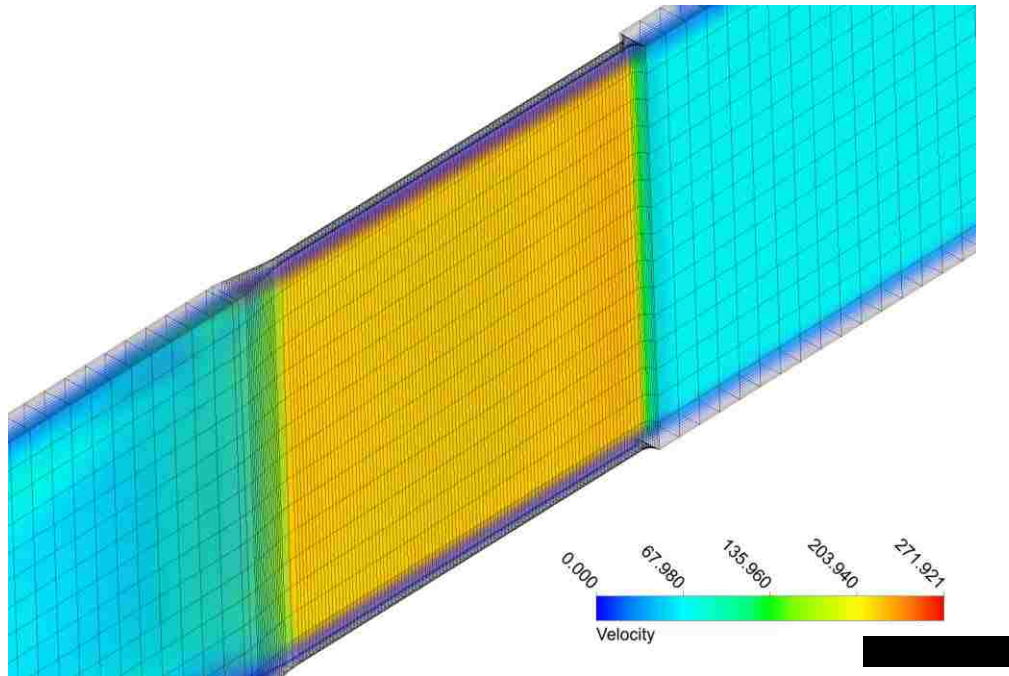Figure 3.18: Mesh Configuration - 788,020 Nodes Outlet

Figure 3.19: Mesh Configuration - 59,136 Nodes ISO View
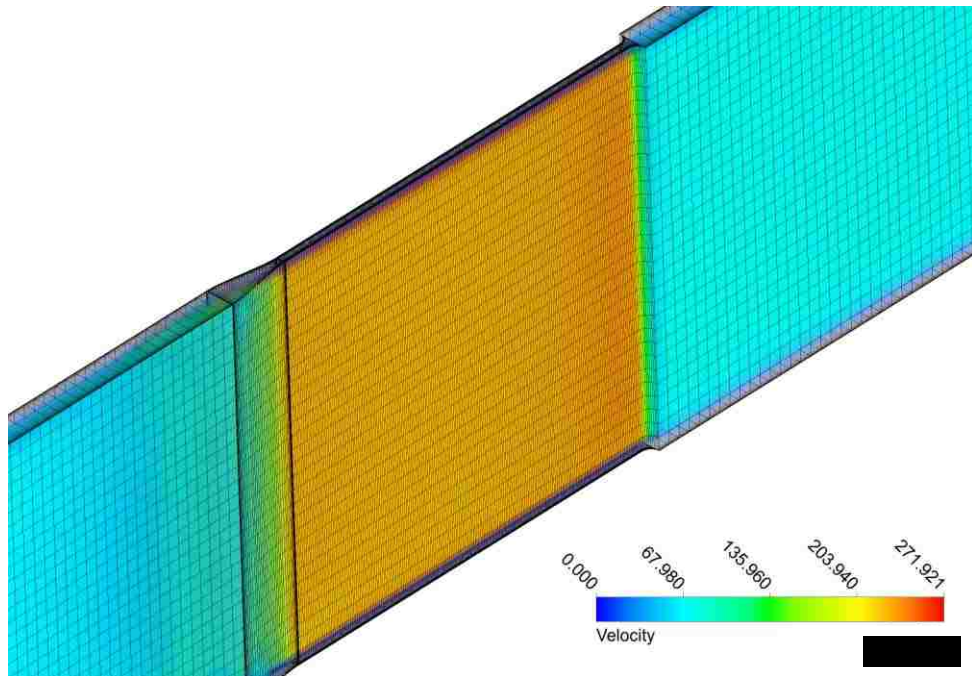
Figure 3.20: Mesh Configuration - 438,216 Nodes ISO View
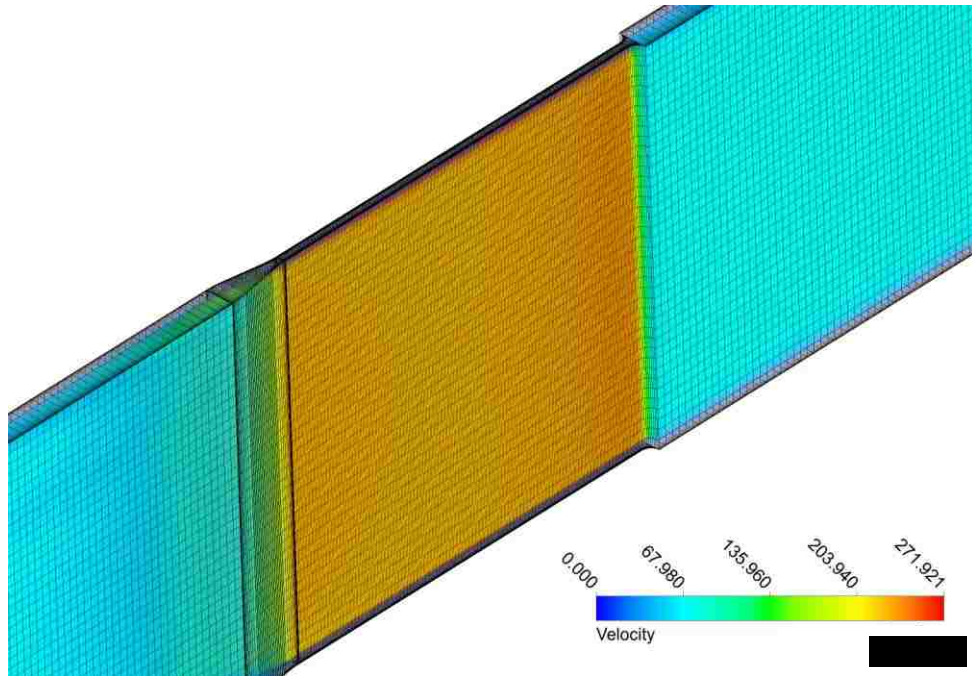
Figure 3.21: Mesh Configuration - 788,020 Nodes ISO View

3.2.4 Result Monitoring

To determine whether the result is converged and reached steady state or not many criteria were monitored. The most common criteria to be monitored are the default scaled residuals from ANSYS Fluent. There are six residuals being monitored for the standard and SST k-ω model and they are: Continuity, x-velocity, y-velocity, z-velocity, turbulence kinetic energy (k), and specific dissipation rate (ω). All residuals errors were set to 1e-6 to ensure steady state and convergence. A sample of scaled residuals can be found in Figure 3.22.

In addition to the scaled residuals, many other criteria can be monitored. Two additional criteria were monitored during the simulation: dynamic pressure at the inlet and mass flow rate at the outlet. Once the simulation is reached steady state these two criteria should become stable, in another word, they should stay (almost) constant. These

two criteria become extremely helpful when determining mesh convergence and independence for multi-channels simulation. Figure 3.23 and Figure 3.24 shown the solution is converged and reached steady state.

Figure 3.22: Scaled Residuals - Single Channel

Figure 3.23: Mass Flow Rate @ Outlet - Single Channel
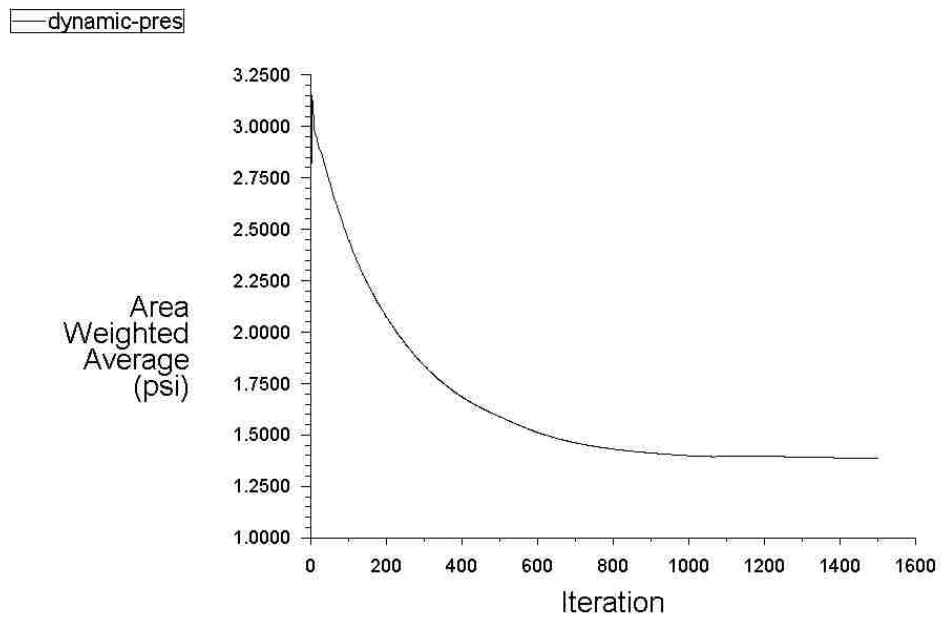
Figure 3.24: Dynamic Pressure @ Inlet - Single Channel
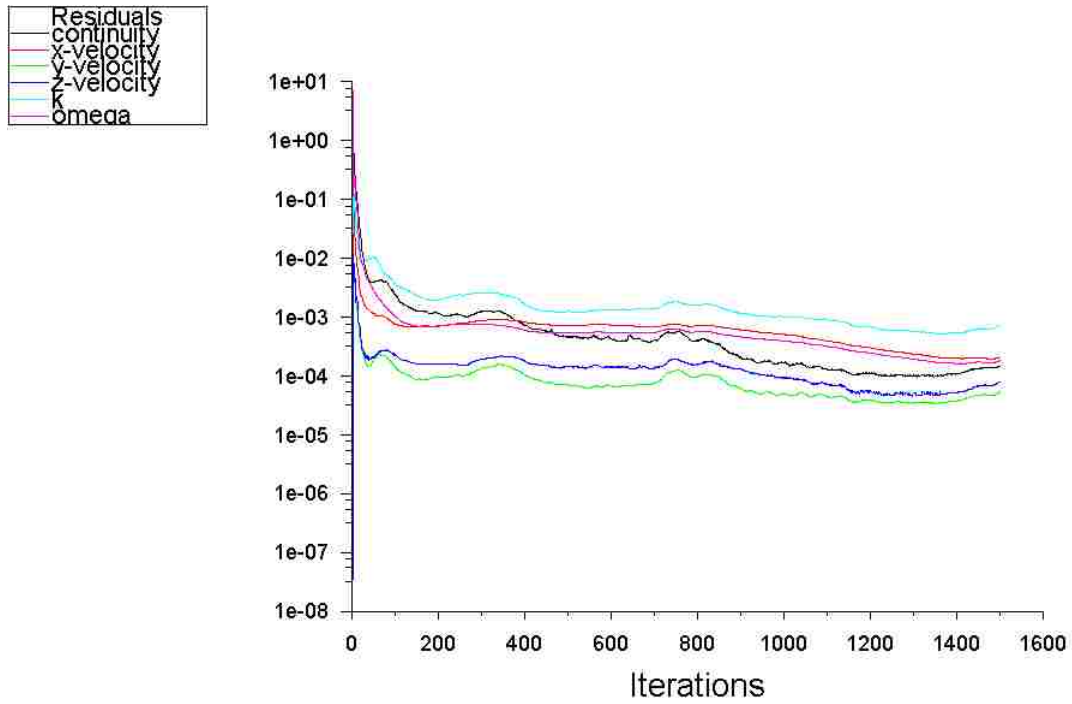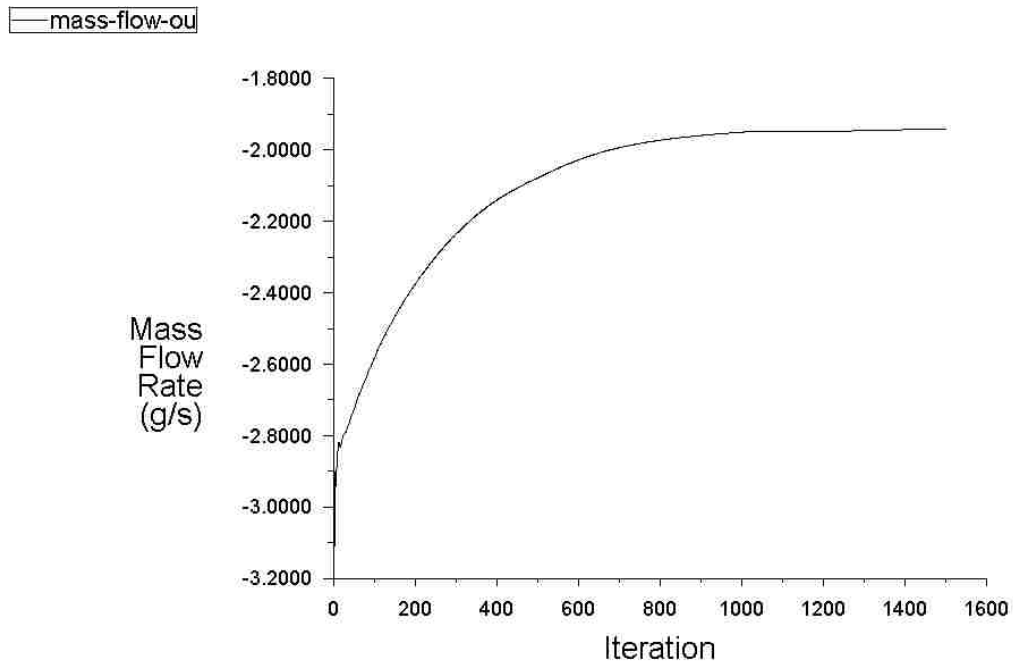
3.3 Multi-Channels Model

Similar procedures were used for the multi-channel model; since the initial and boundary conditions are the same as the single channel model.

3.3.1 Multi-Channels Boundary Conditions and Model Inputs

Multi-channel model was constructed by stacking numbers of single channel in parallel. Similar to the single channel model, multi-channels model also has three main parts: upstream inlet section, center cooling channel, and downstream outlet section with a diffuser design. The upstream inlet section has a duct height of 10.16 mm; the width of the inlet section will depended on the number of channels that are required to be simulated. The inlet section was constructed long enough to allow the fluid to become fully developed before it enters the center channel. A rounded or angled inlet will be determined in next chapter. No change on the center channel, for each channel, it was constructed as a simple duct with duct height of 10.16 mm and width of 0.25 mm. Finally the downstream outlet section is featuring a diffuser design connected with an identical duct as the inlet section. All components are shown in Figure 3.25. Isothermal (at a temperature of 293 K), 1 atmosphere operating environment, and fully developed turbulent flows with helium gas as the medium are introduced to the system.
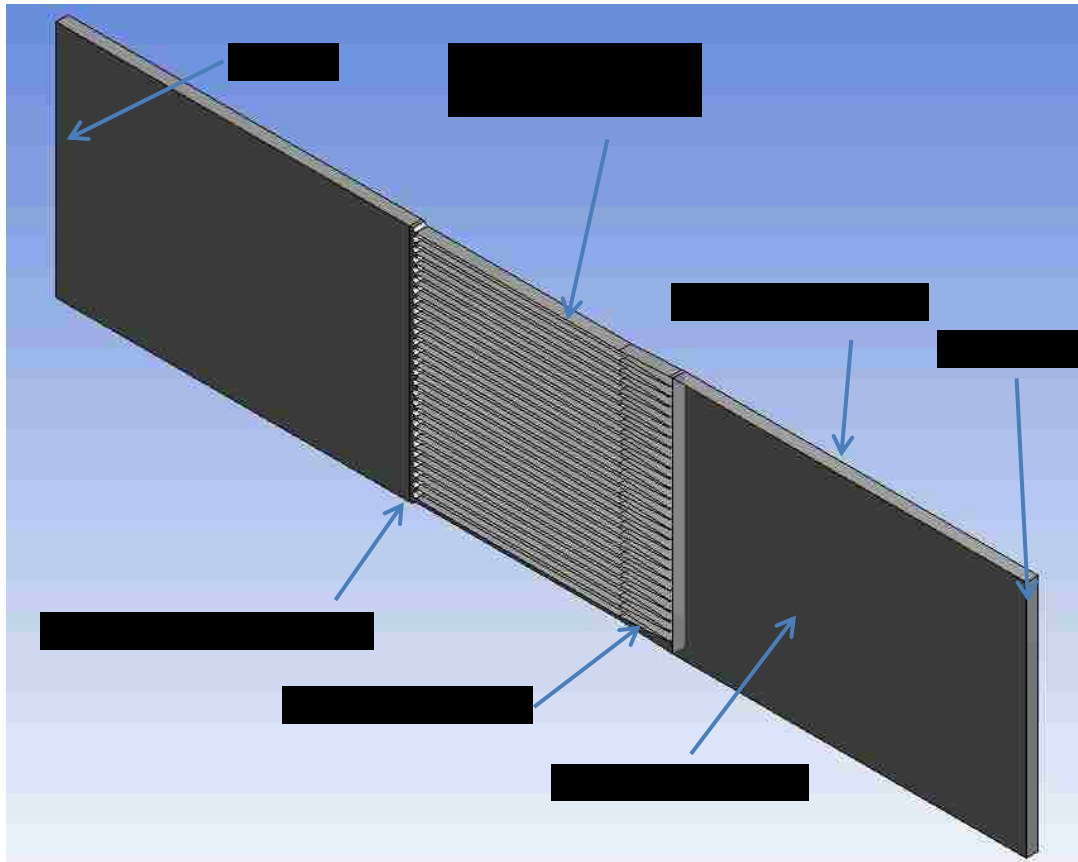
Figure 3.25: Multi-Channels Components

Same as the single channel simulation, a steady state pressure-based solver was selected along with a SIMPLE (Semi-Implicit Method for Pressure-Linked Equations) scheme. The inlet and outlet boundary consitions were set to pressure inlet and pressure outlet respectively. The gauge total pressure for inlet was set to 300 psi (2.07 MPa) and outlet was set to 285 psi (1.97 MPa) gauge pressure, which created a 15 psi pressure across the target cooling channel. Both inlet and outlet turbulence specification were set to a turbulence intensity of 5% coupled with their hydraulic diameter. Finally all walls were configured as stationary with no slip shear condition. To save computational time, symmetry boundary condition was used for the multi-channel simulation. As shown in Figure 3.25, symmetry boundary conditions were used on both side of the wall, This

allows us to only construct 1/10 of the entire domain and still maintain an accurate result. More detail on the 1/10 model will be explained in the later section.

3.3.2 Multi-Channels Mesh Development

Mesh development becomes extremely difficult when it comes to multi-channels simulation. The difficulty comes from the complexity of the transition region. Multiple mesh refinements are needed to develop a convergence and independence mesh.

Mesh biasing technique was also used for the multi-channels model; a growth ratio of 1.2 is enforced to keep the aspect ratio in a reasonable range. A sample of rounded quarter circle inlet and 4-degree diffuser outlet is used here to show the grid independency of the simulation (See Figure 3.26, Figure 3.27, and, Figure 3.28).
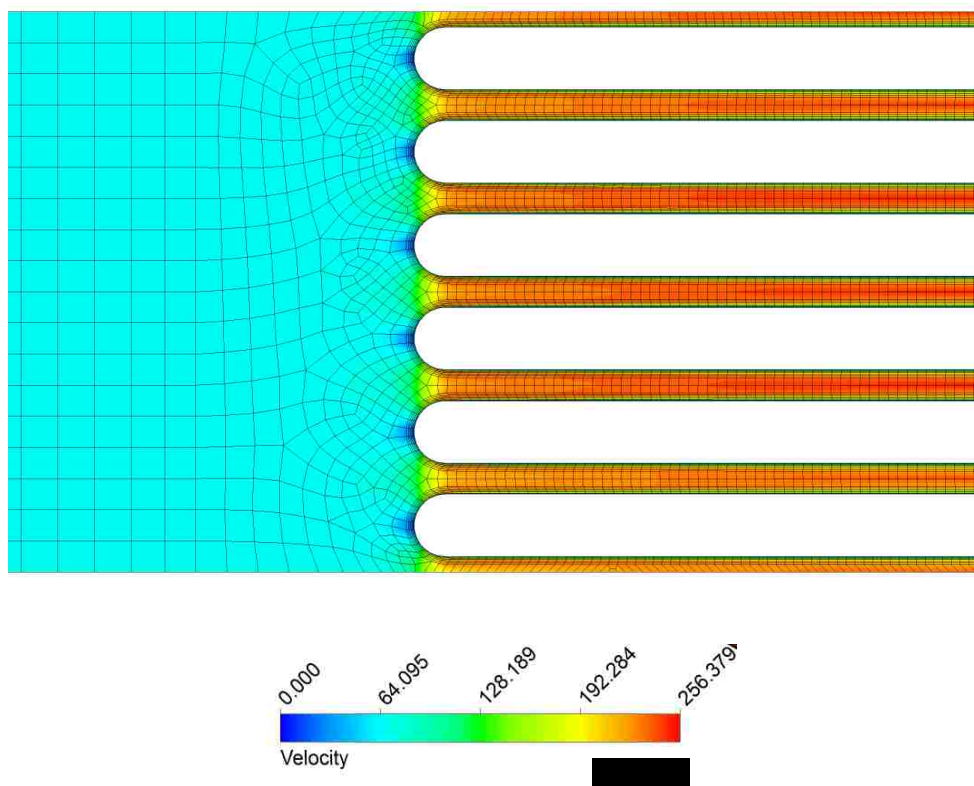

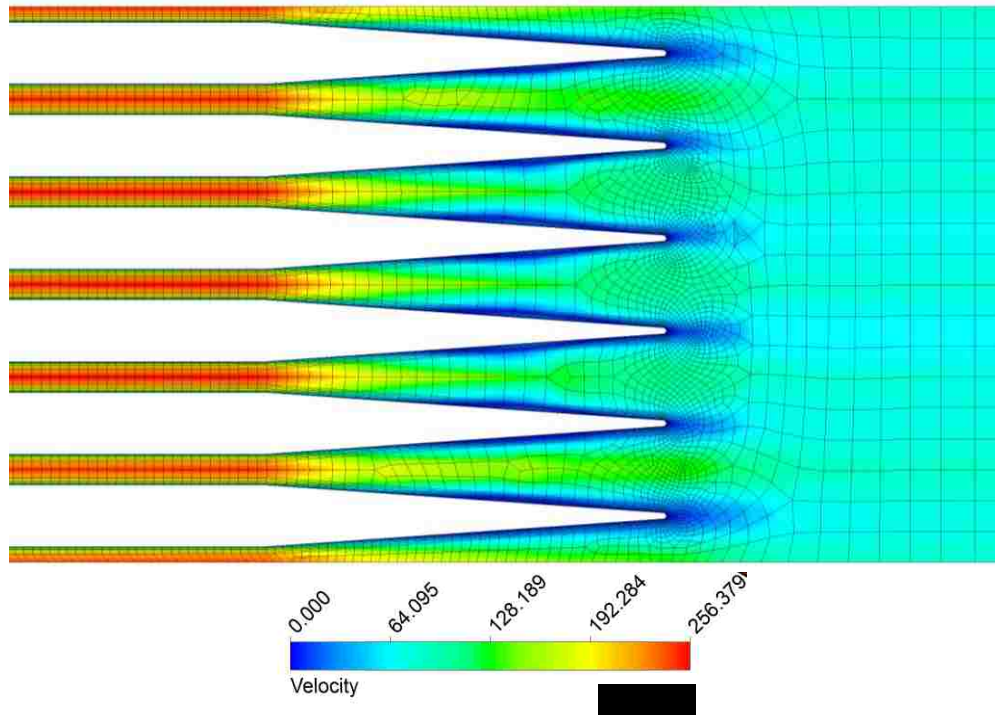Figure 3.26: Quarter Circle Inlet (2,392,054 Nodes Velocity Contour) - Multi-Channels

51

Figure 3.27: Diffuser Outlet (2,392,054 Nodes Velocity Contour) - Multi-Channels
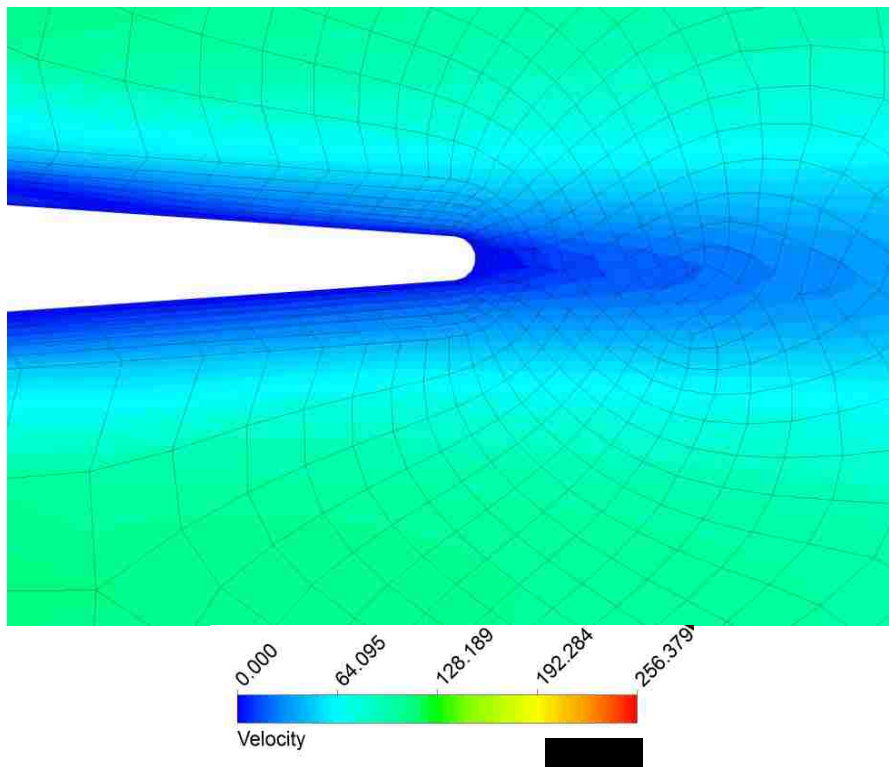
Figure 3.28: Diffuser Outlet (2,392,054 Nodes Velocity Contour) - Close Up

52

Three different meshes are evaluated in this study. Orthogonal quality and skewness are also used to monitor the quality of each mesh. Dynamic pressure at the inlet, mass flow rate at the outlet, and maximum inlet velocity are compared between different meshes. Mesh convergence and independence can be determined from the comparison. Table 3.3 shows the comparison below:

Table 3.3: Multi-Channels Mesh Matrix (3 Degree Diffuser)

Turbulence Model	# of Nodes	# of Elements	Orthogonal Quality	Skewness	Dynamic Pressure (Psi)	Max Inlet Velocity (m/s)	Mass Flow Rate (g/s)
SKW	1,594,242	1,400,256	0.978	6.42E-02	0.81	57.47	4.01
SKW	2,392,054	2,139,007	0.972	7.89E-02	0.79	56.97	3.97
SKW	3,276,750	2,945,782	0.977	6.43E-02	0.79	56.99	3.98
SSTKW	1,594,242	1,400,256	0.978	6.42E-02	1.86	73.52	4.95
SSTKW	2,392,054	2,139,007	0.972	7.89E-02	1.85	72.00	5.02
SSTKW	3,276,750	2,945,782	0.977	6.43E-02	1.85	71.62	5.02

In Table 3.3, three criteria monitored during the calculation shows little to no difference. To ensure mesh convergence and independence are reached, the entire range of scaled residuals and dynamic pressure data were monitored during the calculation. A demonstration is shown below by using the SSTKW model:
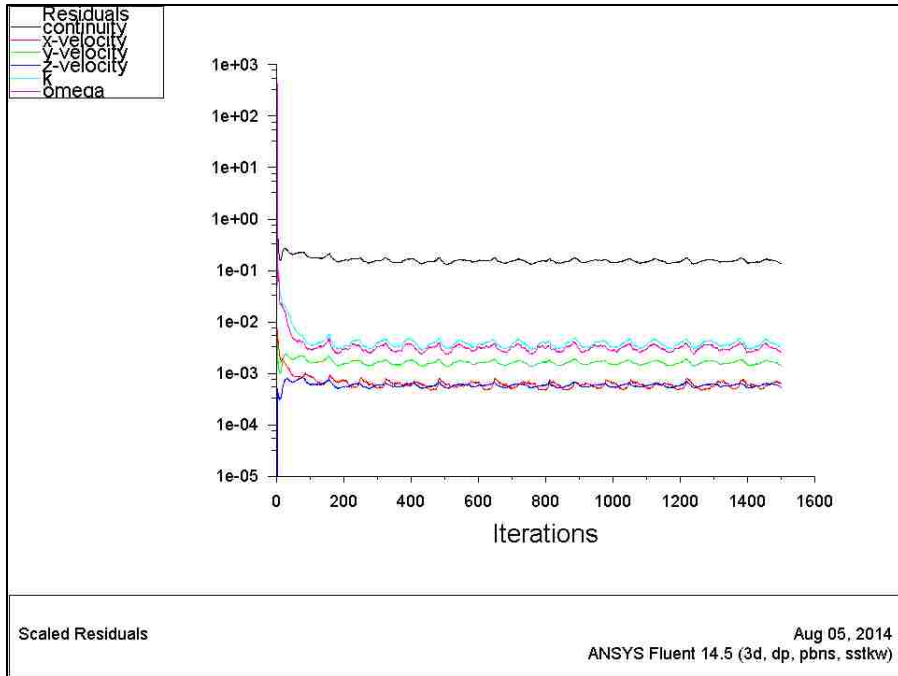
Figure 3.29: Scaled Residuals – Multi-Channels (1,594,242 nodes) SSTKW
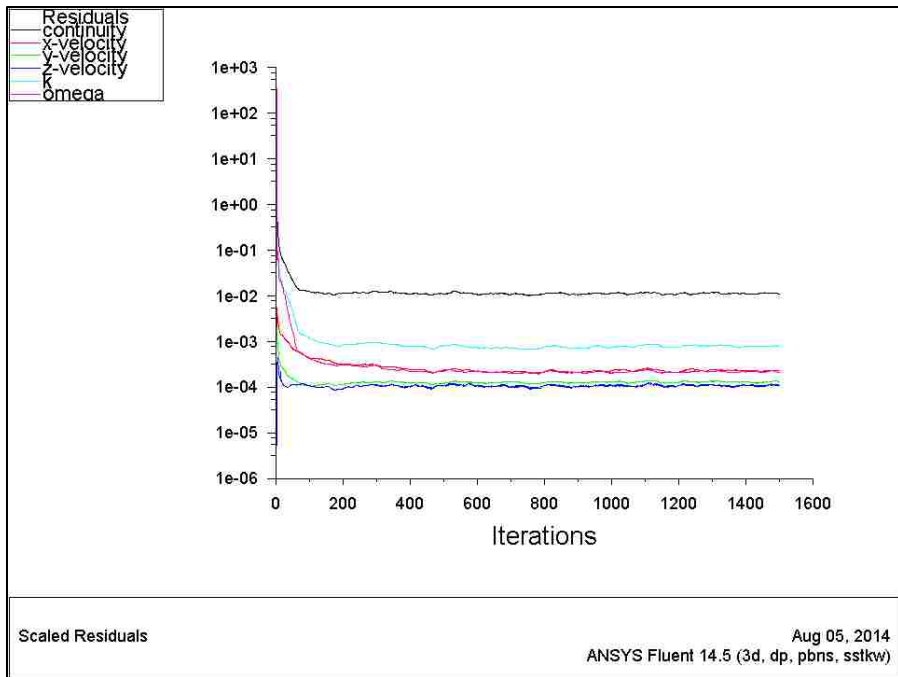
Figure 3.30: Scaled Residuals – Multi-Channels (2,392,054 nodes) SSTKW
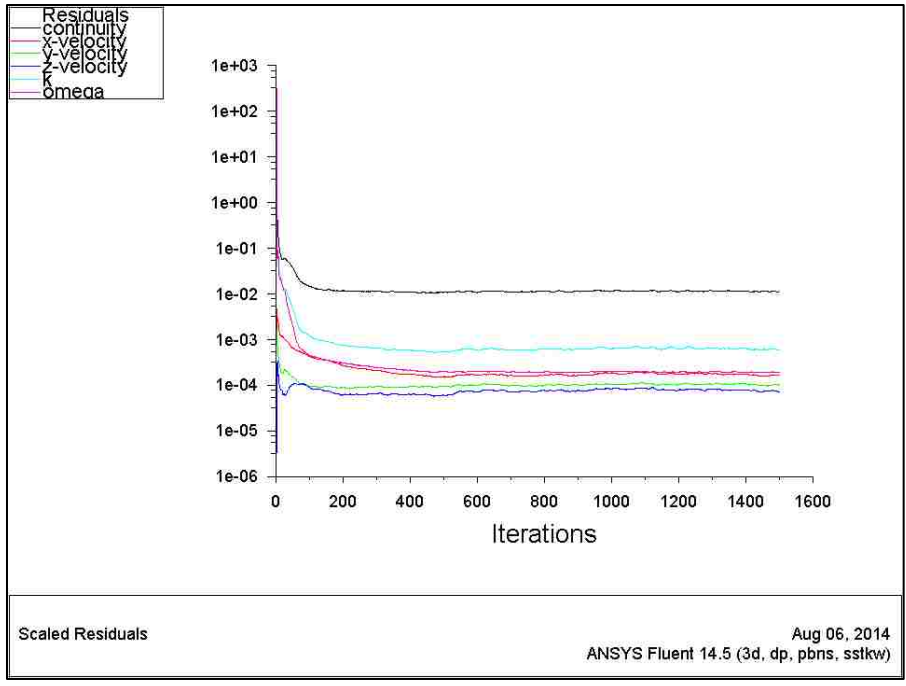
Figure 3.31: Scaled Residuals - Multi-Channels (3,276,750 nodes) SSTKW

All residuals for 1,594,242 nodes mesh (Figure 3.29) are higher than rest of the mesh setups. High oscillations are also shown on all residuals in Figure 3.29.
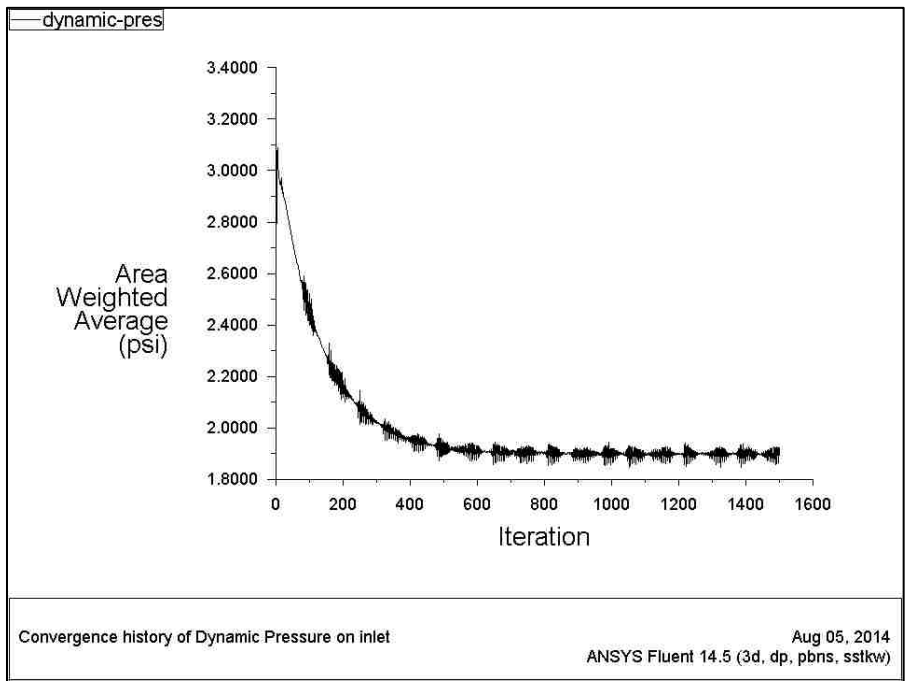
Figure 3.32: Inlet Dynamic Pressure - Multi-Channels (1,594,242 nodes) SSTKW

55
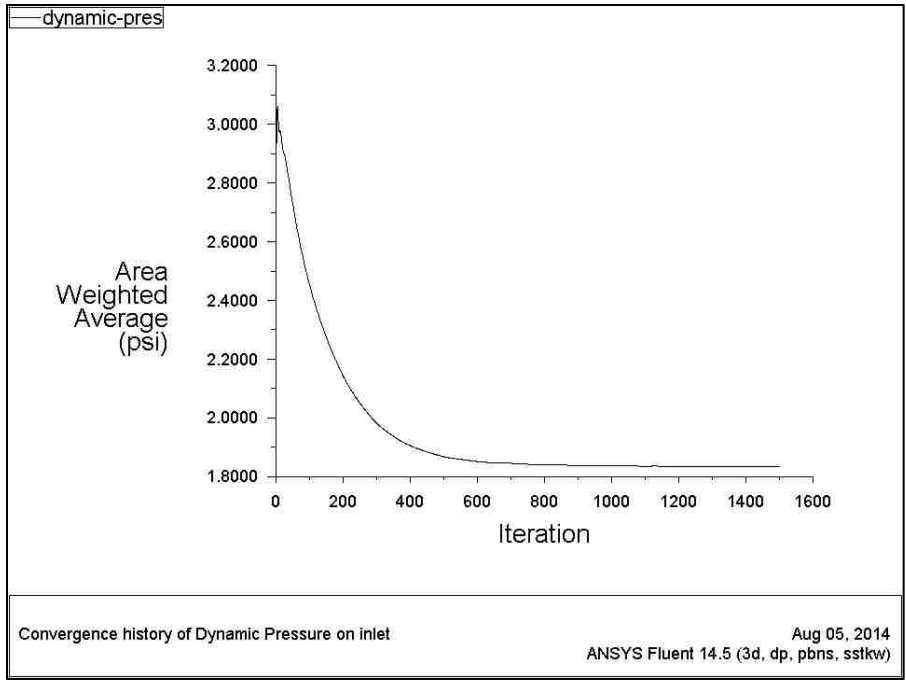
Figure 3.33: Inlet Dynamic Pressure - Multi-Channels (2,392,054 nodes) SSTKW
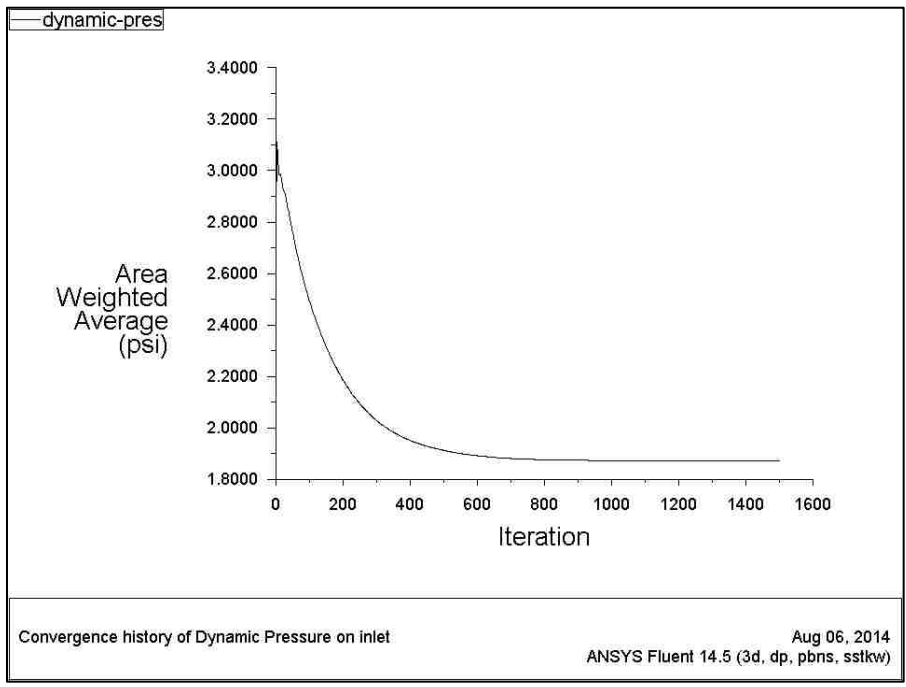
Figure 3.34: Inlet Dynamic Pressure - Multi-Channels (3,276,750 nodes) SSTKW

As the solution reaches steady state, dynamic pressure at the inlet section should stay constant. Evidence in Figure 3.32 shows that, the solution has not reached steady state yet with 1,594,242 nodes mesh setup. A mesh refinement is required to improve the quality of the solution.

From the two comparisons, 2,392,054 nodes and 3,276,750 nodes mesh setups show the same behaviors between each other, therefore, 2,392,054 nodes mesh becomes the best choice for this particular study. It shows that mesh convergence and independence are reached with 2,392,054 nodes setup. Same procedures shown above are applied to all other cases conducted in this project. Figure 3.35 shows a typical velocity contour plot for 2,392,054 nodes mesh
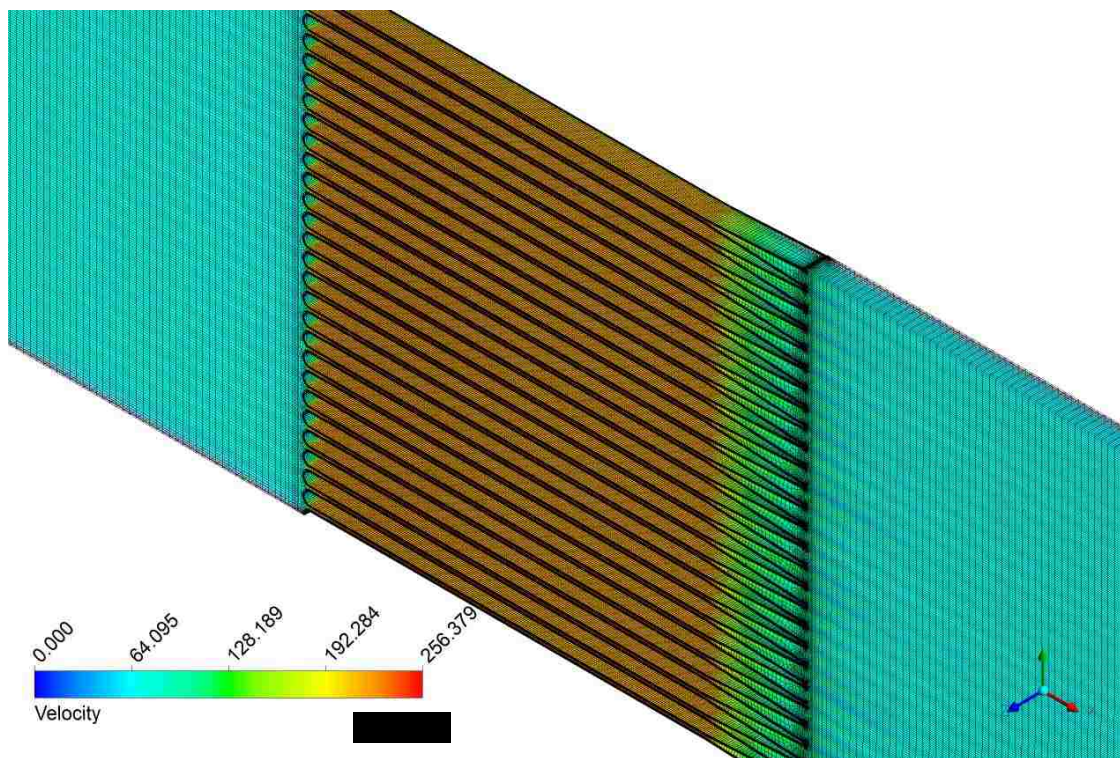
Figure 3.35: 2,392,054 Nodes Mesh - Velocity Contour

Chapter 4 – Design Decision and Model Reduction

In this chapter a series of CFD results for both single channel model and multi-channels model are documented. As mentioned in previous chapter, inlet feature will be determined in this chapter. Two potential candidates were proposed for this project: quarter circle and 45° angled inlet. A side by side comparison along with base case design (sudden contraction and expansion) will be shown in this chapter. A final decision will be made in this chapter for the inlet feature.

The number one goal for this project is to maximize the flow rate to reduce extra heat created by the system process. In addition to the inlet feature, a diffuser outlet is added to the system to help guide the flow out of cooling section. A series of diffuser angles are tested in later section of this chapter. A design will be finalized at the end of this chapter. To validate the CFD models developed for this project; results gathered from this chapter will be compared against a series of in-house experimental data. The comparisons with the data will be shown in the next chapter.

4.1 Inlet Feature Selection

As mentioned earlier, two features were proposed for the inlet section: quarter circle and 45° angled inlet. A visual representative for both features can be found in Figure 4.1 and Figure 4.2. Both geometries feature a sudden expansion outlet, this outlet can be found in Figure 4.3.

Figure 4.1: Quarter Circle Inlet
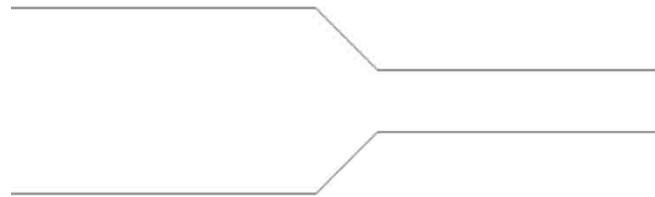
Figure 4.2: 45° Angled Inlet
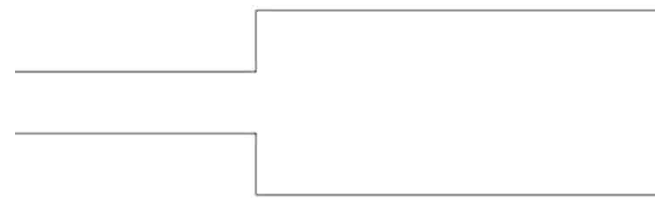
Figure 4.3: Sudden Expansion Outlet

Both geometries are supplied with 300 Psi pressure at the inlet and configured to have 15 Psi pressure drop across the channel. A pressure based and time steady solver is used for both geometries. The results from both cases will be directly compared to the base case shown in Figure 3.4

Figure 4.4 and Figure 4.5 show the results for the steady state solution for both quarter circle inlet and 45° angled inlet, respectively. From the visual comparison, quarter circle inlet has a better performance in velocity than the 45° angled inlet. However, only looking at the maximum velocity does not tell the whole story, more details need to be investigated to make the final conclusion.
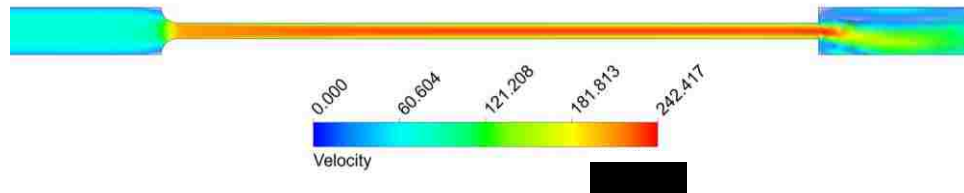
Figure 4.4: Steady State Velocity Contour for Quarter Circle Inlet - SSTKW
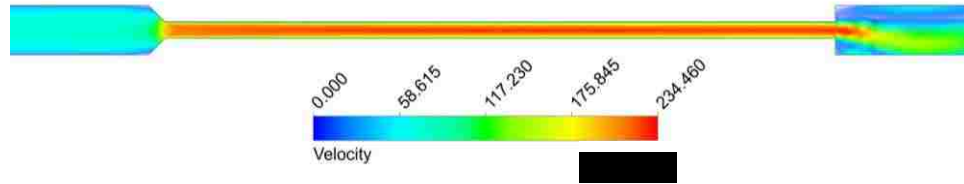
Figure 4.5: Steady State Velocity Contour for 45 Degree Angled Inlet - SSTKW

When only focusing on the inlet section, things are becoming a lot clearer than looking at the whole picture. Use base case shown in Figure 4.6 as an example, as explained earlier in section 3.2 when fluid flow through a sudden contraction region the majority of the loss is due to the inertia effects.
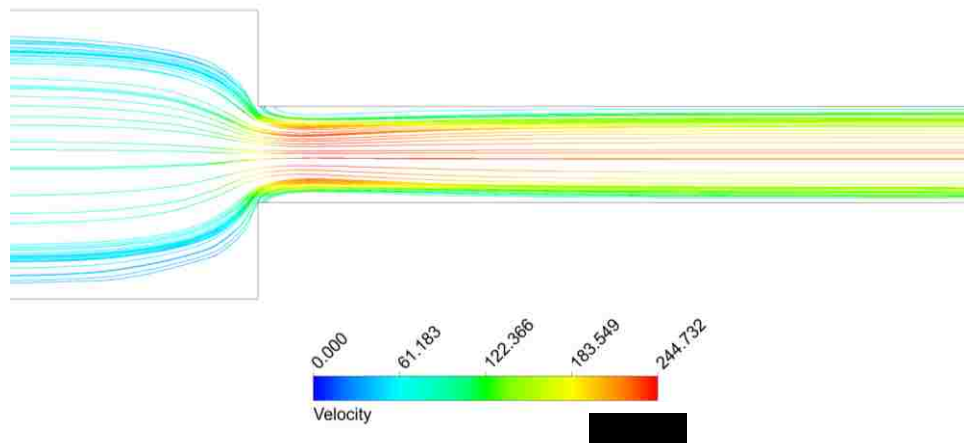
Figure 4.6: Steady State Velocity Streamline for Sudden Contraction Inlet - SSTKW

Evidence shown in Figure 4.6, due to the sudden contraction entrance effect, most of the energy is lost right around the entrance area. A high velocity flow is concentrated

60

around one spot (right after entrance) and slowly dissipated downstream. The velocity intensity downstream is becoming weaker and weaker; therefore the cooling ability for the entire cooling channel becomes not so efficient.
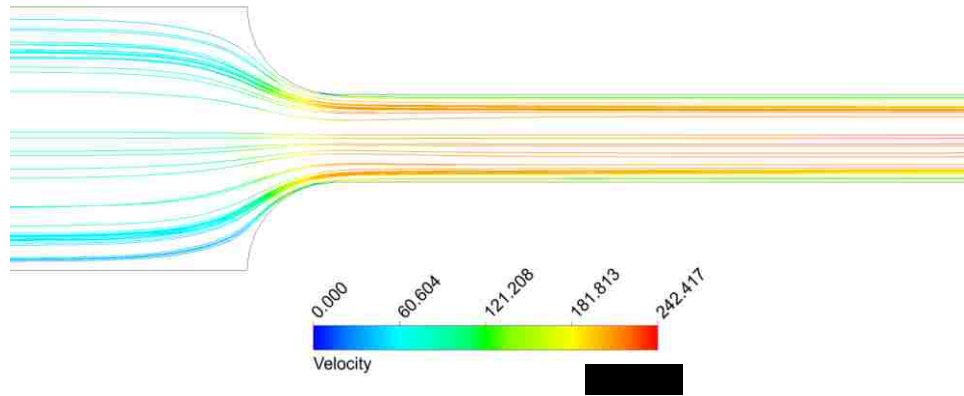
Figure 4.7: Steady State Velocity Streamline for Quarter Circle Inlet - SSTKW
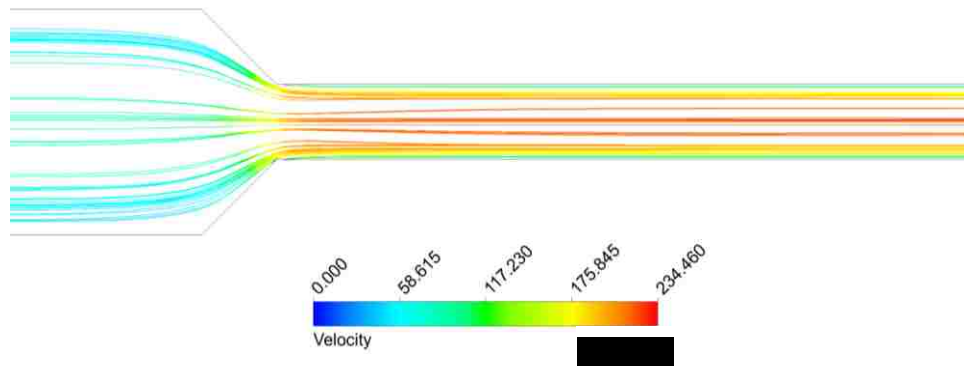
Figure 4.8: Steady State Velocity Streamline for 45 Degree Angled Inlet - SSTKW

On the other hand, in Figure 4.7 and Figure 4.8 show better velocity distributions through the entire cooling channels by using either quarter circle inlet or 45° angled inlet. When comparing quarter circle inlet to 45° angled inlet, quarter circle inlet tended to have a better flow distribution than the 45° angled inlet. The fully rounded walls from the quarter circle inlet guided the flow smoothly through the entrance. The sharp edges on

the 45° angled inlet added a little disturbance to the flow, which resulted in uneven distribution of the flow.

Detailed comparisons between all geometries are provided in both Table 4.1 and Table 4.2. From the results, both models have shown a sign that quarter circle inlet and 45° angled inlet have significant improvement on the flow performance when compare to the base case design (sudden contraction and expansion). Fortunately, a decision can be made based on the results shown in Table 4.1 and Table 4.2. Both models agree that the quarter circle inlet design is the best candidate for this project. The quarter circle design has outperformed 45° angled inlet design in every single category that has been compared. The data indicates that the quarter circle inlet design causes a lower degree of resistance in the flow, and provides a high efficiency in temperature cooling.

In addition, quarter circle geometry is easier to fabricate when using wire Electrical Discharge Machining (EDM) technology, therefore reducing the manufacturing costs. With all of these reasons, quarter circle inlet design is chosen for the remaining simulation.

Table 4.1: Inlet Geometries Performance Comparison (Single Channel SKW Model)

	Mass Flow Rate (g/s)	Max Inlet Velocity (m/s)	Max Mid-Channel Velocity (m/s)	Average Mid-Channel Velocity (m/s)	Mass Flow Improvement
Sudden Contraction Inlet	1.46	57.4	197.5	143.5	--
Quarter Circle Inlet	1.64	66.1	223.0	164.3	12.3%
45° angled inlet	1.60	63.4	213.7	157.9	9.59%

Table 4.2: Inlet Geometries Performance Comparison (Single Channel SSTKW Model)

	Mass Flow Rate (g/s)	Max Inlet Velocity (m/s)	Max Mid-Channel Velocity (m/s)	Average Mid-Channel Velocity (m/s)	Mass Flow Improvement
Sudden Contraction Inlet	1.55	60.8	220.9	145.7	--
Quarter Circle Inlet	1.74	68.1	237.0	164.8	12.3%
45° angled inlet	1.69	66.1	231.3	158.3	9.03%

4.2 Single Channel Diffuser Angle Selection

Diffuser is commonly used in many applications, for instance, the tail end of a F1 racecar, an impeller inside the centrifugal pump, and more commonly the cooling channels inside a heat exchange device.

The second feature that is added to the new design is a diffuser. An optimal diffuser angle, commonly known as the "sweet spot" for many of computational fluid analysts can be determined through a series of parametric studies. An optimal angle indicates that the separation of the flow is minimized and the speed of the flow is maximized. As mentioned earlier, according to Lan's [20] study, the recirculation flow region does not develop in diffuser (half) angles equal to, or less than 6.5 degrees. However, a slightly different correlation was found compared to the one that Lan had claimed. The different correlation is mainly due to the difference in boundary conditions and overall geometry.

Stated in many literatures, by reducing the angle of the diffuser to follow the natural flow patterns, the amount of separation will be limited. Many studies started with diffuser half angle of 10 degree. For this project, 10 through 3 degree diffuser angles along with 1 degree decrement in between were tested. As the decision made from

section 4.1, all geometries are using the quarter circle inlet. With no change to the operating condition, 15 Psi pressure drop was enforced along with 300 Psi inlet pressure. Both Figure 4.9 and Figure 4.10 show the computed streamlines for 8 different diffusers angles. Instead of finding 6.5-degree diffuser angle to be the critical diffuser angle, which differentiates the recirculation region, both models agree that 5-degree diffuser angle is the transitional angle for this project.
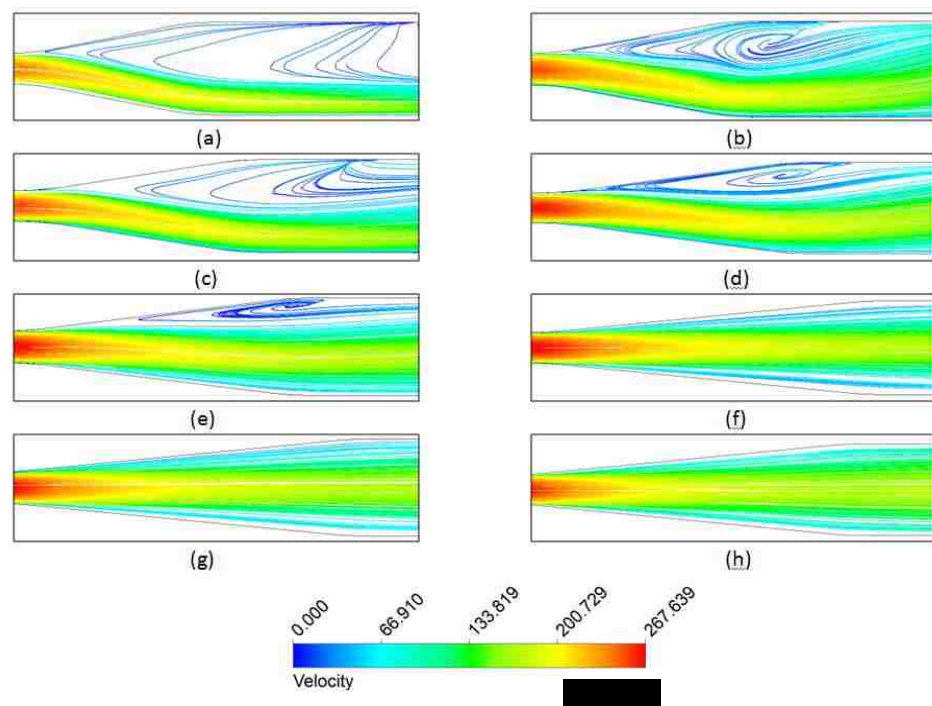
Figure 4.9: SKW Model - Streamline Paths and Velocity Magnitude with Different Diffuser Angles: (a) $\alpha = 10°$,(b) $\alpha = 9°$, (c) $\alpha = 8°$, (d) $\alpha = 7°$, (e) $\alpha = 6°$, (f) $\alpha = 5°$, (g) $\alpha = 4°$, and (h) $\alpha = 3°$
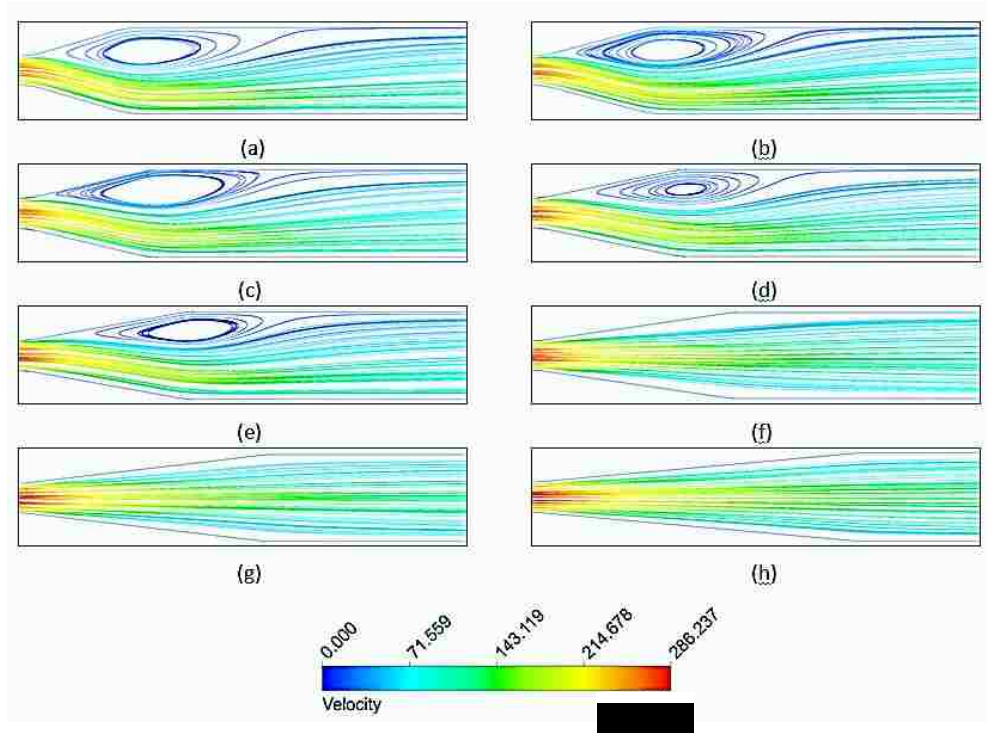
Figure 4.10: SSTKW Model Streamline Paths and Velocity Magnitude with Different Diffuser Angles: (a) $\alpha = 10°$,(b) $\alpha = 9°$, (c) $\alpha = 8°$, (d) $\alpha = 7°$, (e) $\alpha = 6°$, (f) $\alpha = 5°$, (g) $\alpha = 4°$, and (h) $\alpha = 3°$

Table 4.3: Parametric Study: Single Channel

Turbulence Model	Angle (Degree)	Mass Flow (g/s)	Max Channel Velocity (m/s)	Max Inlet Velocity (m/s)	Max Mid-Channel Velocity (m/s)	Average Mid-Channel Velocity (m/s)
SKW	10	1.67	258.5	69.1	237.0	177.2
SKW	9	1.68	261.7	69.3	238.0	178.8
SKW	8	1.71	261.4	69.3	239.1	178.9
SKW	7	1.73	263.1	69.4	239.3	179.6
SKW	6	1.75	265.1	69.4	240.2	179.6
SKW	5	1.79	267.2	69.5	240.5	180.1
SKW	4	1.79	267.6	70.1	242.2	181.7
SKW	3	1.77	266.3	69.7	241.5	180.7
SSTKW	10	1.94	269.3	75.82	268.5	193.4
SSTKW	9	1.94	270.5	76.18	269.7	194.3

Turbulence Model	Angle (Degree)	Mass Flow (g/s)	Max Channel Velocity (m/s)	Max Inlet Velocity (m/s)	Max Mid-Channel Velocity (m/s)	Average Mid-Channel Velocity (m/s)
SSTKW	8	1.98	275.1	77.56	274.4	198.0
SSTKW	7	2.00	278.2	78.42	277.4	200.4
SSTKW	6	2.02	282.0	79.43	281.0	203.1
SSTKW	5	2.06	287.1	80.76	285.8	206.6
SSTKW	4	2.06	287.5	80.56	286.0	206.1
SSTKW	3	2.05	285.7	80.11	284.2	204.9

The results from a parametric study for the single channel model are shown in Table 4.3. The key design factor of mass flow rate was closely monitored. According to Table 4.3, both models agree that channel mass flow reaches its peak performance when the geometry of the diffuser (half) angle is tuned in between 4 and 5 degrees. The results from this table are also corresponded to the outcome shown earlier in Figure 4.10. When transitional angle 5 degree is reached the maximum mass flow rate can be obtained. Both results prove the theory when reducing the diffuser angle to a certain degree, the amount of separation can be limited and, therefore the peak flow performance can be reached.

The trend of mass flow performance versus diffuser angle is shown in Figure 4.11 below. The graph below shows the diffuser geometry is very sensitive for both models; it directly affects the flow performance of the cooling channel. When the diffuser angle is less or greater than the critical angles, the flow performance of the channel starts to decrease.
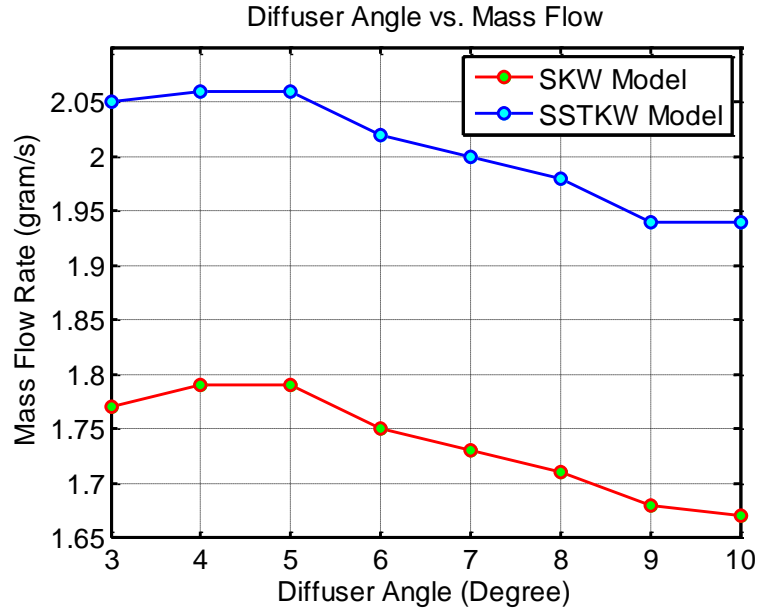
Figure 4.11: Diffuser Angle vs. Mass Flow

The comparison of performances between different diffuser angles can be constructed in terms of percentage of improvement. In Table 4.4 shows the percentage of the mass flow improvement for each case compares to the base case with sudden contraction inlet and sudden expansion outlet.

Note: all diffusers are featuring with quarter circle inlet.

Table 4.4: Mass Flow Improvement for Different Diffusers

Angle (Degree)	Mass Flow Improvement (SKW)	Mass Flow Improvement (SSTKW)
Sudden Contraction and Expansion	--	--
10	14.4%	25.2%
9	15.1%	25.2%
8	17.1%	27.7%
7	18.5%	29.0%
6	19.9%	30.3%
5	22.6%	32.9%
4	22.6%	32.9%
3	21.1%	32.3%

From all of the comparisons shown in this section, SSTKW model produced higher value in every category than the SKW model. However, the behaviors of these two models are very similar. Both models indicated that quarter circle inlet adds more mass flow performance than the 45° angled inlet, and they both agreed that the transitional angle for the diffuser is around 5 degree. The final decision of which turbulence model to use for this project will heavily rely on the experimental data that was gathered at LANL.

4.3 Multi-Channels Study

Evidence from a series of single channel studies has shown that adding a quarter circle inlet and diffuser outlet improved the mass flow performance in the channel, which directly improves the heat transfer rate of the cooling channel. Study from section 4.2 has shown that 4 and 5 degree diffuser (half) angle are the critical angles, which allow maximum mass flow rate to be reached. From all of this evidence, many of the testing matrices can be reduced. For instance, for multi-channels study, instead of testing diffuser (half) angle from 3 to 10 degree, the test was reduced down to 3 to 6 degree. By doing this process, both computational and experimental expense are reduced by at least half. In another word, single channel study has helped save both time and money for this project.

4.3.1 Model Reduction for Multi-Channels Study

Even though the single channel study has helped reduced the testing parameters by half, modeling the multi-channels model is still computationally intensive. A 27 channels model was constructed to match the experiment that was conducted at LANL.

By using multi-channels model with quarter circle inlet and 4 degree diffuser outlet as an example, to maintain a high quality mesh for selected model an extremely high value of nodes is required. The mesh matrix for this particular model is shown in Table 4.5.

With 8 cores processors running on their full speed and 24 GB of physical memory available for the system, it took almost 72 hours (2,000 iterations) to allow the model to reach a convergent solution. In addition to the calculation time, an hour of mesh development time was required before starting the simulation. Figure 4.12 shows a typical mesh used for the full model.

Table 4.5: Full Model Mesh Matrix

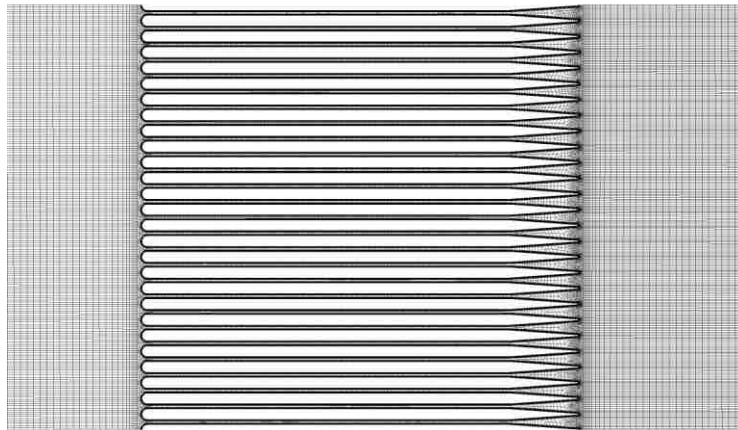| # of Nodes	# of Elements	Orthogonal Quality	Skewness
13,680,880	12,820,992	0.964	0.110

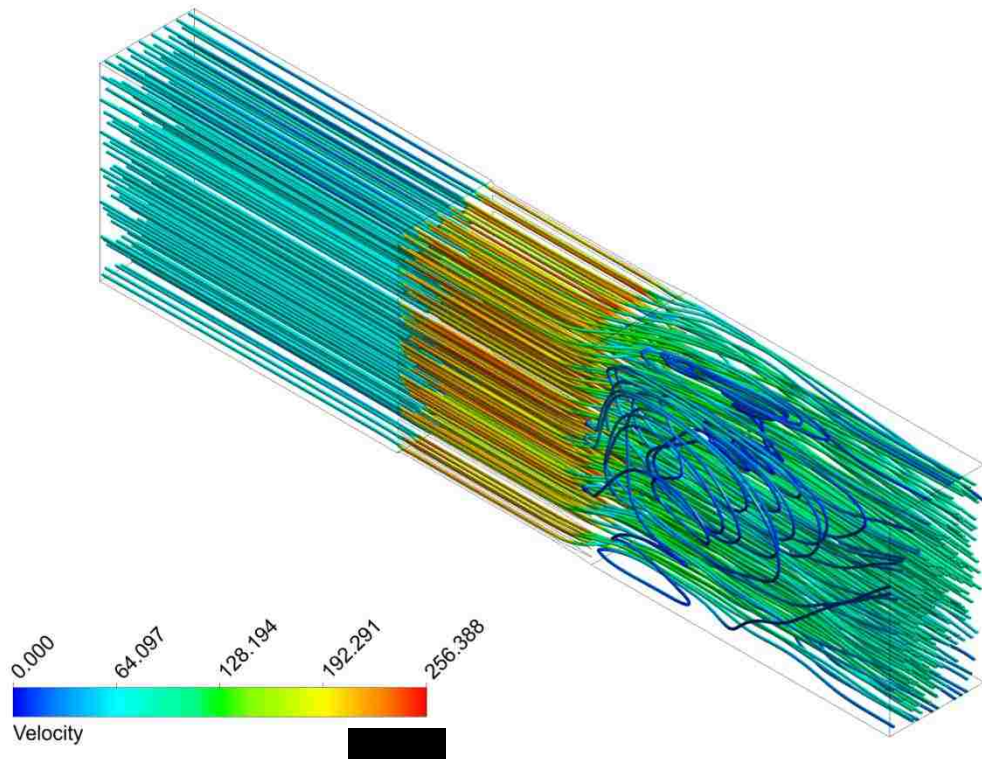Figure 4.12: Full Model Mesh (27 Channels with 4 Degree Diffuser)

Figure 4.13: Full Model Velocity Streamline (27 Channels with 4 Degree Diffuser – SSTKW Model)

The computational cost has become very expensive in this case; the goal for this project is keep the simulation simple but accurate, it is not a good practice for this project to require days of simulation. In addition to the calculation time, post processing the result has become extremely difficult. It requires a tremendous amount of memory to process the data. To conquer all of these computational issues and reduce the cost of computing, a new method of modeling technique was proposed. Instead of modeling the entire domain a 1/10 model was used. As mentioned before, in addition to the 1/10 model, symmetry boundary condition was used to simulate the behavior of the full domain. A typical 1/10 model can be found in Figure 4.14.
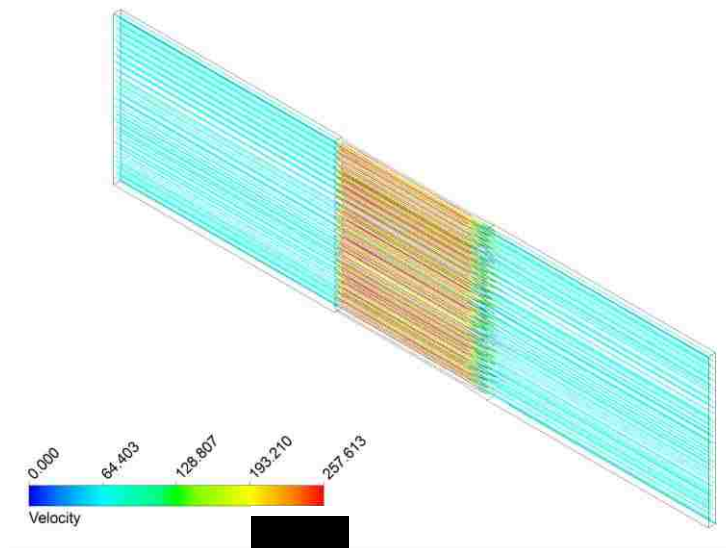
Figure 4.14: 1/10 Model Velocity Streamline (27 Channels with 4 Degree Diffuser – SSTKW Model)

When the size of the model is reduced the size of the mesh is also decreased. A new mesh matrix for the reduced model can be found in Table 4.6.

Table 4.6: 1/10 Model Mesh Matrix

# of Nodes	# of Elements	Orthogonal Quality	Skewness
2,677,168	2,419,830	0.972	7.91E-02

Comparing the data from Table 4.5 and Table 4.6, 80% of mesh size reduction has been shown in the 1/10 model while maintaining the quality of the mesh. The benefit of this reduced model is significant. With the same computing power, the total meshing time is reduced from an hour to 20 minutes, and most importantly, the overall solving time to obtain a converged solution is reduced from 72 hours to 3 hours. A 96% reduction in solving time is a big savings for this project; instead of waiting for the result in days many other analyses can be performed and many cases can be processed during a short

71

period of time. Typical convergence results for the reduced model in both SKW and SSTKW model can be found as follows:
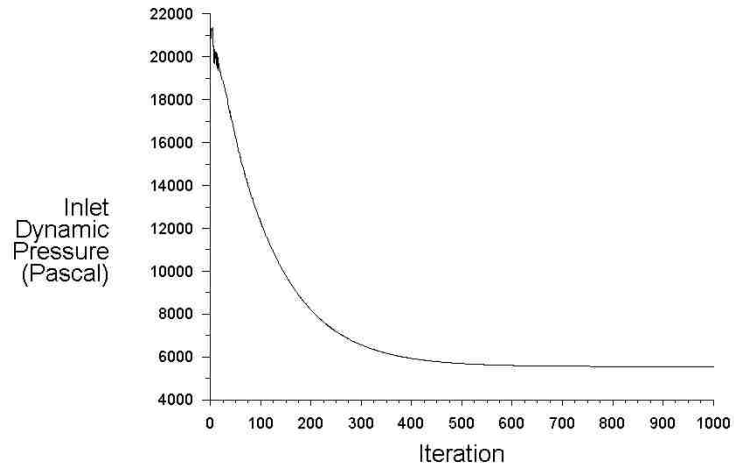
Figure 4.15: 1/10 Model Convergence History - Inlet Dynamic Pressure (SKW)
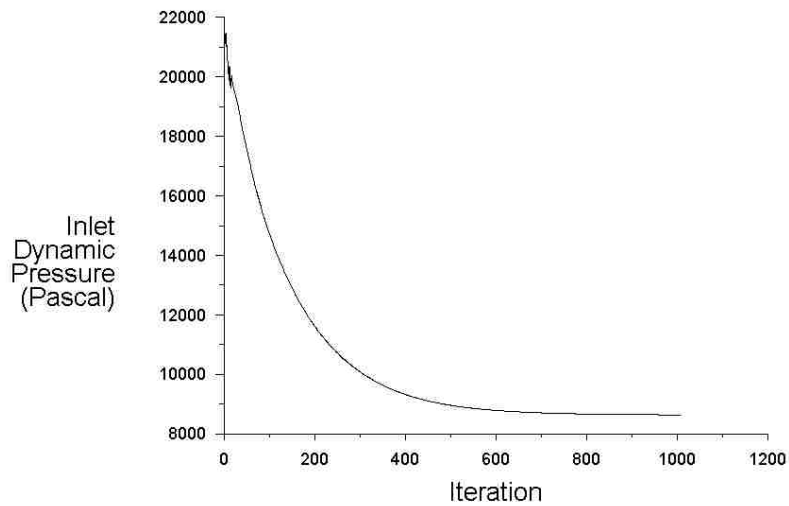
Figure 4.16: 1/10 Model Convergence History - Inlet Dynamic Pressure (SSTKW)
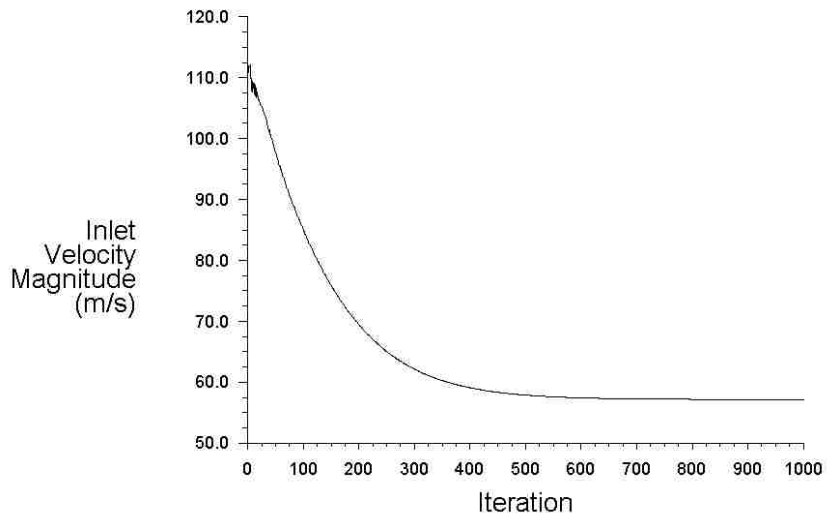
Figure 4.17: 1/10 Model Convergence History - Inlet Velocity Magnitude (SKW)
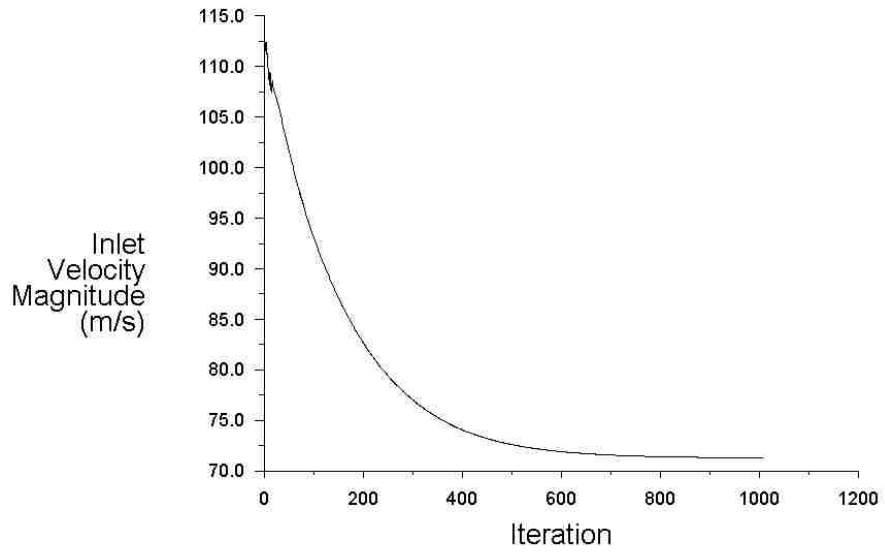
Figure 4.18: 1/10 Model Convergence History - Inlet Velocity Magnitude (SSTKW)
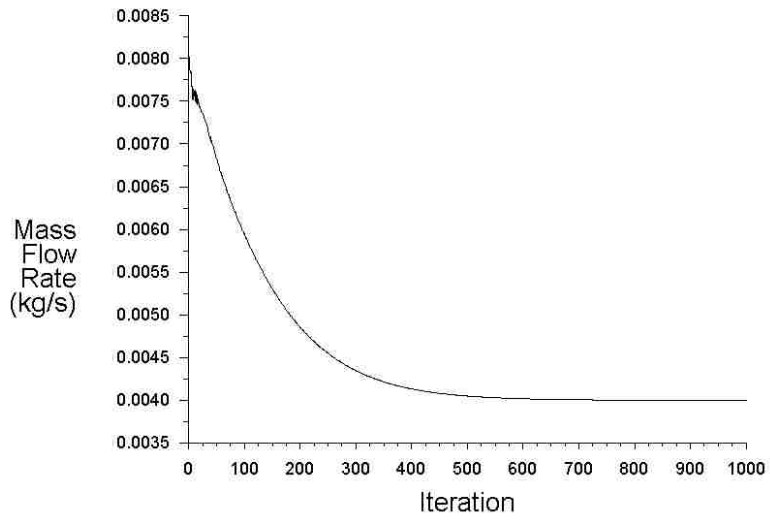
73

Figure 4.19: 1/10 Model Convergence History - Inlet Mass Flow Rate (SKW)
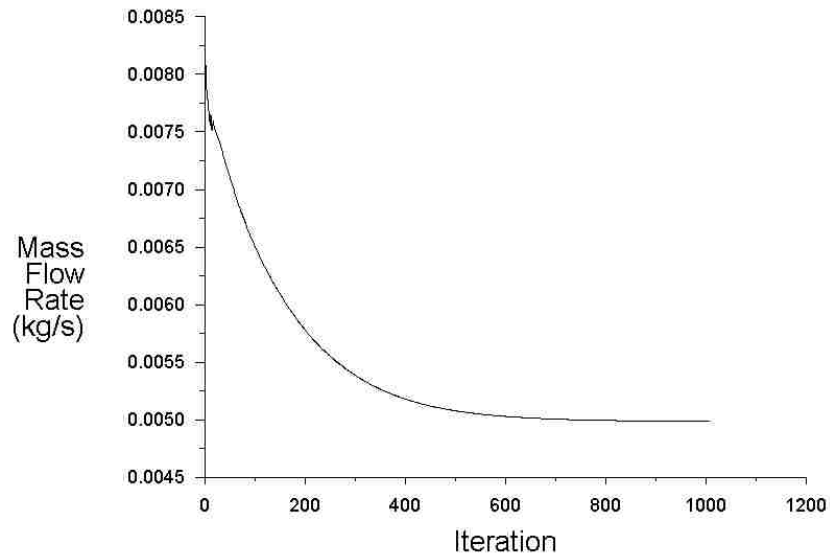
Figure 4.20: 1/10 Model Convergence History - Inlet Mass Flow Rate (SSTKW)

From the convergence results shown above, with the 1/10 model, both turbulence models can provide a stable solution in a short period of time. As expected from the previous study. The SSTKW model will always produce a higher value in every catogories that have been compared than the SKW model in every case that has been compared. The decision on the choice of the turbulence model will depend on how well the model matches the experimental data. Both turbulence models will be compared directly to the experimental data collected at LANL in the next chapter. A final decision on the turbuence model will be made based on the accuracy of the model for this project.

Chapter 5 – Validation Analysis

The aim of this chapter is to perform the V&V analysis to make sure about this CFD analysis. The criteria of V&V have perspective on the base of ASME and AIAA standard codes. Verification is the process of assessing software correctness and also the numerical accuracy of the solution for a mathematical model and Validation is defined as the process of evaluation of the physical accuracy of a mathematical model based on comparisons between the computational results and the experimental data. [22] To assess validation an experimental analysis was performed as mentioned earlier, an in-house experiment at LANL. Based on the early CFD result, many of the design parameters were finalized. A quarter circle inlet and diffuser outlet were decided for this project. Adding both features to the existing design has significantly improved the mass flow rate in the target cooling channels, which will directly increase the heat transfer ability of the system. From the single channel study, a decision was made to reduce the test parameters to half and only test the diffuser angle near the critical angle (3 to 6 degree half angle). With all of these decisions, 6 prototypes were computer drafted and machined, and they are: sudden contraction and expansion, quarter circle inlet and sudden expansion outlet, and 4 of quarter circle inlet featured with 3 to 6 degree (half angle) diffuser outlet.

5.1 Experiment Setup

Because of the space constraint for the existing test bench at LANL only 27 channels were able to fit in the test section. This is the main reason why only 27 channels were modeled instead of the entire 82 channels. A typical drawing for the prototype can

be found in Figure 5.1. Following the drawing, an actual prototype is shown in both Figure 5.2 and Figure 5.3.
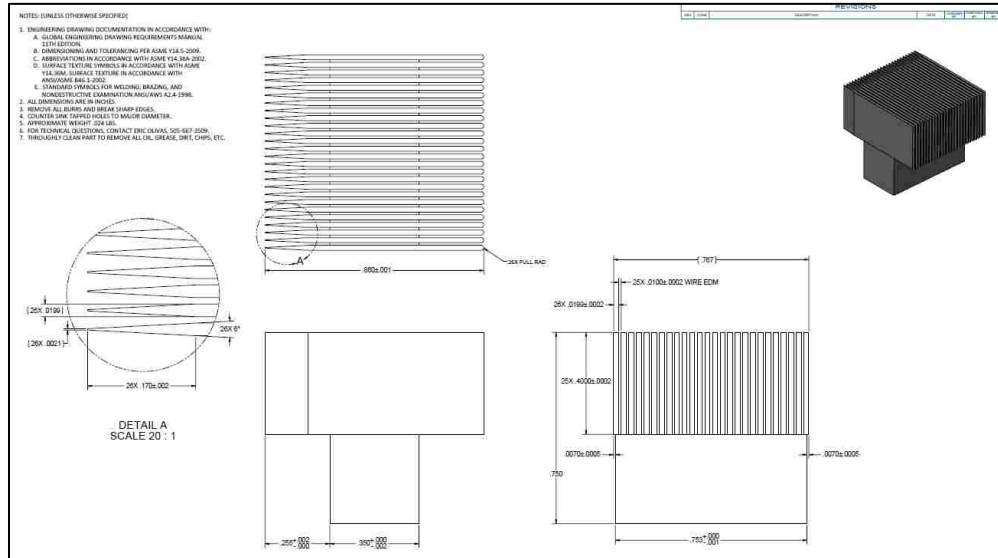
Figure 5.1: A Typical Design Drawing for Mo99 Project
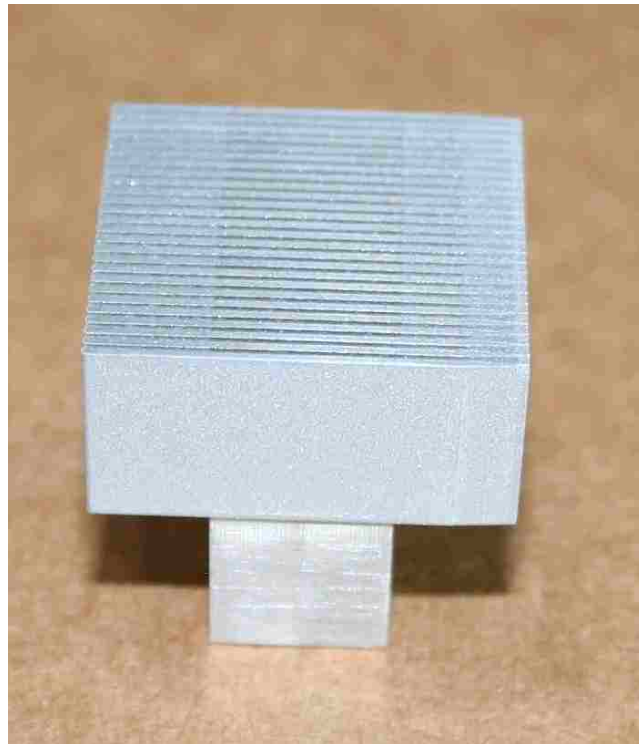
Figure 5.2: Mo99 Target Prototype Front
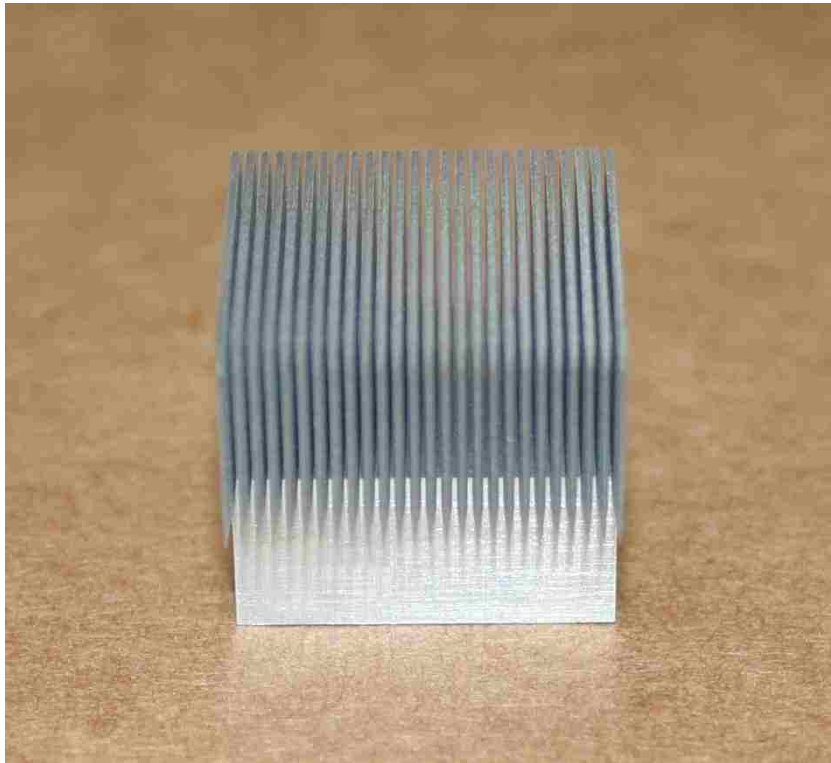
Figure 5.3: Mo99 Target Prototype Side View

As explained earlier in Chapter 1, section 3, the driving force for the closed loop helium gas cooling system is a root blower. During the experiment, the blower pushed helium gas through the test section and a series data were collected from the test section. A picture shows in Figure 5.4 gives a little detail about the test section.
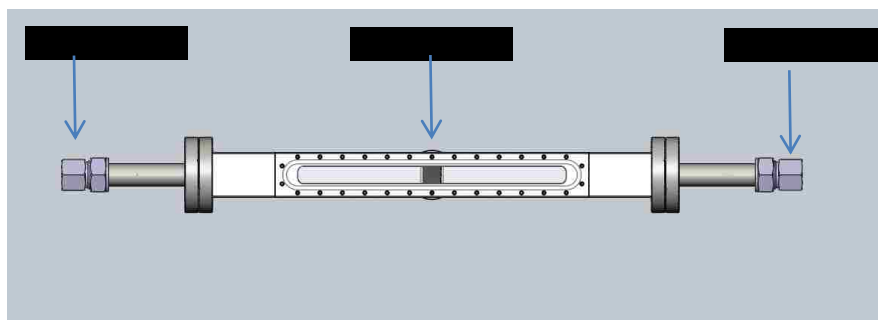
Figure 5.4: Solidworks Model for Test Section

Pressure drop and mass flow rate were measured in the experiment model as validation metrics. To properly record the data needed from this experiment, many of measuring instruments were used. Two of the most important instruments are flow meter and pressure gauge. A Flow meter was placed upstream of the test section to monitor flow before entering into the target cooling channels. Three pressure gauges were used in this experiment to monitor the pressure across the target cooling channels. The actual placement of the instruments used in this experiment can be found in Figure 5.5 and Figure 5.6.
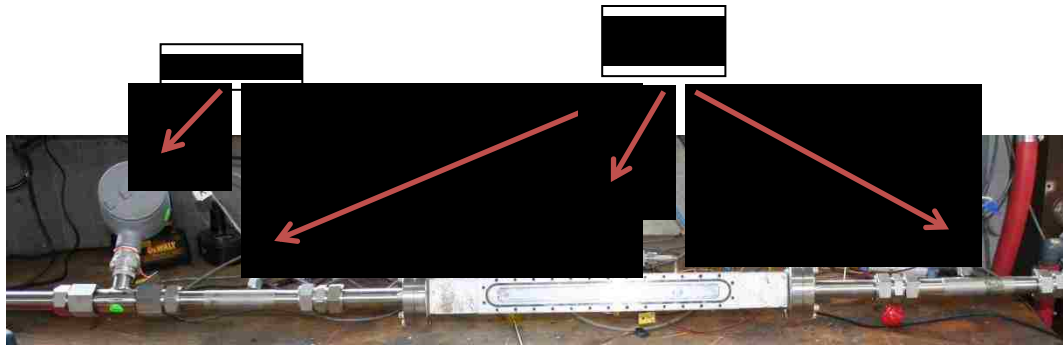
Figure 5.5: Experiment Instruments Setup
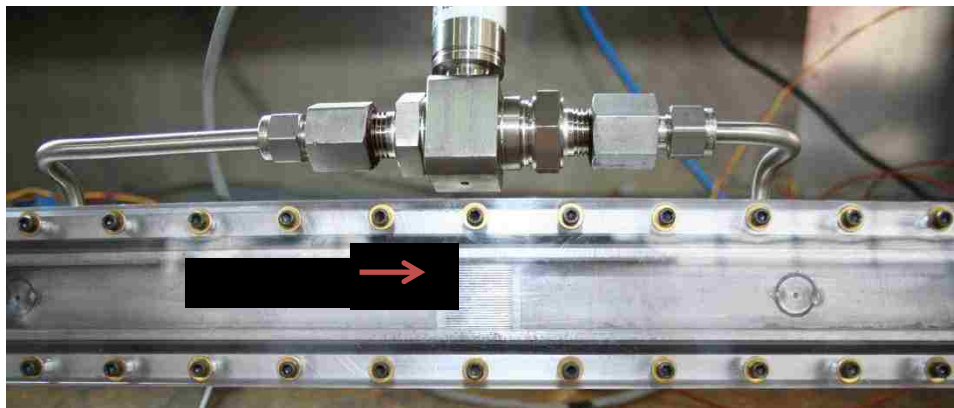
Figure 5.6: Experiment Target Placement

79

5.2 Experimental Incident

Like many other experiments, something unexpected happened during this experiment. An incident occurred when 6 degree diffuser geometry was tested inside of the test section; it was the very first one to be tested. A structure failure occurred when high pressure drop (much greater than15 Psi) was introduced to the target cooling channels. One of the disks completely separated from the holder and ended up inside of the flowing loop and two additional ones were collapsed to their neighboring disk. Luckily, all of the valuable data were taken before this incident happened. Evidence from this incident can be found in the figures below:
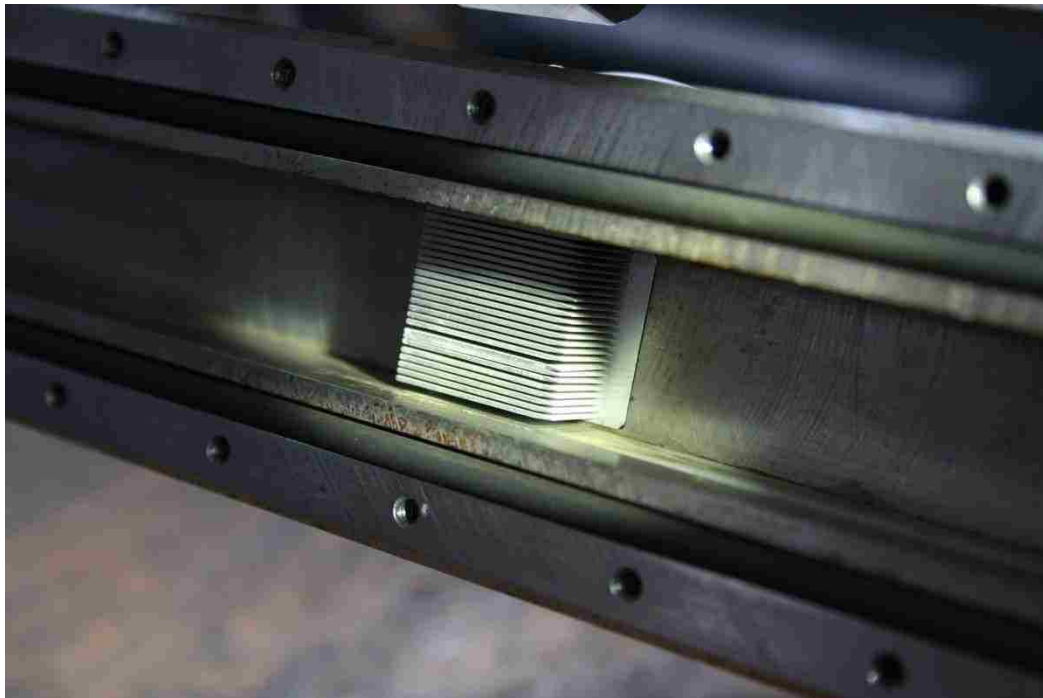
Figure 5.7: Experiment Incident - Two Collapsed Disks

Figure 5.8: Experiment Incidence – Broken Disks

Since this incident occurred, all other geometries were tested with extreme care. Pressure drop across the target cooling channels was monitored closely to make sure that no extreme pressure drop is introduced to the system. Fortunately, with the new test plan, this incident did not occur for the rest of the test geometries. The incident also indicates that there is still room for the test piece to be improved, especially on the structure rigidly side.

5.3 Experimental Result

Many of the design features can be validated in this section, two main results are processed from this experiment: mass flow rate as a function of pressure drop and average mass flow rate at the system required operating condition (15 psi pressure drop across the channels).

The pressure drop across the system is caused by the shape of the target cooling channels traversed by the flow and by the driving pressure at the inlet of the channels. As discussed before, pressure drop has a direct relationship between entrance and exit losses. A decision was made in Chapter 4 that to help reduce the loss at entrance and exit, a quarter circle inlet and diffuser outlet were added. This part of study focused on how a change in pressure drop changes the mass flow rate of the system.

To achieve different pressure drop values across the channels, a control unit was used to control the speed of the motor (in Hertz) to vary the torque of the blower. A 5 Hz increment was used to separate different pressure drops. From the experiment, the following pressure drops were closely monitored: 2 psi, 5 psi, 10 psi, and 15 psi. A comparison from the experiment data is provided in Figure 5.9.
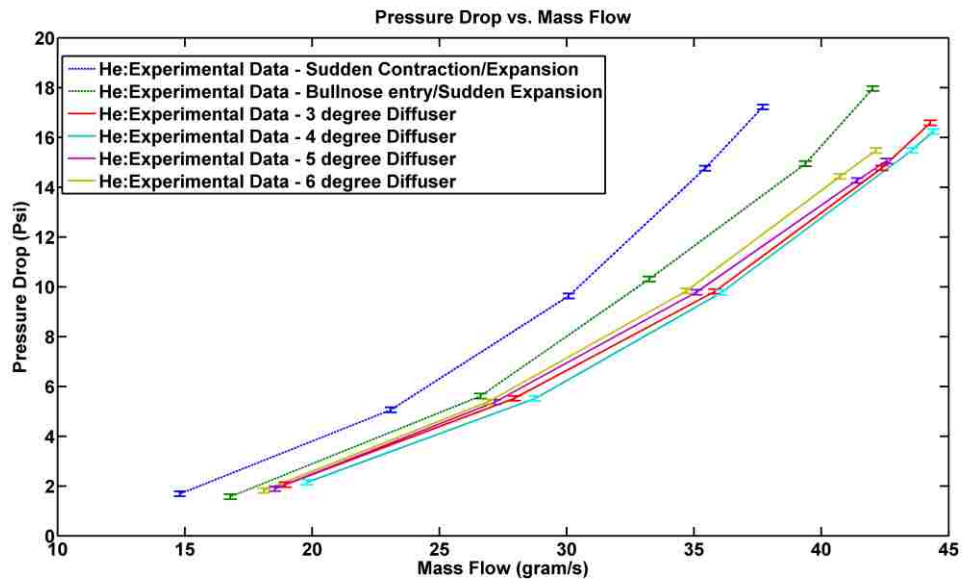

Figure 5.9: Experimental Result - Pressure Drop vs. Mass Flow

Note: All diffusers are featured with a quarter circle inlet

Table 5.1: Pressure Drop vs. Mass Flow – Geometry Comparison

Geometry/Pressure Drop	Mass Flow Rate (gram/s)			
	2 Psi	5 Psi	10 Psi	15 Psi
Sudden Contraction and Expansion	14.8	23.1	30.7	35.4
Quarter Circle Inlet	16.8	26.6	33.2	39.4
3 Degree Diffuser	18.9	27.9	35.8	42.4
4 Degree Diffuser	19.8	28.8	36.1	43.6
5 Degree Diffuser	18.5	27.2	35.1	41.4
6 Degree Diffuser	18.1	26.9	34.7	40.7

Table 5.1 shows the pressure drop vs. mass flow result for proposed geometries from the experiment. At 15 psi (system operating pressure drop), 4 degree diffuser geometry has the best performance on mass flow, which corresponds to the single channel study shown earlier. To see how much improvement each geometry has contributed, Table 5.2 was created to show the comparison.

Table 5.2: Mass Flow Percentage Improvement

Geometry/Pressure Drop	Mass Flow Improvement			
	2 Psi	5 Psi	10 Psi	15 Psi
Sudden Contraction and Expansion	--	--	--	--
Quarter Circle Inlet	13.5%	15.2%	8.14%	11.3%
3 Degree Diffuser	27.7%	20.8%	16.6%	19.8%
4 Degree Diffuser	33.8%	24.7%	17.6%	23.2%
5 Degree Diffuser	25.0%	17.7%	14.3%	16.9%
6 Degree Diffuser	22.3%	16.5%	13.0%	15.0%

Use sudden contraction inlet and sudden expansion outlet geometry as the base model; Table 5.2 shows that in every pressure drop monitored during the experiment, 4

degree diffuser geometry has always provided the highest improvement on mass flow rate. Table 5.2 has also indicated that just adding the quarter circle itself at inlet (without diffuser outlet) will improve the mass flow rate by 11.3% at the system operating pressure drop (15 psi). Use 4 degree diffuser as an example, adding a 4 degree diffuser on top of quarter circle inlet the mass flow rate increases to 23.2%. In another word, 11.9% improvement in mass flow was added to the system by simply adding 4 degree diffuser geometry.

Information shown in Table 5.2 can also be transformed into another form of relation: mass flow as a function of diffuser angle (@15 Psi pressure drop) (see Figure 5.10).
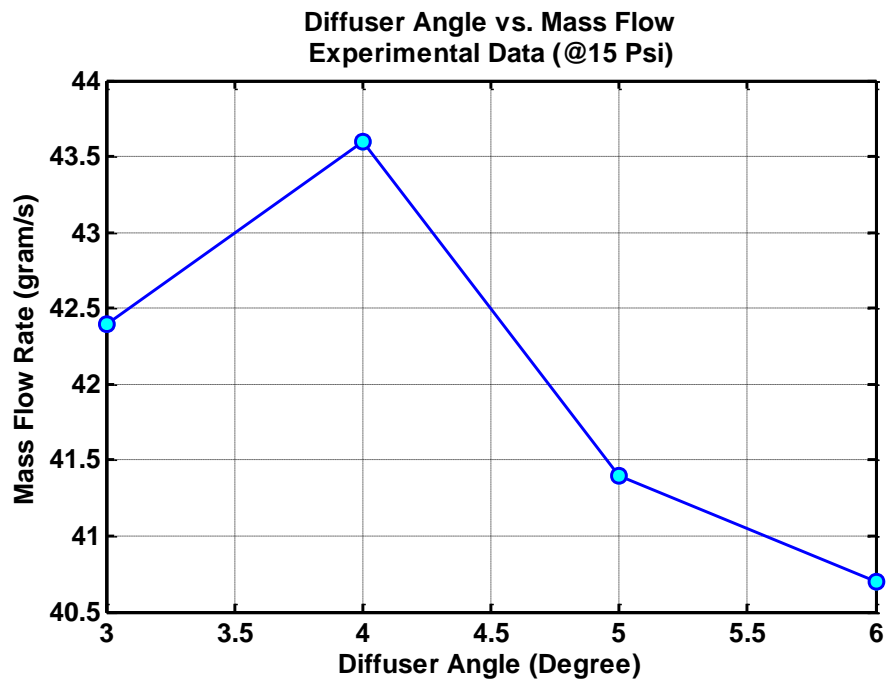

Figure 5.10: Diffuser Angle vs. Mass Flow – Experimental Data (@15 Psi)

5.4 Result and Discussion

In this section, both SKW and SSTKW models results will be evaluated and compared to the experimental data gathered in this chapter. Early study results from single channel model shown that both SKW and SSTKW models are good candidates to predict the right physics for this project. However, the best way to determine the final turbulence model is to compare them directly to the experimental data. Figure 5.11 - Figure 5.22 present the streamline contour plots for each computational analysis.

Starting from the sudden contraction and expansion case, both models have shown a great flow disturbance near the outlet region, which slows down the overall flow. For this particular geometry (sudden contraction and expansion), two models have shown different behaviors on the flow velocity distribution. For SSTKW model shown in Figure 5.11, a group of high velocity flow was concentrated near the inlet region and quickly dissipating in a short distance. On the other hand, the SKW model has shown a completely different behavior than the SSTKW model in this case. The SKW model has shown a more even flow distribution than the SSTKW model. However, the average flow rate for the SSTKW model is still higher than the SKW model. Evidence from both cases shows that by adding the quarter circle inlet and diffuser outlet, the velocity magnitude increases and the regions of flow disturbance are significantly reduced, which increases the cooling performance of the system. Evidence has also shown that as the angle of the diffuser starts to increase the flow disturbance starts to gain back its stage.
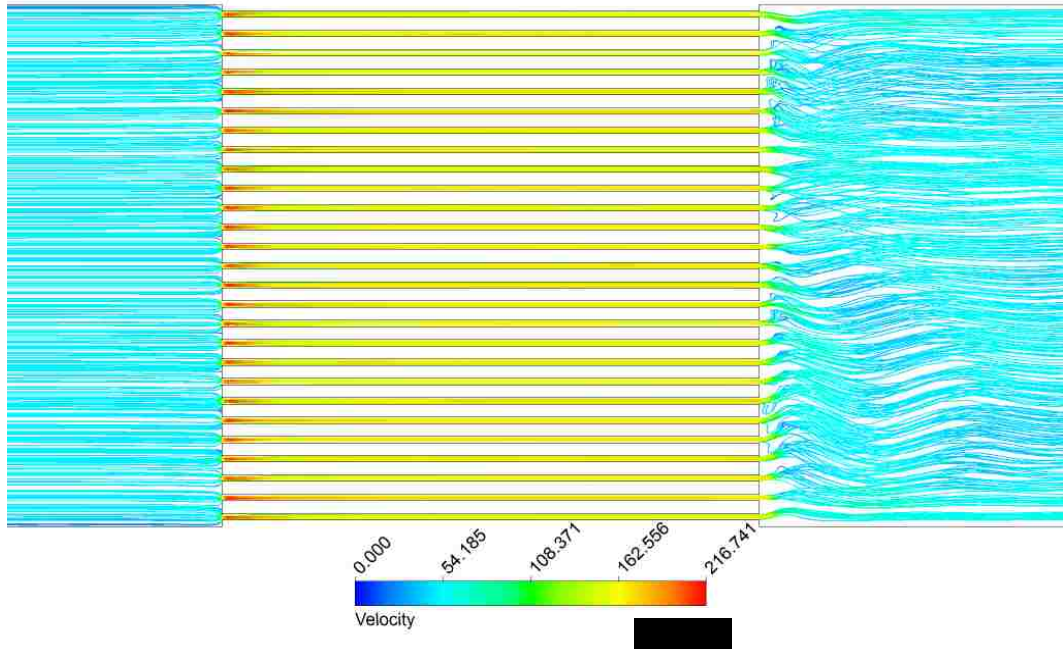
Figure 5.11: Velocity Streamline - Sudden Contraction and Expansion (SSTKW Model)
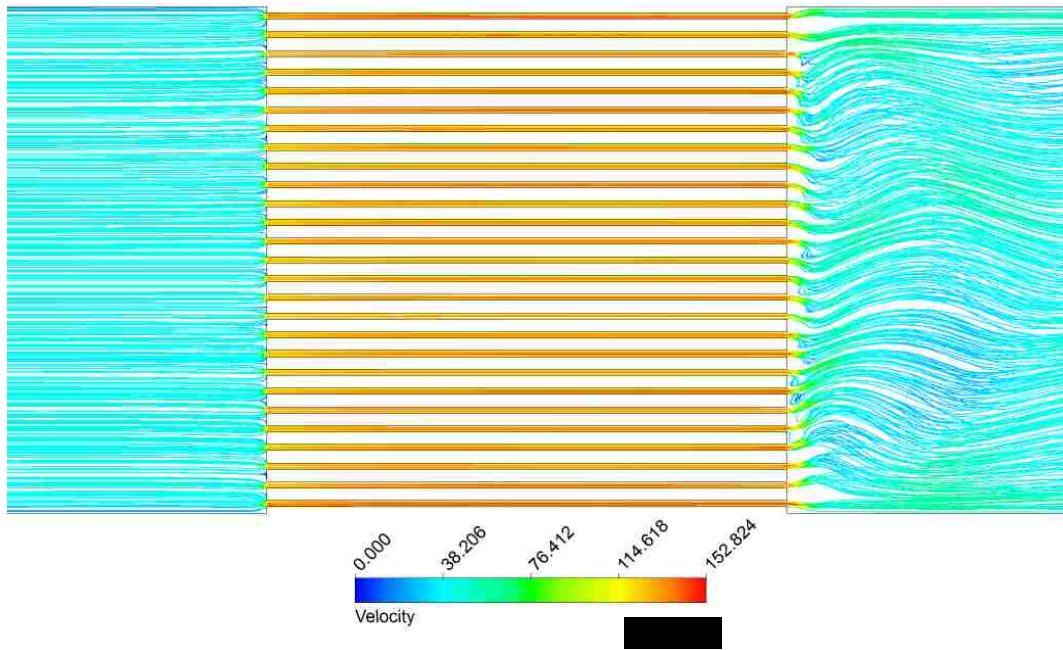
Figure 5.12: Velocity Streamline - Sudden Contraction and Expansion (SKW Model)
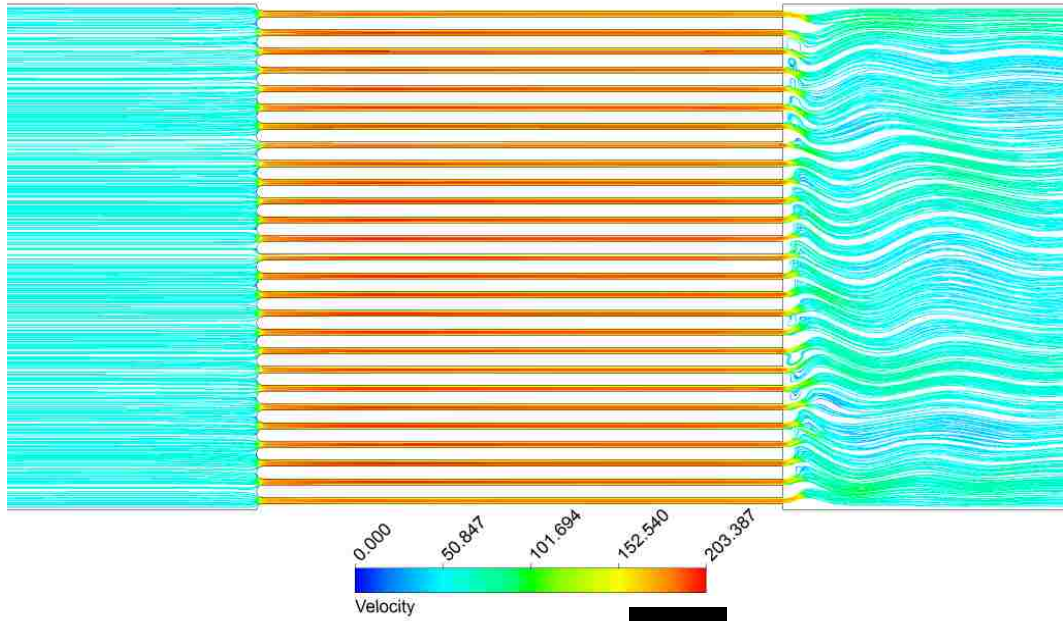
Figure 5.13: Velocity Streamline - Quarter Circle Inlet (SSTKW Model)

Figure 5.14: Velocity Streamline - Quarter Circle Inlet (SKW Model)

Figure 5.15: Velocity Streamline - 3 Degree Diffuser (SSTKW Model)

Figure 5.16: Velocity Streamline - 3 Degree Diffuser (SKW Model)

Figure 5.17: Velocity Streamline - 4 Degree Diffuser (SSTKW Model)

Figure 5.18: Velocity Streamline - 4 Degree Diffuser (SKW Model)

Figure 5.19: Velocity Streamline - 5 Degree Diffuser (SSTKW Model)

Figure 5.20: Velocity Streamline - 5 Degree Diffuser (SKW Model)

90
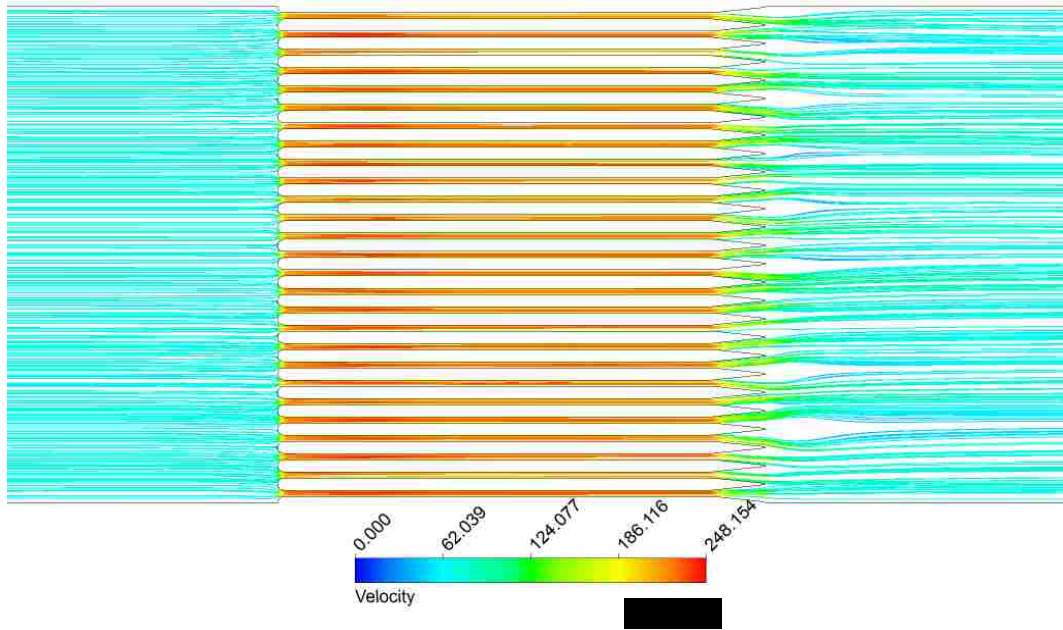
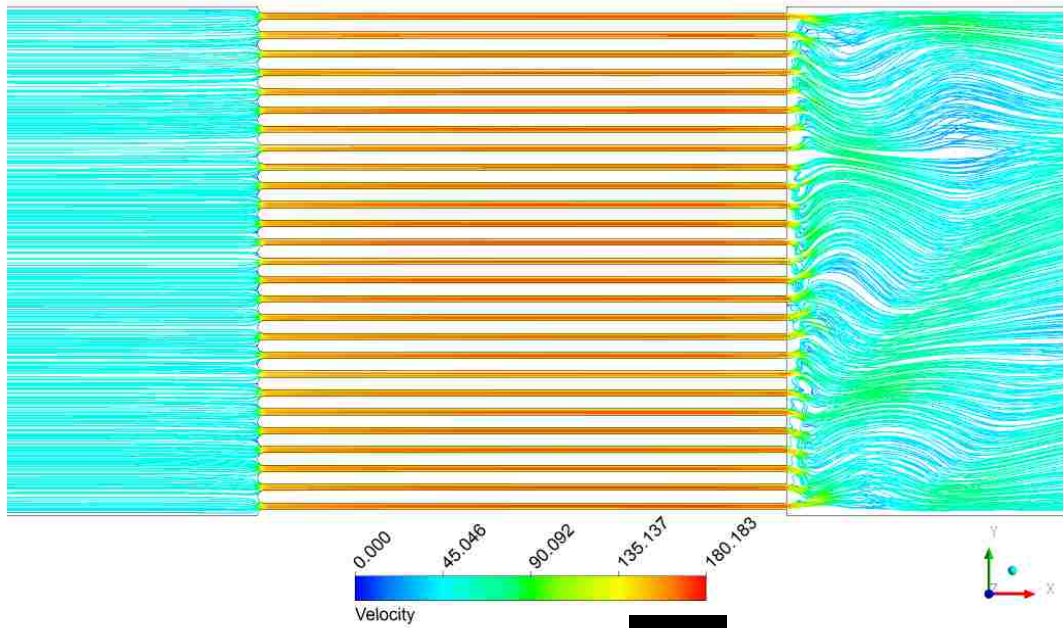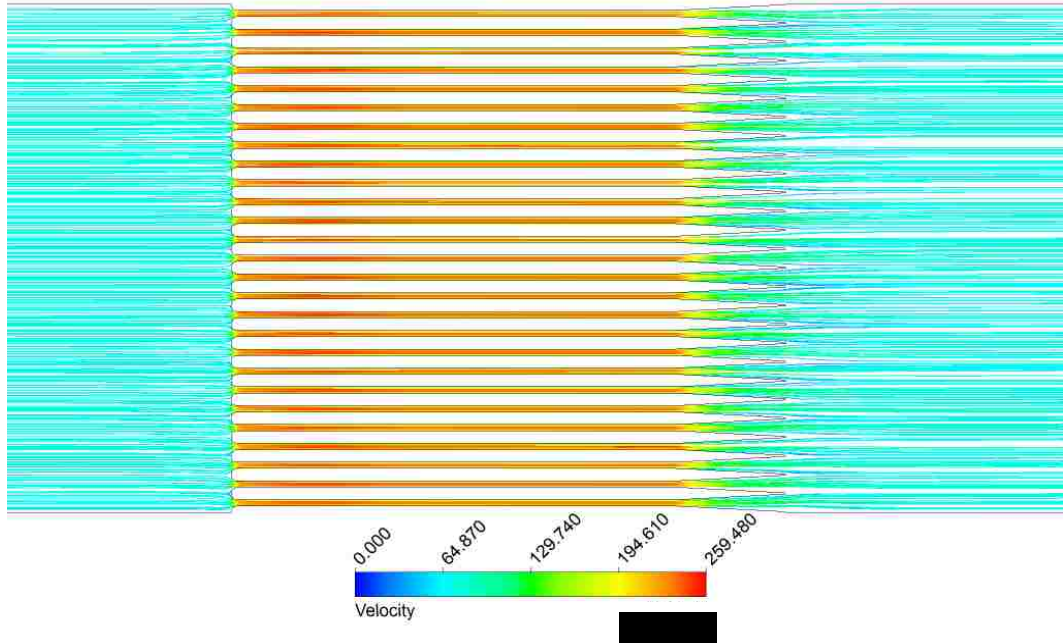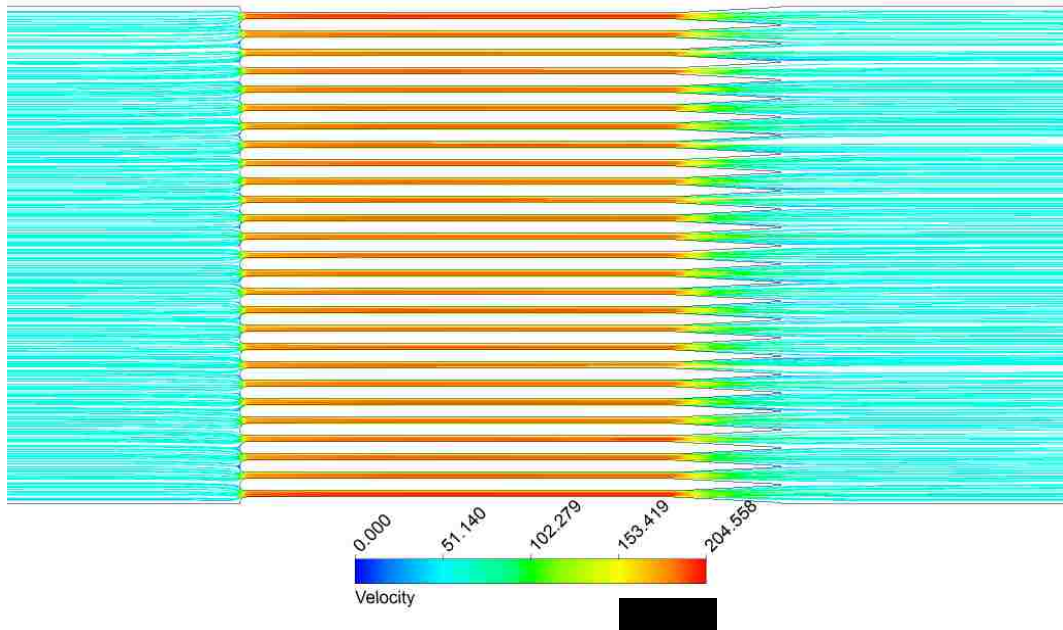Figure 5.21: Velocity Streamline - 6 Degree Diffuser (SSTKW Model)

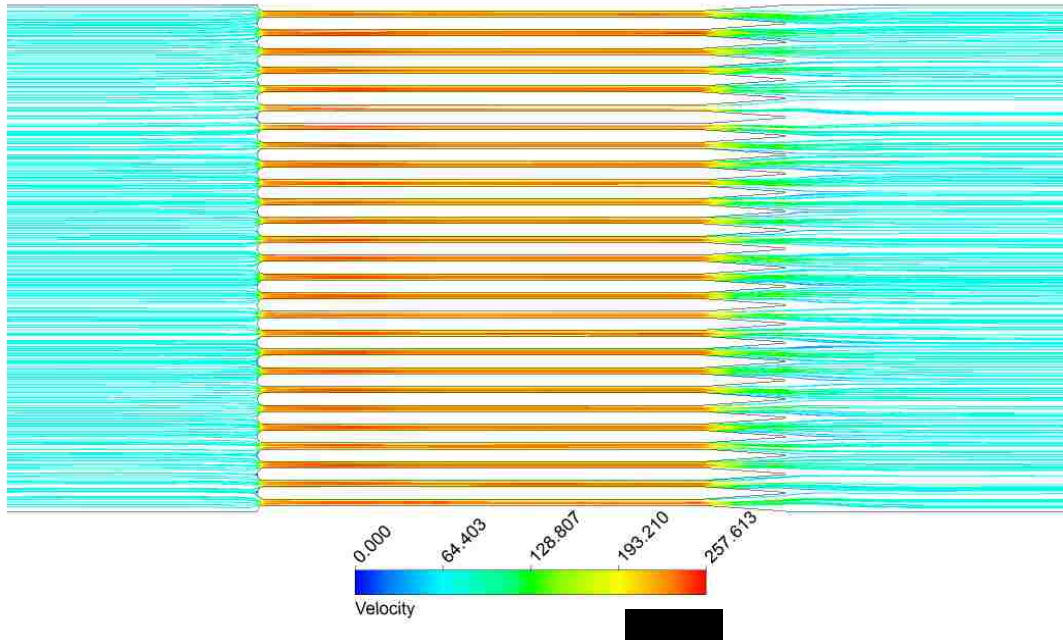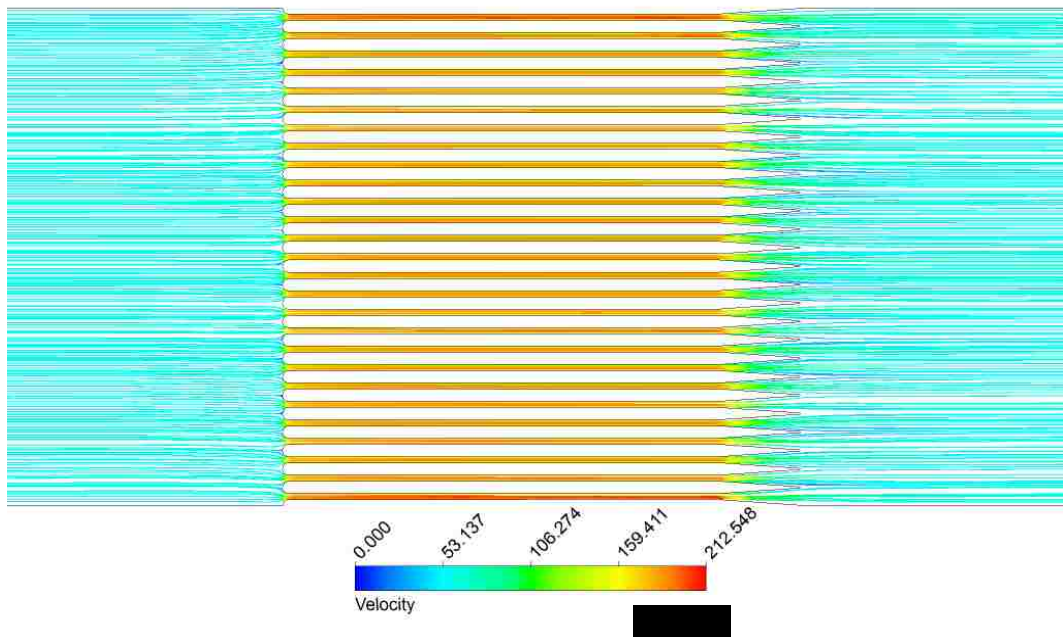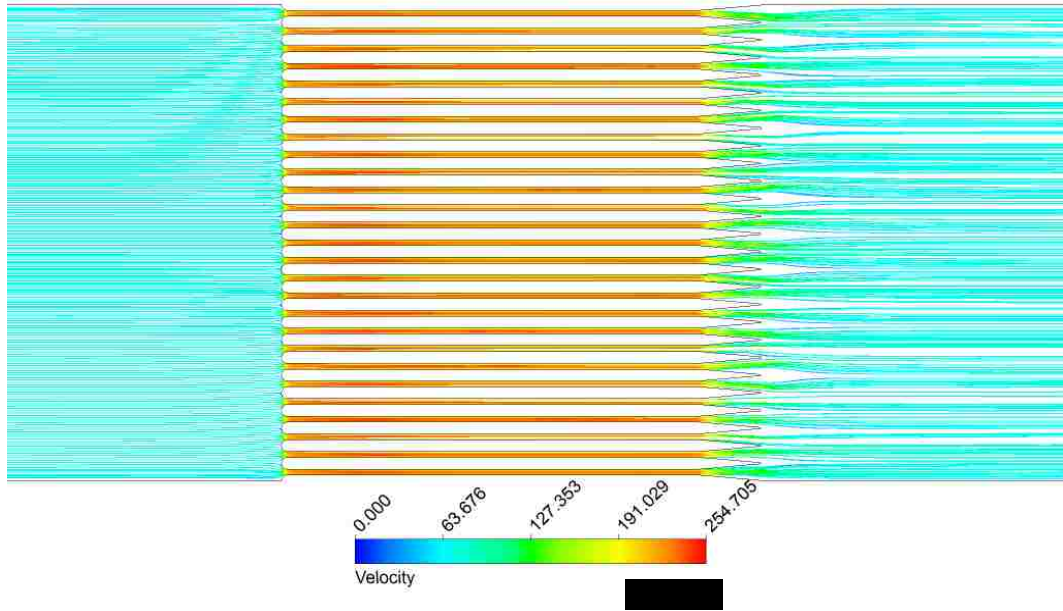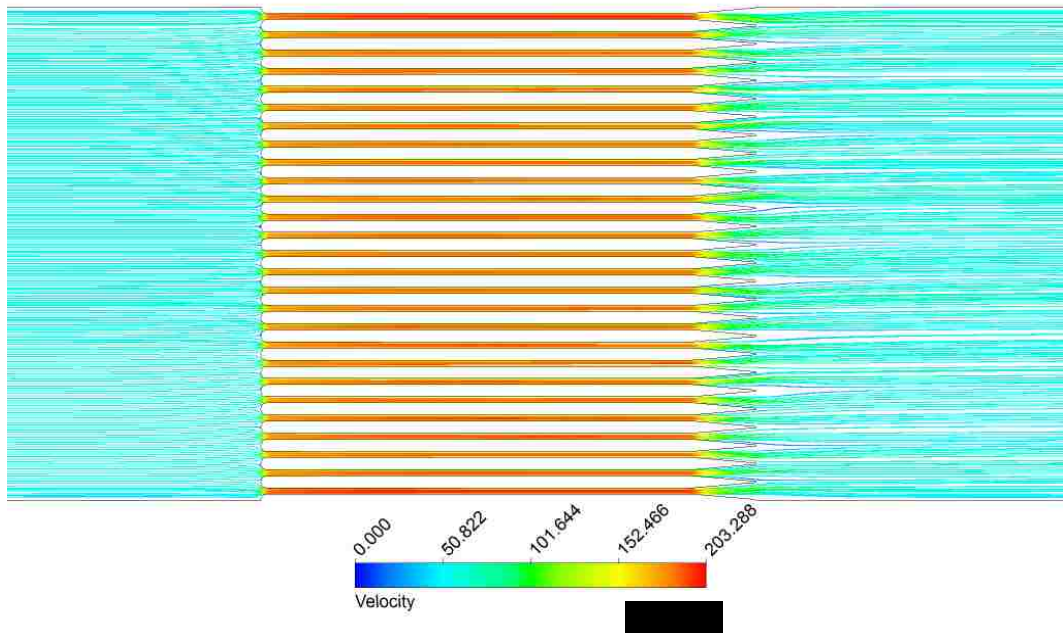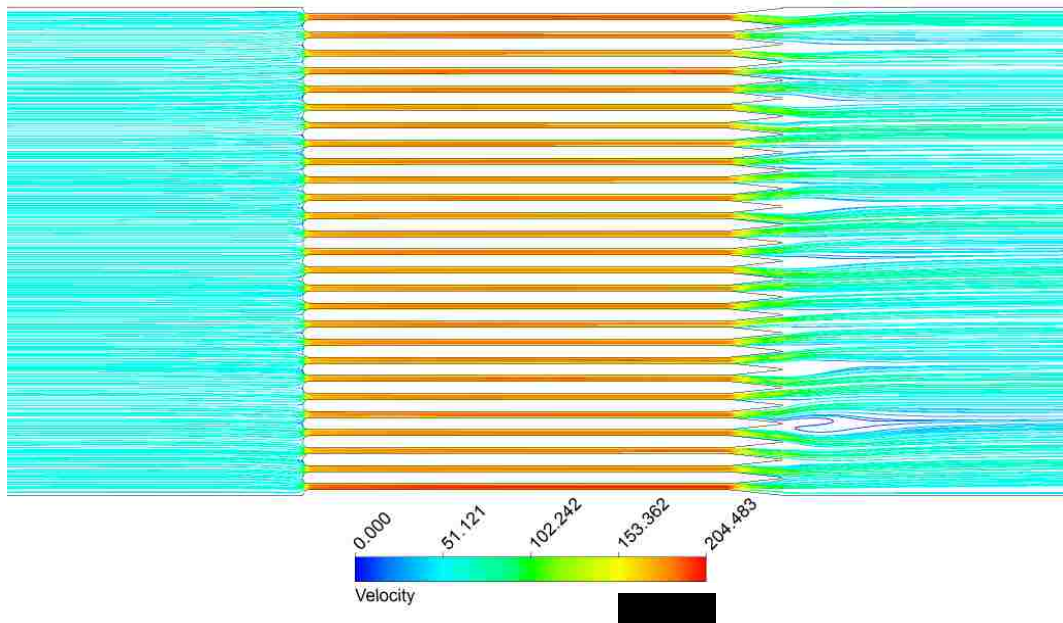Figure 5.22: Velocity Streamline - 6 Degree Diffuser (SKW Model)

Studies above have shown the models predictions on the benefit of adding quarter

circle inlet and diffuser outlet. A more ultimate way to validate the model is to compare

the model result directly to experimental data. A system matrix is created to compare all models and data side by side. A relative error was also evaluated by using the experimental data as the base case. The comparison result can be found in Table 5.3 shown below.

Table 5.3: Results Comparison - Models vs. Experimental Data (@15 Psi Pressure Drop)

Geometry/Data	Mass Flow Rate (gram/s)			SSTKW Error	SKW Error
	SSTKW Model	SKW Model	Experiment		
Sudden Contraction and Expansion	35.1	28.3	35.4	0.847%	20.1%
Quarter Circle Inlet	39.1	35.0	39.4	0.761%	11.2%
3 Degree Diffuser	49.8	41.1	42.4	17.5%	3.07%
4 Degree Diffuser	50.2	42.8	43.6	15.1%	1.83%
5 Degree Diffuser	49.2	40.9	41.4	18.8%	1.21%
6 Degree Diffuser	48.4	39.6	40.7	18.9%	2.70%

From the comparison shown in Table 5.3 some interesting results were found. For SSTKW model, it shows its strong ability of predicting the results for both sudden contraction and expansion and quarter circle inlet cases. The relative error produced from SSTKW model for these two cases were less than 1%. However, SSTKW did not perform so well on the diffuser cases. It shows a 15-19% error margin when predicting the diffuser geometries. On the other hand, SKW model behaved the opposite way than SSTKW model. For the sudden contraction and expansion and quarter circle inlet cases, SKW model leaves 11-20% error for its prediction. However, SKW model shows a strong performance on predicting the diffuser cases. Only 1-3% error was shown when using the SKW model.

The advantages and disadvantages of both turbulence models have been obtained by above mentioned analysis. The ultimate question that needs to be answered now is which model is more useful for this project. The main focus of this project is to predict the right physics for the new geometry designs. When carefully evaluating the values of both models, evidence indicates that SKW model is the better candidate than the SSTKW model for this project. SKW model shows its strong side of predicting the diffuser geometries, which will eventually be used in the production. In Figure 5.23 shows the direct comparison between the experimental data and the two models.
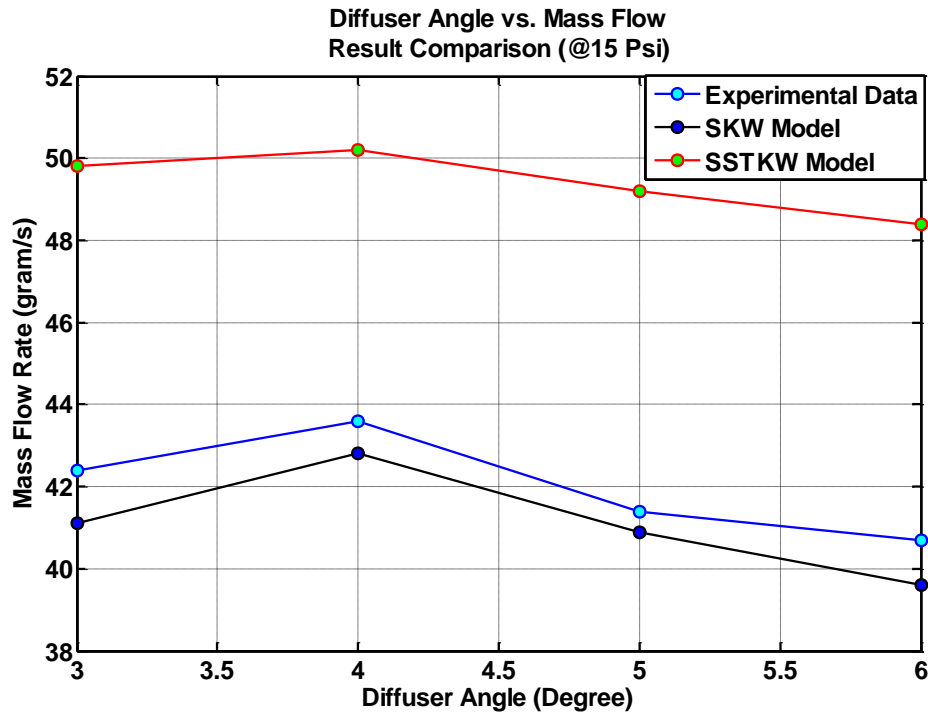
Figure 5.23: Final Result Comparison – Models vs. Experimental Data

From the result shown in Figure 5.23, clearly the SKW model has the ability of predicting the right result for the diffuser geometries at the required operating condition.

To ensure that the decision on the turbulence model is reliable a further analysis was conducted to make sure that the right turbulence model was chosen.

Early in this chapter, a plot was generated from the experimental data to show the relation between pressure drop and mass flow rate for different geometries (Figure 5.9). Since both experimental data and CFD model show that 4 degree diffuser design performs the best on mass flow rate, 4 degree diffuser design was used as a test case to help determine stability of the SKW model. In addition to the 15 Psi pressure drop operating condition, 3 more operating conditions were ran for this test and they are: 2 Psi, 5 Psi, and 10 Psi. The comparison result is shown in Figure 5.24.
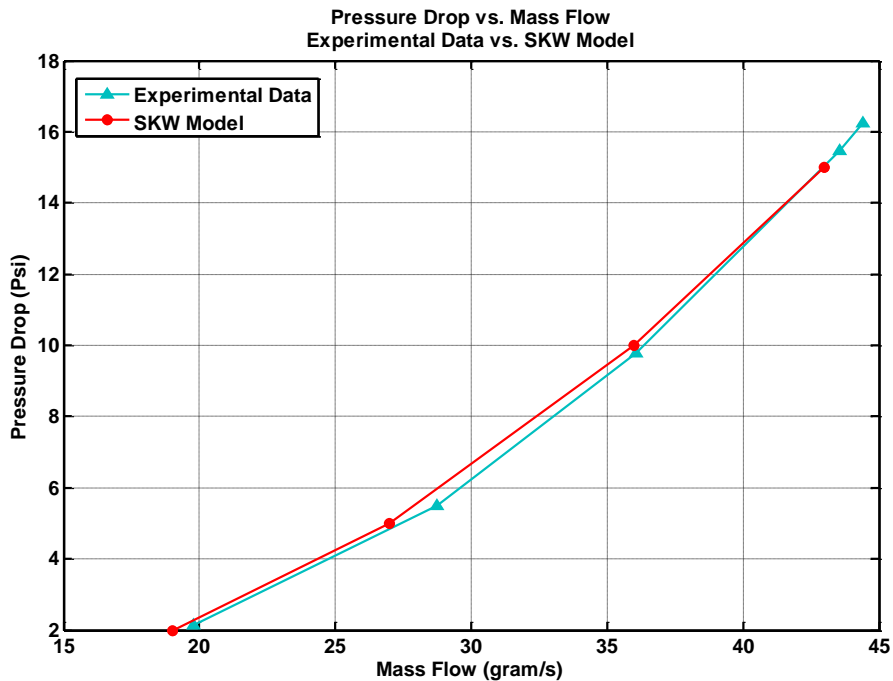
Figure 5.24: Mass Flow as a Function of Pressure Drop
Experimental Data vs. SKW Model (4 Degree Diffuser Design)

Based on the result shown in Figure 5.24, once again the SKW model has proven its strong ability of predicting the right behavior of the diffuser geometries for this project.

The performed assessment analysis shows that the SKW model is truly the right candidate for the ^{99}Mo project. Both CFD model and experimental data are showing that 4 degree diffuser design is best design compared to all other proposed designs. A maximum mass flow was achieved by using this geometry.

Chapter 6 – Conclusions and Recommendations

6.1 Conclusions

The turbulent flow through a cooling channel featuring different inlet and diffuser outlet designs has been investigated using the computational fluid dynamics software ANSYS FLUENT 14.5. The built-in standard $k - \omega$ model was validated with the experiment conducted at LANL. A very good agreement between the simulation result and the experimental data was shown in the early chapters. By using the single channel model shown in Figure 4.9 and Figure 4.10, a correlation between recirculation and diffuser angle was found for this particular project. From single channel study, there will not be any recirculation region when diffuser angle is equal to, or less than 5-degree. This correlation later proved that 5-degree diffuser angle is the critical angle, which is the turning point that affected the overall performance of the flow.

Two inlet features were proposed and compared. Quarter circle inlet was chosen over the 45° angled inlet due to its ability of reducing the head loss around the inlet section. Just by adding the quarter circle inlet itself, 12.3% of mass flow improvement was added to the system compared to the base case design (sudden contraction and expansion).

In addition to the inlet geometry, a diffuser design was added to the downstream of the target cooling channel. Evidence from both experiment and CFD model have shown that diffuser design is an efficient mechanism for decelerating the flow to prevent disturbance flow and at the same time recovering the dynamic pressure smoothly.

Not like the single channel study, multi-channels study was more complex. As mentioned earlier, the ideal case shown in single channel study could not be reproduced in the multi-channels case. There was always separation or disturbance flow in the channel. However, there was one phenomenon that occurred in both single channel and multi-channel studies. Both studies agreed that by decreasing the diffuser angle to a certain degree, separation will decrease but mass flow will increase. Proof for this phenomenon can be found from Figure 5.11 to Figure 5.22 from the multi-channels study.

Before conducting the multi-channels study, results gathered from single channel study were used to reduce the test parameters for both CFD model and experiment. Significant amounts of testing time were saved from this process.

Model validation and verification was crucial for this project. Starting from the beginning, a benchmark test was conducted by using the experimental data from Buice [19], initial result shown in Figure 3.7 indicated that both SKW and SSTKW models are the good candidates for this project. However, by comparing the results from both models to the experimental data, a final decision was made that the SKW model is the better candidate than the SSTKW model for this project. Besides comparing model result to the experimental data, mesh independency was also studied to prevent deficiency from the model. A series of mesh matrix were tested and many methods were used to ensure the stability of the model. Evidence for model stability can be found throughout Chapter 3.

Finally, a new geometry design was finalized from this study. Both experimental data and CFD model agreed that quarter circle inlet and 4 degree diffuser design is the

best combination for this project with the mission of improving heat transfer performance for the ^{99}Mo target cooling loop. 4 degree diffuser design showed less separation and higher mass flow rate than other diffuser designs.

The same methodology used in this project can be applied to many other channel flow design project that involves flow separation and diffusers. Finding the correlation between diffuser angle and recirculation flow for the design is critical. By doing the procedures described in this project, one's designing time can be significantly reduced when it comes to optimizing the performance of a channel flow.

6.2 Suggestions for Future Work

There are many areas that can be improved for this project. As mentioned in Chapter 5 section 5.2, an incident occurred during the experiment. Because of this incident all other test pieces were treated with extreme care during the experiment. For the future work, design and machine more rigid test pieces than the current ones so that a higher pressure drop can be tested.

Another big suggestion for this project is to conduct a particle image velocimetry (PIV) test. Due to the time constraint this part of test could not be completed. If this test was conducted many interesting phenomena can be discovered visually from the experiment. For instance, the wall effects, the stagnation point at the entrance, and the separation region near the diffuser. A visual comparison between CFD model and experiment can also be performed.

The final suggestion for the future work is to conduct thermal-hydraulics modeling. The reason why thermal-hydraulics model was not constructed for this project

was because there has not been an easy to conduct experiment to validate the model. Without using the real electron beam from the actual accelerator, heating the targets has become a very difficult task. Maybe in the near future there is an inexpensive method to heat up all 25 disks in the test section and have a Gaussian distribution of the heat flux applied to the test piece.

References

[1]   World Nuclear Association, 2012, "Radioisotopes in Medicine", from http://www.world-nuclear.org/info/inf55.html.

[2]   Dale, G. E., Chemerisov, S. D., Vandegrift, G. F., Woloshun, K. A., Kelsey, C. T. IV, Tkac, P., Makarashvili, V., Jonah, C. D., Olivas, E. R., Hurtle, K. P., Romero, F. P., Dalmas, D. A., Holloway, M. A., Harvey, J. T., 2012, "Design and Experimental Activities Supporting Commercial U. S. Electron Accelerator Production of Mo-99", LA-UR-12-23810, Los Alamos National Laboratory, Los Alamos, New Mexico.

[3]   D.R. McAlister and E.P. Horwitz, "Automated two column generator systems for medical radionuclides." Appl Radiat Isot., **67**, pp. 1985-91, 2009.

[4]   Division of Environmental Health, Office of Radiation Protection, July 2002, "Technetium-99m (^{99m}Tc)", Fact Sheet 320-083, Washington State Department of Health.

[5]   U.S. EPA OSWER, "EPA Facts About Technetium-99: July, 2002", (2002): n. pag. Print.

[6]   Lyra M., Charalambatou P., Roussou E., Fytros S., Baka I.,March 2011, "Alternative production methods to face global molybdenum-99 supply shortage", Hellenic Journal of Nuclear Medicine., 14(1), pp 49-55, 2011.

[7]   Petersen Vroman P. 2014, "Helium-Cooling Loop for a Molybdenum-99 Accelerator-Production System". Master Thesis, Bradley University, 2014.

[8]   Zucrow, M. J., Hoffman, J. D., *Gas Dynamics Volume 1*, John Wiley & Sons, Inc., Hoboken, NJ, Chap. 6.

[9]   Anderson, John David. *Computational Fluid Dynamics: The Basics with Applications*. New York: McGraw-Hill, 1995.

[10]   Currie, Iain G. *Fundamental Mechanics of Fluids*. Boca Raton, FL: Taylor & Francis, 2013.

[11]   Munson, Bruce Roy, T. H. Okiishi, and Wade W. Huebsch. *Fundamentals of Fluid Mechanics Sixth Edition*. Hoboken, NJ: J. Wiley & Sons, 2009. Print. Chap 1, Chap 3, Chap 7.

[12]   Obi S, Aoki K, Masuda S, "Experimental and computational study of turbulent separating flow in an asymmetric plane diffuser". In: Ninth symposium on turbulent shear flows, Kyoto, Japan; 16-19 August 1993. p. 305-1-4.

[13]   Kaltenbach, H-J 1994, *Large-eddy simulation of flow through a plane, asymmetric diffuser.* Annual Research Briefs-1994, Center for Turbulence Research, Stan- ford Univ./NASA Ames, pp. 175-184.

[14]   D. C.Wilcox. *Turbulence Modeling for CFD*. DCW In- dustries, Inc. La Canada, California. 1998.

[15]   F. R. Menter. *Review of the SST Turbulence Model Experience from an Industrial Perspective.* International Journal of Computational Fluid Dynamics. Volume 23, Issue 4.. 2009.

[16]   B. E. Launder and D. B. Spalding. "The Numerical Computation of Turbulent

Flow". Computer Methods in Applied Mechanics and Engineering. 3. 269-289. 1974.

[17]   S.M. El-Behery, M. Hamed *A comparative study of turbulence models performance for separating flow in a planar asymmetric diffuser* Computer and Fluids, 44 (2011), pp. 248-257

[18]   *ANSYS FLUENT Theory Guide 14.5.* Canonsburg, (PA): ANSYS Incorporated; 2012.

[19]   Buice, C.U. and Eaton, J.K., *Experimental Investigation of Flow through an Asymmetric Plane Diffuser*, Dept. of Mech. Eng, Stanford University, TSD-107 (1997)

[20]   H. Lan, B.F Armaly, and J.A Drallmeier. *Turbulent Forced Convection in a Plane Asymmetric Diffuser: Effect of Diffuser Angle.* Journal of Heat Transfer, Vol. 131/071702

[21]   Berdanier, Reid A. *Turbulent Flow through an Asymmetric Plane Diffuser.* Thesis. Purdue University, 2011

[22]   Oberkampf, William L., and Christopher J. Roy. *Verification and Validation in Scientific Computing*. New York: Cambridge UP, 2010.